Study on Inversion Layer at Iron Pyrite Surface for Photovoltaic Application
(太陽光発電応用に向けた黄鉄鉱表面の反転層に関する研究)

March 2019

Shunsuke UCHIYAMA

Graduate School of Materials Science

Nara Institute of Science and Technology

Abstract

Photovoltaic devices are clean energy technologies that can generate electric power with suppressing the consumption of limited resources for increasing electric demand. Greatly increased demand of photovoltaic devices requires next generation photovoltaic material that fulfills various application and mass production. Iron pyrite (cubic FeS_2) is a candidate for thin film photovoltaic device material because of its high light absorption coefficient ($\alpha > 10^5$ cm^{-1} for $h\nu > 1.3$ eV), earth-abundance and low cost material. However, previous reports show poor performance of iron pyrite photovoltaic devices, and it is essential to understand the reason for the poor performance. In this thesis, an inversion layer at iron pyrite surface is focused as cause which can reduce the conversion efficiency. To reveal an effect of the inversion layer, device simulation of iron pyrite thin film photovoltaic device and characteristics evaluation of iron pyrite single crystal are performed.

In Chapter 2, a two-dimensional (2D) device simulator, ATLAS, was utilized to investigate the device structure toward high performance iron pyrite thin film photovoltaic device. In addition, an effect of the inversion layer at the surface region of iron pyrite was investigated to carry out the numerical simulation and design of an iron pyrite photovoltaic device by combining the density of states in surface layer and bulk layers of iron pyrite. It was founded that the following factors allow iron pyrite thin film photovoltaic device efficiency as high as around 13.5% to be achieved: a *p*-Cu_2O/*n*-FeS_2 hetero-junction, a density of states in the bulk layer of less than 1×10^{15} cm^{-3}, and carrier lifetime in the bulk of longer than 1 μs. To realize higher efficiency iron pyrite thin film photovoltaic device, it is necessary to remove the surface layer and reduce the density of states of the deep donor level during the fabrication of the bulk layer.

In Chapter 3, the chemical-bonding state and phase purity at the surface region of iron pyrite single crystal wafers treated by alcohol washing and aqua regia etching were evaluated

by micro-Raman spectroscopy and XPS. From these measurements, it was found that phase purity at iron pyrite surface was improved and oxidation productions were removed by aqua regia treatment. However, oxide absorption at iron pyrite surface was confirmed because the oxide and water in air immediately reacts with the surface of iron pyrite and Fe^{3+}–OH^- species were created. Therefore, it was difficult to completely remove the oxidation productions at iron pyrite surface.

In Chapter 4, band structure and electrical transport characteristics of iron pyrite single crystal were evaluated to investigate the effect of oxidation production at iron pyrite surface for band bending. From these results of PYS, KFM and optical measurements, it was suggested that an inversion layer at the surface region of iron pyrite single crystal might be formed although oxidation productions were removed. This result indicated that the formation of the inversion layer at iron pyrite surface might contribute to defect levels based on LFT model rather than oxidation layer. In addition, the formation of localized states below conduction band of iron pyrite was estimated from optical characteristic evaluations such as ellipsometry and Micro-PL. The formation of localized states was supposed by also Hall effect measurement because Mott-VRH conduction at low temperature was observed. Therefore, it was revealed that not only the inversion layer but also the intrinsic defect levels in the bulk contributed to poor performance of photovoltaic device. To improve photovoltaic characteristics, it is necessary to reduce the intrinsic defect levels in the bulk because the intrinsic defect levels lead to the formation of localized states below conduction band which reduces band gap and encourage the carrier recombination through the defects.

In Chapter 5, the conclusions of this study and future plan are summarized. In addition, problems relating to the proposed method are highlighted, and suggestions for future work to solve these problems are provided.

Acknowledgements

First of all, I would like to express my deepest gratitude to Professor Yukiharu Uraoka for his supervision, continuous guidance, and kind encouragement through fruitful discussions.

I would like to thank Professor Masakazu Nakamura and Associate Professor Hiroyuki Katsuki for their supervision and critical comments for improving this thesis.

I would like to express my hearty appreciation and gratitude to Associate Professor Yasuaki Ishikawa for his continuous guidance concerning experimental details, helpful suggestions, and constructive discussions throughout this work. I am also indebted to Assistant Professor Mutsunori Uenuma, Assistant Professor Mami Fujii, and Assistant Professor Juan Paolo Soria Bermundo for his fruitful suggestions and their support in my daily work. I am also indebted to Ms. Yukiko Morita for her great support and kindness in my daily work.

I also thanks for Mr. Noritaka Koike, Mr. Kazuhiro Miyake, Mr. Fumio Asanoma, Mr. Shohei Katao, Mr. Masahiro Fujihara, and Mr. Yasuo Okajima for technical help.

I wish to express gratitude to Associate Professor Yoshitaro Nose, Dr. Shigeru Nakatsuka, Dr. Ryoji Katsube, Mr. Taro Kuwano, and all members of the Nanostructual Design of Advanced Materials Laboratory in Kyoto University for their support, technical advice and fulfilling discussions on my experiments conducted at Kyoto University.

I wish to express gratitude to Associate Professor Takeaki Sakurai, Assistant Professor MD. Monirul Islam, and all members of the Sakurai and Islam Laboratory in Tsukuba University for their support, technical advice and fulfilling discussions on my experiments conducted at Tsukuba University.

I wish to express gratitude to Professor Takashi Minemoto, Professor Jakapan Chantanna, Mr. Yuya Ishino, and all members of the Takakura and Minemoto Laboratory in Ritsumeikan University for their support, technical advice and fulfilling discussions on my experiments conducted at Ritsumeikan University.

I wish to express gratitude to Professor Hideaki Adachi from Mesoscopic Material Science Laboratory in NAIST and all members of Panasonic Corporation for their support, technical advice and fulfilling discussions on my experiments conducted at Panasonic Corporation.

I wish to acknowledge Dr. Takahiro Doe, Dr. Seiya Yoshinaga, Mr. Itaru Raifuku, Mr. Yusuke Kawamura, Mr. Kazuki Noguchi, Mr. Takuya Oshima, Mr. Yuuya Nakai, Mr. Nguyen Chung Dong, Mr. Hiroto Murakawa, Mr. Daisuke Kobayashi, Ms. Sachiko Morioka, Mr. Ryosuke Sato, Mr. Go Sasakawa for sharing meaningful time to discuss fabrication process and characterization in photovoltaic devices and materials.

I wish to acknowledge Dr. Satoshi Urakawa, Dr. Hiroki Kamitake, Dr. Takahiro Ban, Dr. Haruka Yamazaki, Dr. Koji Yoshitsugu, Dr. Yana Mulyana, Dr. Shinji Araki, Dr. Chao He, Dr. Keisuke Kado, Dr. Kyohei Nabesaka, Dr. Daisuke Hishitani, Dr. Kulchaisit Chaiyanan, Dr. Kahori Kise for their helpful advice and valuable discussions.

I am grateful to Mr. Yuta Fujimoto, Mr. Shun Okazaki, Mr. Yoshiaki Nieda, Mr. Yang Liu, Ms. Hiromi Okada, Mr. Yuma Karaki, Mr. Yuki Hashima, Mr. Michael Paul Jallorina, Mr. Lin Tengda, Mr. Yuki Tada, Mr. Xudongfang Wang, Ms. Jenichi Clairvaux Felizco, Mr. Masaaki Furukawa, Mr. Muhammad Arif, Ms. Dianne Corshino, Mr. Ryota Ando, Mr. Tsubasa Nakamura, Mr. Yuta Miyagoshi, Mr. Ryosuke Mochii, Mr. Kenta Umeda, Mr. Yoshitaka Watanabe, Ms. Aimi Syairah Binti Safaruddin, Mr. Takanori Takahashi, Mr. Naoyoshi Noda, Mr. Masato Higashi, Mr. Hoshito Murakawa, Mr. Daichi Yoshii, Mr. Kohei Fujimoto, and all members in the various laboratories for their understanding and for sharing good times during this research work.

Finally, I would really like to thank my parents, sisters, and all my friends for their understanding, continuing care, support and encouragement.

March, 2019

Shunsuke Uchiyama

Contents

Chapter 1

Introduction

1.1 Background

Production of modern electric energy is highly dependent on thermal power generation using fossil fuel and nuclear power generation using radioactive elements. Since these consume resources to produce electric energy, exhaustion of limited resources is a concern with an increase in demand and population. Furthermore, it becomes a factor in the further increase of CO_2 emission, which is a cause of global warming problem in recent years. In contrast, sunlight, solar heat, hydraulic power, wave power and wind power generation are clean energy technologies that convert natural energy into electric energy, and are indispensable technologies for building a sustainable society. In particular, photovoltaic generation is a technology that utilizes the enormous amount of solar energy, and as it can simply obtain power from anywhere on the earth without developing large scale infrastructure, it is anticipated as a technology to suppress the consumption of limited resources. However, photovoltaic generation depends on solar radiation, which is difficult to supply stably. As the grid interconnection system backed up by the electric power system was established, the range of solar power generation to be used is widely expanded, and various measures were introduced by government such as fixed price purchase and tax deduction as a technology to cope with global warming. The current cumulative introduction amount of the world is going to be 400 GW. Due to the increase in the introduction amount of photovoltaic power generation, the problem of securing consistency between power generation and electric power demand and installation site problems has developed to a situation where constraints are introduced in the future introduction. For this, it is important to stabilize power supply by introducing power storage function etc. In addition to

its role as a simple power supply technology from the past, it is strongly required to contribute to social structural change that makes full use of the characteristics of solar power generation toward the construction of a sustainable society. Production volume of solar cell modules in the world. Figure 1.1 shows that production volume reaches 75 GW in 2016 and 100 GW in 2017 [1]. Crystalline silicon solar cells occupy 90% or more of these. In the production of solar cell modules Japan, the United States and Europe, have led the technology development until the first half of the 2000s, when the main production base moved to the East Asian region such as China and Taiwan. Production volume in China in 2016 is about 53 GW, or about 70% of the world market share.

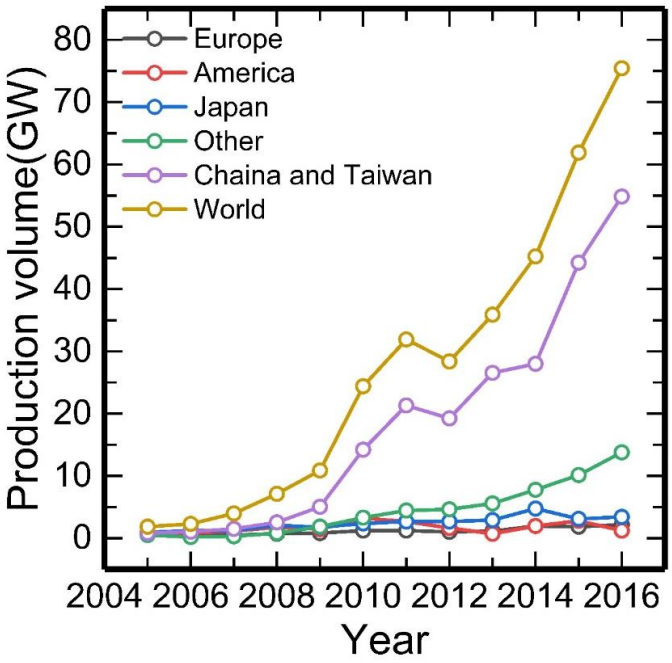

Fig. 1.1 Production volume of solar cells [1].

1.2 Solar Cells

1.2.1 Category of solar cells

When semiconductor p-n junction is irradiated with light having energy larger than the forbidden band width of the semiconductor, electron-hole pairs are generated in the semiconductor. The generated electron-hole pair is separated by the internal electric field present at the junction, and holes are collected on the *p*-side and electrons are collected at the *n*-side, and an electromotive force is generated outside. A device that converts sunlight into electric energy with such a principle is called a solar cell. Table I.I shows the classification of solar cells [2]. Currently, semiconductor materials used for commercialized solar cells are roughly classified into silicon type and compound semiconductor type.

For silicon type, there are crystalline silicon types using a bulk crystal, thin film silicon types using a thin film, and a hetero junction type of a bulk crystal and a thin film. Crystalline silicon is the most widely used semiconductor material for solar cells. Among crystalline silicon, single crystal systems of non-concentration type records 26.1% and this record is close to the theoretical limit value. However, it is costly and disadvantageous. On the other hand, the polycrystalline system has an efficiency of 22.3%, which is slightly lower than that of the single crystal system. However polycrystalline silicon is made by silicon chloride, which has the advantage that the manufacturing process enable to fabricate productions with saving resources and cost. Silicon thin film utilizing amorphous silicon enables to fabricate productions in a low

temperature process and save resources and cost due to thin film. However reported highest efficiency of amorphous silicon thin film solar cell remains 14.0% and cell performance degrades due to photodegradation. Recently, the heterojunction with intrinsic thin-layer (HIT) solar cell is developed and records 26.6%. This cell is fabricated by combining amorphous silicon and crystalline silicon.

Compound semiconductor type includes compound thin film systems such as multi-junction type using III-V compounds, CdTe type and $CuInGa(Se,S)_2$ (CIGS) type. III-V solar cells are fabricated by depositing various III-V compound semiconductors to form multilayer structure on GaAs single crystal substrate. It is an ultra-high performance solar cell that demonstrates high conversion efficiency such as 46.0% of 4 junction type concentrating solar cells. Concentration is the order of 500-1000. However III-V solar cells are expensive and utilized for space solar cells and concentrator solar cells. On the other hand, other compound thin film solar cells such as CdTe type and CIGS type record conversion efficiency exceeding 20%. Especially, these thin film solar cells is fabricated in large area size and enable to save resources and cost because light absorption layer is only a few micron thickness. However the module efficiency remains about 14%.

In addition, dye sensitized solar cells and organic thin film solar cells are at the research phase. Especially, perovskite solar cells are rapidly developing and have already exceeded 20% of conversion efficiency.

Table I.I Category of solar cells [2]

Category	Type	Cell Eff. (%)	Characteristics
Crystalline Si cell	Single crystal	26.1	High performance
	Multi crystal	22.3	Low cost than single crystal
	Hetero-junction	26.6	High performance, High cost
Thin film	CIGS	22.9	High performance, Flexible, Low cost, Including rare metal
	CdTe	22.1	High performance, Flexible, Low cost, Including Cd
	a-Si:H	14.0	Low cell performance, Low cost, Light degradation
Multi-junction cell	III-V	46.0	Highest performance, High cost, Application for space technology Concentration : Order of 500-1000
Emerging PV	Dye-sensitize	11.9	Research phase, Indoor applications
	Organic	12.6	Research phase, Flexible, Low cost
	Perovskite	23.3	Research phase, High performance, Flexible, Low cost, Including Pb

1.2.2 Ideal band gap for material of photovoltaic device

The band gap (E_g) of the semiconductor is greatly related to the conversion efficiency of the solar cell. Figure 1.2 shows an equivalent circuit diagram of the solar cell. From Fig. 1.2, the solar cell can be regarded as a current source having a short-circuit current I_{SC} in which diodes are connected in parallel. The total current-voltage (I-V) characteristics of such a device under illumination is simply calculated by the dark current and the photocurrent, given as from Eq. (1.1):

$$\boldsymbol{I_{SC} = I_0\left(e^{\frac{qV}{kT}} - 1\right) - I_L} \qquad (\mathbf{1.1})$$

The open-circuit voltage (V_{OC}) is obtained by setting $I_L = 0$:

$$\boldsymbol{V_{OC} = \frac{kT}{q}\ln\left(\frac{I_{SC}}{I_0} + 1\right) \cong \frac{kT}{q}\ln\left(\frac{I_{SC}}{I_0}\right)} \qquad (\mathbf{1.2})$$

Hence for a given I_L, the V_{OC} increases logarithmically with decreasing saturation current I_0. For a regular p-n junction, the ideal saturation current is given by Eq. (1.3):

$$\boldsymbol{I_0 = AqN_CN_V\left(\frac{1}{N_A}\sqrt{\frac{D_n}{\tau_n}} + \frac{1}{N_D}\sqrt{\frac{D_p}{\tau_p}}\right)exp\left(\frac{-E_g}{kT}\right)} \qquad (\mathbf{1.3})$$

As seen, I_0 decreases exponentially with E_g. Therefore a large E_g is required to obtain a large V_{OC}. The maximum V_{OC} corresponds to the built-in potential of the junction, and the maximum built-in potential is close to the energy gap. Equation (1.1) is plotted in Fig. 1.3. The curve of I-V characteristic passes through the fourth quadrant after solar cell is illuminated by sunlight, which shifts from black line to red line in Fig. 1.3. By properly choosing a load, close to 80% of the product can be extracted. Here, the short-circuit current I_{SC} is equal to the photocurrent. The colored area in Fig. 1.3 corresponds to the maximum power output, and each volume of current, voltage and power is I_m, V_m and P_m, respectively. To derive the maximum-power operation point, the output power is given by Eq. (1.4):

$$\mathbf{P} = \boldsymbol{V I_L} = \boldsymbol{V}\left\{\boldsymbol{I_{SC}} - \boldsymbol{I_0}\left(\boldsymbol{e^{\frac{qV}{kT}}} - \mathbf{1}\right)\right\} \tag{1.4}$$

The condition for maximum power can be obtained when *dP/dV = 0* by Eq. (1.5). In addition, V_m and I_m are written by Eq. (1.6) and Eq. (1.7). Moreover, the maximum power output V_m is then by Eq. (1.8).

$$\frac{\boldsymbol{dP}}{\boldsymbol{dV}} = \boldsymbol{I_{SC}} + \boldsymbol{I_0} - \boldsymbol{I_0}\left(\frac{\boldsymbol{qV}}{\boldsymbol{kT}} + \mathbf{1}\right)\boldsymbol{e^{\frac{qV}{kT}}} = \mathbf{0} \tag{1.5}$$

$$\boldsymbol{V_m} = \frac{\boldsymbol{kT}}{\boldsymbol{q}}\mathbf{ln}\left[\frac{\mathbf{1} + \left(\frac{\boldsymbol{I_{SC}}}{\boldsymbol{I_0}}\right)}{\mathbf{1} + \left(\frac{\boldsymbol{qV_m}}{\boldsymbol{kT}}\right)}\right] \cong \boldsymbol{V_{OC}} - \frac{\boldsymbol{kT}}{\boldsymbol{q}}\mathbf{ln}\left(\mathbf{1} + \frac{\boldsymbol{qV_m}}{\boldsymbol{kT}}\right) \tag{1.6}$$

$$\boldsymbol{I_m} = \boldsymbol{I_0}\left(\frac{\boldsymbol{qV_m}}{\boldsymbol{kT}}\right)\boldsymbol{e^{\frac{qV_m}{kT}}} \equiv \boldsymbol{I_{SC}}\left(\mathbf{1} - \frac{\mathbf{1}}{\frac{\boldsymbol{qV_m}}{\boldsymbol{kT}}}\right) \tag{1.7}$$

$$\boldsymbol{P_m} = \boldsymbol{I_m V_m} \cong \boldsymbol{I_{SC}}\left[\boldsymbol{V_{OC}} - \frac{\boldsymbol{kT}}{\boldsymbol{q}}\boldsymbol{ln}\left(\mathbf{1} + \frac{\boldsymbol{qV_m}}{\boldsymbol{kT}}\right) - \frac{\boldsymbol{kT}}{\boldsymbol{q}}\right] \tag{1.8}$$

Here, the ideal conversion efficiency is the ratio of the maximum power output to the incident power P_{in}.

$$\boldsymbol{\eta} = \frac{\boldsymbol{P_m}}{\boldsymbol{P_{in}}} \tag{1.9}$$

On the other hand, I_{SC} is written by Eq. (1.10). Q is carrier collection efficiency, α is optical absorptions, l is thickness, and $n_{ph}(E_g)$ is photon number. When E_g increases, I_{SC} decreases because light on long wavelength is not absorbed.

$$\boldsymbol{I_{SC}} = \boldsymbol{Q}[\mathbf{1} - \mathbf{exp}(-\boldsymbol{\alpha l})]\boldsymbol{q}\boldsymbol{n_{ph}}(\boldsymbol{E_g}) \tag{1.10}$$

As seen in Eq. (1.2) and (1.3), the V_{OC} decreases as the E_g decreases. On the other hand, the I_{SC} increases as the E_g increases as written by Eq. (1.10). Therefore, the theoretical limit conversion efficiency which is also known as a Shockley-Queisser limit depends on the E_g as shown in Fig. 1.4 [3]. From Fig. 1.4, the theoretical limit conversion efficiency is the maximum at 1.4 eV. Therefore, Fig. 1.4 shows that the conversion efficiency of the silicon solar cell is close to the

theoretical limit. On the other hand, CIGS solar cell and CdTe solar cell can still improve the photovoltaic performance.

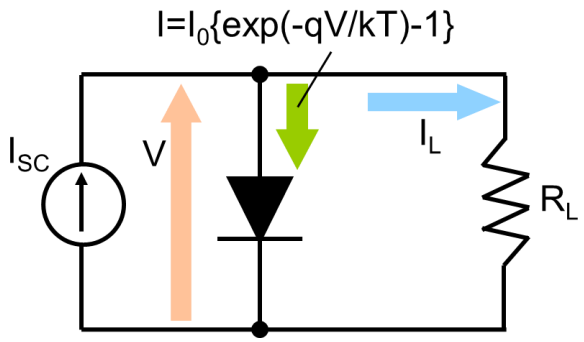

Fig. 1.2 Idealized equivalent circuit of solar cell under illumination.

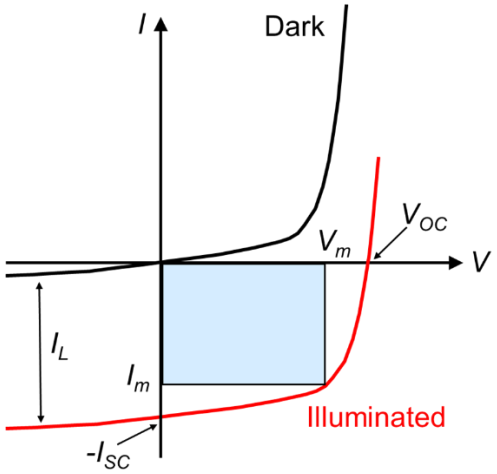

Fig. 1.3 *I-V* characteristics of solar cell under illumination. Determination of maximum power output is indicated.

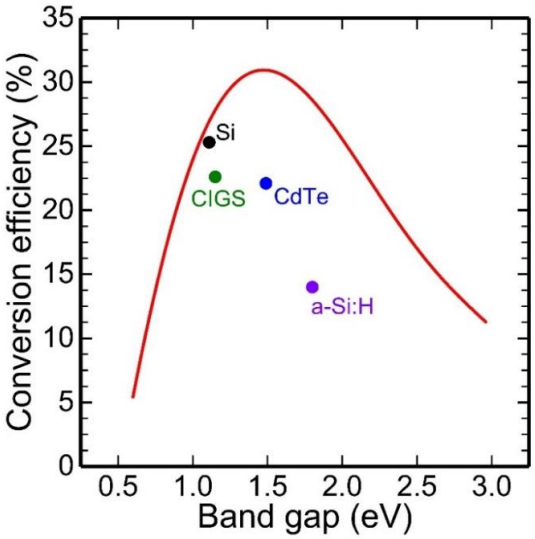

Fig. 1.4 Theoretical limit conversion efficiency vs band gap (E_g). Each dot of Si, CIGS, CdTe and a-Si:H corresponds to the highest conversion efficiency from Table I.I [3].

1.2.3 Optical absorption of semiconductor material

The absorption coefficient in some materials is shown in Fig. 1.5 [4]. Vertical axis plots the light absorption coefficient α (cm^{-1}) and horizontal axis plots the photon energy E (eV). The relation of $E = 1239.8/\lambda$ holds between the photon energy E and the wavelength λ (nm). Comparing some materials, compound materials such as CuIn(Se,S) (CIS), CdTe and GaAs show strong light absorption. Since the penetration depth into light is the reciprocal of the light absorption coefficient α, the penetration depth of the light for CIS, CdTe and GaAs is short even on the longer wavelength side, which enables to utilize the device as thin film solar cell. Thin film solar cell can save cost because a small of amount of material can fabricate the device. In addition, thin film solar cell enables to fabricate flexible cell, which leads to develop various application. However, CIGS and CdTe are not suitable to realize mass production because these materials contain toxic elements such as Cd and rare metals such as In and Ga. Ideally, the material consisted of non-toxic elements and rare metal free is essential to realize mass production of thin film solar cell.

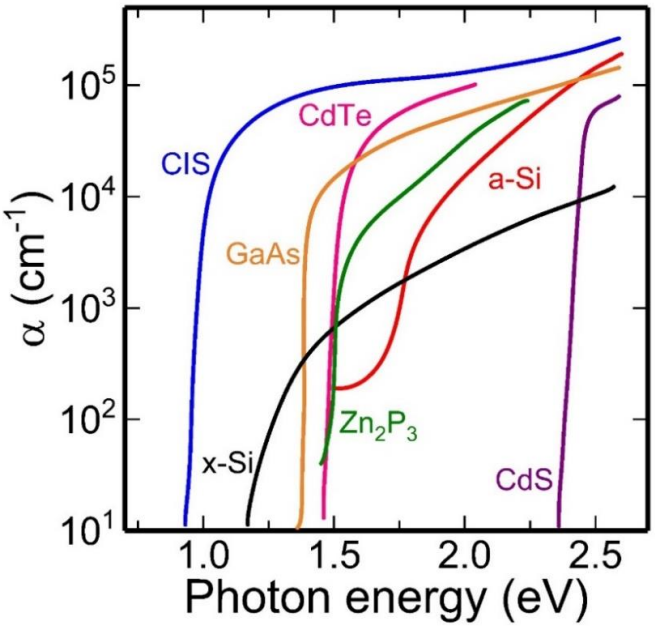

Fig. 1.5 Optical absorption coefficient α of some materials [4].

1.3 Rare Metal Free and Non-toxic Materials

Various materials are studied as an alternative material for CIGS and CdTe. Table I.II shows the best record of photovoltaic characteristics using rare-metal free and non-toxic materials [5-10]. $Cu_2ZnSnS_xSe_{4-x}$ (CZTS) is the material with the highest conversion efficiency among the materials composed of rare metal-free and nontoxic elements. It has recorded 12.6% as the highest efficiency so far [7]. CZTS is a quaternary compound semiconductor of I_2-II-IV-VI_4, in which In and Ga of group III of chalcopyrite Cu(In, Ga)(S, $Se)_2$ are divided by Zn of group II and Sn of group IV. It is a substituted material. CZTS is also being developed as a submodule, which reached 11.38% [11]. In contrast, as a material other than CZTS, various materials such as Cu_2SnS, SnS, Cu_2O, $CuSbS_2$, $ZnSnP_2$ and the like are studied as a next generation compound thin film material which is a rare-metal free and nontoxic element, but the conversion efficiency is 3-5%. Currently, materials exceeding CZTS are not found, and exploration of new materials is required.

Table I.II Photovoltaic characteristics of thin film devices utilizing rare metal free and non-toxic materials [5-10]

Material	Cell Eff. (%)	*FF*	V_{OC} (V)	J_{SC} (mA/cm^2)	Ref.
Cu_2O	5.38	0.67	0.80	9.99	[5]
$CuSbS_2$	3.13	0.44	0.49	14.7	[6]
$Cu_2ZnSnS_xSe_{4-x}$	12.6	0.69	0.51	35.2	[7]
SnS	4.36	0.58	0.37	20.2	[8]
Cu_2SnS_3	4.63	0.44	0.28	37.3	[9]
$ZnSnP_2$	3.44	0.59	0.47	12.3	[10]

∗ *FF* : Fill factor.

∗ J_{SC} : Short-circuit current density

1.4 Iron Pyrite

1.4.1 Iron pyrite thin film

A different alternative material is iron pyrite. Iron pyrite is recognized as a semiconductor having outstanding possibilities as a solar cell material. Iron pyrite has a band gap of about 0.95 eV, and has particularly remarkable optical absorption characteristic ($\alpha > 10^5$ cm^{-1} above 1.2 - 1.4 eV) [12, 13]. This optical absorption characteristic indicates that the film thickness of about 100 nm can absorb 90% or more of sunlight. Bulk *n*-type iron pyrite single crystals can have high majority carrier diffusion lengths (L = 0.1–1 μm) [12, 14-16]. Furthermore, iron pyrite is composed of iron and sulfur which are rare metal free and non-toxic elements. Figure 1.6 shows the theoretical material cost ratio [17]. Wadia, *et al.* simulated each material cost assuming each material has reached the theoretical limit conversion efficiency. As shown in Fig. 1.6, pyrite is sufficiently lower than other solar cell materials. Some characteristics of iron pyrite such as earth abundant and high optical absorption has the advantage that these characteristics are able to fabricate thin film solar cell at low cost.

Since iron pyrite materials have these promising properties, this material is synthesized by using a wide range of methods including chemical vapor transport [18], chemical vapor deposition [19-21], thermal sulfurization of various precursor materials [22-27], nanowires [28], and colloidal nanocrystals [29-31]. Despite the widespread progress of extensive efforts and synthesis, iron pyrite thin film photovoltaic devices have not yet obtained the conversion efficiency as shown in Table I.III [31-33]. In Table I.III, iron pyrite thin film are nanocrystals, nanocrystalline film or polycrystalline films. However, a lack of important synthetic details and specific discussion of the factors controlling the performance of these solar devices has limited the understanding of iron pyrite.

Poor performance of iron pyrite thin film photovoltaic devices include some problems. For example, (i) Controlling of quality, phase purity, stoichiometry to prepare iron pyrite films is

insufficient, (ii) Understanding the doping in iron pyrite to control carrier concentration and carrier type is insufficient, and (iii) Understanding the surface phenomena that has affected iron pyrite photovoltaic devices is not sufficiently achieved. Considering phase purity and stoichiometry, non-negligible phase fractions of the FeS_2 marcasite and $Fe_{1-\delta}S$ pyrrhotite phases have long been cited as potential causes for poor photovoltaic device performance in iron pyrite [12, 34, 35]. Recent studies of iron pyrite crystals and films including phase pure and near stoichiometry are reported by various characterization techniques, such as x-ray diffraction[21, 25, 28, 29, 31, 36-42], synchrotron x-ray diffraction [21, 38, 43], Raman spectroscopy [21, 28-31, 36, 37, 39, 42-45], magnetometry [21, 31, 39, 42, 45], and x-ray photoelectron spectroscopy [21, 38, 39, 44]. In particular, magnetometry is possible that all compounds except diamagnetic FeS_2 include magnetic property [39, 42]. Therefore, while phase purity and homogeneity are concerns in iron pyrite, they are likely not the fundamental origin of poor iron pyrite photovoltaic device performance.

Next, the doping in iron pyrite is described. Table I.IV shows the conductivity type and carrier properties of majority carriers of thin films and bulk crystals prepared by various methods [20, 21, 23-26, 29, 31, 37, 38, 43, 45-50]. As shown in Table I.IV [45], these evaluations by thermoelectric property measurements, hot-point probe measurements and Hall effect measurements show that iron pyrite thin films which have low mobility have *p*-type properties. On the other hand, high purity and unintentionally doped iron pyrite single crystals are obviously *n*-type conditions because of S vacancies (V_s) as the suspected dopants. Figure 1.7(a) shows the magnitude of the Hall coefficient R_H at room temperature as a function of the carrier mobility from previous reports of thin films and bulk crystals [24, 30, 31, 37, 43, 46-50]. On this plot in Fig. 1.7(a), blue symbols are for electron-like behavior and red symbols are for hole-like behavior. These bulk crystals have high mobility in Fig. 1.7(a) and these behaviors indicate *n*-type conduction. The small number of counterexamples often occur in naturally

occurring crystals, where impurities are a concern, or in cases where the Hall effect disagrees with the other methods such as thermopower to determine the sign of majority carriers. The complexity arises when considering unintentionally doped iron pyrite thin films.

Furthermore, the mobility of iron pyrite thin film is highly variable. These films have 200–280 $cm^2 V^{-1} s^{-1}$, which are prepared by spray pyrolysis [49] and chemical vapor deposition [51], with an additional handful of other values in 2–80 $cm^2 V^{-1} s^{-1}$ range [24, 29, 47, 48, 50]. In the great majority of cases, iron pyrite thin films have low mobility and cannot be determined exactly from Hall effect measurements. Some ubiquitous uncontrolled impurities are often hypothesized as cause that leads to high carrier concentrations and low mobility in iron pyrite thin films, although a high defect density from S vacancies also seems feasible [22, 27, 30, 52, 53]. This situation explains the modest number of thin film data points in Fig. 1.7(a), exacerbated by the fact that raw data are often not reported. The data of thin film clearly suggests *p*-type behavior in contrast to bulk crystals. As shown in Fig. 1.7(a), the Hall effect results have been reported to indicate either *n*-type [24] or *p*-type [30, 31, 47-50] majority carriers in iron pyrite thin films. However, *p*-type behavior obviously dominates.

Evaluation of carrier type by thermopower or Seebeck coefficient (*S*) measurements also forms similar conclusions. As shown in Fig. 1.7(b), *n*-type behavior in bulk crystals is confirmed from thermopower or Seebeck coefficient (*S*) measurements [46]. On the other hand, thin films show *p*-type behavior [24, 48]. However, the number of data points in Fig. 1.7(b) are not impressive because some measurements record only the sign of seebeck coefficient not value. As shown in Table IV, these measurements by thermopower and hot point probe methods are in almost universal support of *p*-type conduction in low mobility iron pyrite thin films. In conclusion, the observations summarized in Table I.IV and Fig. 1.7 have led to the notion that unintentionally doped iron pyrite single crystals show *n*-type behavior, whereas unintentionally doped iron pyrite thin films show *p*-type behavior [45]. While some ubiquitous impurities and

detects might be unintentionally introduced in iron pyrite thin films, the fundamental understanding has not obtained yet.

Finally, the effect of surface phenomena for iron pyrite photovoltaic devices is explained in section 1.4.2.

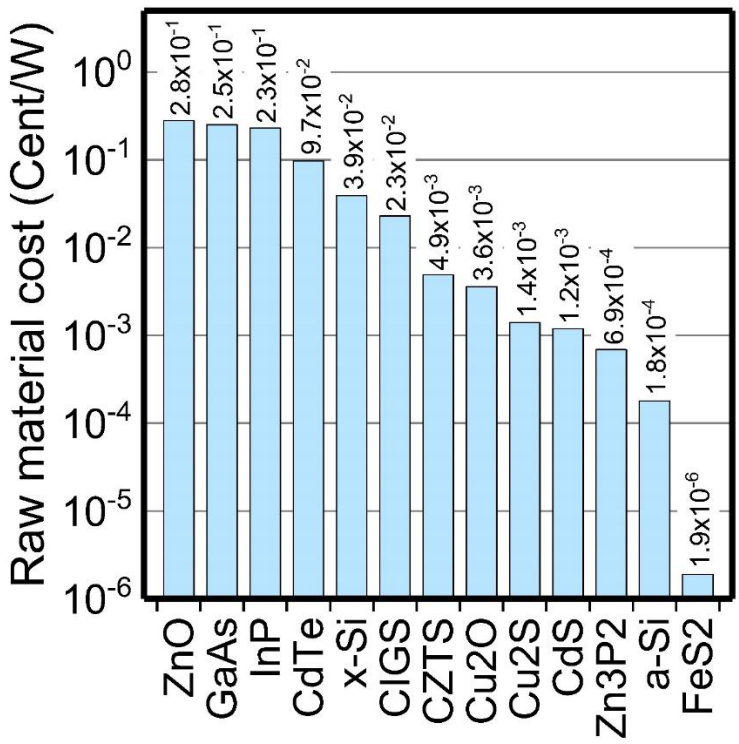

Fig. 1.6 Material cost for inorganic photovoltaic materials. Component cost contribution in cent/W is a strong indicator of value for future deployment [17].

Table I.III Previous reports of Iron pyrite (FeS_2) thin film solar cells and conversion efficiencies [32-34].

Eff. (%)	Device structure	Ref.
0	IZO/AZO/*n*-CdS/*p*-FeS_2/Mo	[32]
0	ITO/*n*-ZnO/*n*-CdS/*p*-FeS_2/Au	[33]
0	ITO/*n*-ZnO/*n*-CdS/*p*-FeS_2/*n*-MoO_3/Al	[34]

Table I.IV Literature review of carrier types in unintentionally doped FeS_2 from Hall effect and thermopower [45]. This table was drawn from [21, 22, 24-27, 30, 32, 38, 39, 44, 47-51]

FeS_2	Synthesis method	Majority carrier	Properties	Ref.
Thin film	Sulfidation of Fe	Electron	ρ(300K) = 0.1 Ωcm S(300K) = 6.7 μVK^{-1}	[25]
Thin film	Sulfidation of Fe	Hall	S(300K) = 70-80 μVK^{-1}	[24]
Thin film	Sulfidation of Fe	Hall	ρ(300K) = 0.50-0.58 Ωcm	[26]
Thin film	Plasma-assisted sulfidation of Fe	Hall	ρ(300K) = 1 Ωcm	[27]
Thin film	Annealing of $Fe(acac)_3$ ink	Hall	ρ(300K) = 1.35 Ωcm	[39]
Thin film	FeS_2 nanocrystal coating	Hall	μ_H(300K) = 80 $cm^2V^{-1}s^{-1}$	[30]
Thin film	FeS_2 nanocrystal coating	Hall	ρ(300K) = 11.2 Ωcm μ_H(300K) = 0.1 $cm^2V^{-1}s^{-1}$	[32]
Thin film	Spray pyrolysis	Hall	ρ(300K) = 0.59 Ωcm μ_H(300K) = 2.12 $cm^2V^{-1}s^{-1}$	[51]
Thin film	Spray pyrolysis	Hall	ρ(300K) = 0.425 Ωcm μ_H(300K) = 210 $cm^2V^{-1}s^{-1}$	[50]
Thin film	Reactive sputtering (Fe target)	Hall	ρ(300K) = 0.003 Ωcm S(300K) = 10 μVK^{-1} μ_H(300K) = 25 $cm^2V^{-1}s^{-1}$	[49]
Thin film	Reactive sputtering (FeS_2 target)	Hall	ρ(300K) = 0.25 Ωcm μ_H(300K) = 5 $cm^2V^{-1}s^{-1}$	[48]
Thin film	CVD	Hall	ρ(300K) = 1 Ωcm S(300K) = 50 μVK^{-1}	[21]
Thin film	CVD	Hall	ρ(300K) = 1.5 Ωcm	[22]
Syn. crystal	CVT	Electron	ρ(300K) = 2.1 Ωcm S(300K) = 320 μVK^{-1} μ_H(300K) = 172 $cm^2V^{-1}s^{-1}$	[47]
Syn. crystal	CVT	Hall	ρ(300K) = 142 Ωcm μ_H(300K) = 5.3 $cm^2V^{-1}s^{-1}$	[47]
Syn. crystal	CVT	Electron	ρ(300K) = 114 Ωcm μ_H(300K) = 50 $cm^2V^{-1}s^{-1}$	[38]
Syn. crystal	Flux	Electron	ρ(300K) = 5.1 Ωcm μ_H(300K) = 245 $cm^2V^{-1}s^{-1}$	[44]

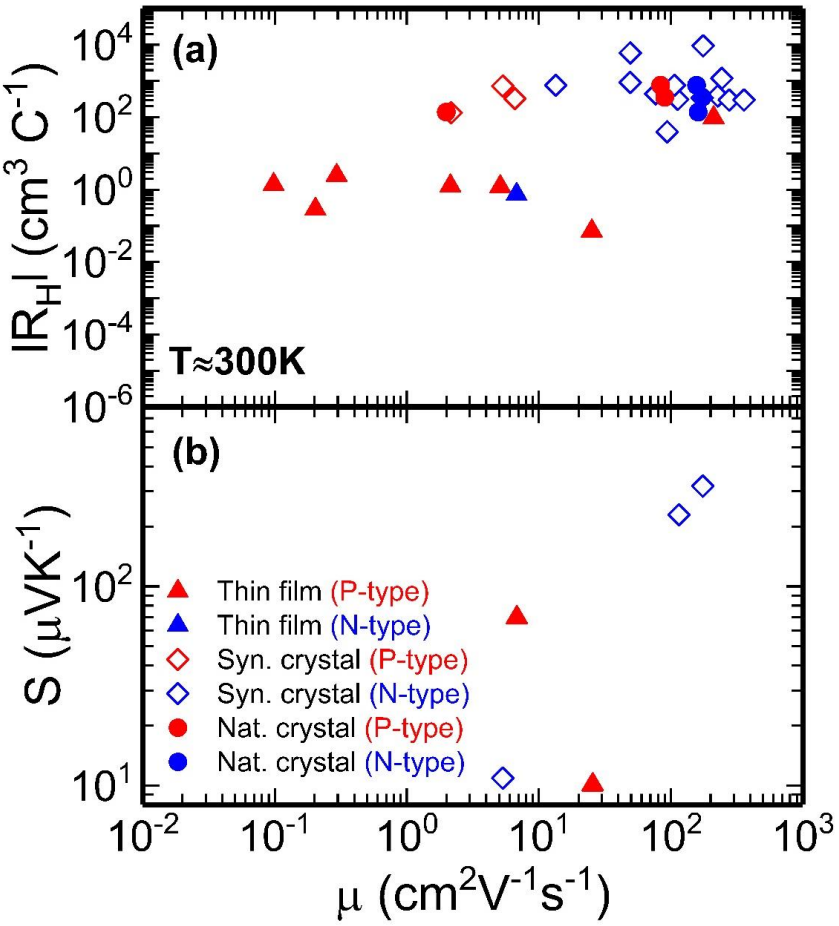

Fig. 1.7 Summary of the literature on carrier type in unintentionally doped iron pyrite from Hall effect and thermopower [45]. (a)The room temperature Hall coefficient (R_H) [25, 31, 32, 38, 44, 47-51] (b) Seebeck coefficient (S) vs Hall carrier mobility (μ) for the polycrystalline films and synthetic single crystals [25, 47, 49].

1.4.2 Iron pyrite bulk crystal

Iron pyrite thin films are prepared by various methods, however they yield poor properties as a photovoltaic device. Therefore, iron pyrite bulk crystals including high pure phase are suitable to understand and improve some properties for fabricating photovoltaic devices. Iron pyrite photovoltaic device using single crystal has already been reported as low as 2.8% of the solar energy conversion efficiency [12]. This efficiency was reported for a photoelectrochemical (PEC) solar cell using a CVT grown, unintentionally doped *n*-type pyrite single crystal and an iodine/iodide aqueous electrolyte with little experimental detail [12]. The photoanode reached an outstanding photocurrent of 42 mA/cm^2 at short-circuit current density (J_{SC}), however its efficiency was ultimately limited by a low open-circuit voltage ($V_{OC} \leq 187$ mV) and moderate fill factor (FF~50%) [12]. The highest efficiency of iron pyrite photovoltaic device has remained 2.8% since the beginning of the 1990s. Therefore, understanding the reason for the low performance is essential to improve iron pyrite photovoltaic devices.

Low V_{OC} of iron pyrite photovoltaic devices include some problems. For example, (i) Decreasing band gap at surface region of iron pyrite bulk crystals, (ii) Fermi level pinning and band bending based on ligand field theory (LFT), and (iii) Inversion layer at surface region.

As the first explanation of the low V_{OC} of iron pyrite photovoltaic device, scanning tunneling spectroscopy (STS) measurements were taken on {100}-faced iron pyrite single crystals synthesized by chemical vapor transport in closed quartz ampoules [54]. This report suggests that the band gap at surface can be as small as 0.4 eV although the band gap in bulk corresponds 0.95 eV [54]. This surface gap has also been indicated from density functional calculations, where the band gap was found to be a function of stoichiometry [55, 56]. Low density states resulting in an ill-defined conduction band onset are an issue even in bulk pyrite [57, 58]. In fact, this general area of research clearly warrants further work.

As the second explanation for the low V_{OC} of iron pyrite, the existence of intrinsic defect

states at surface region are hypothesized as cause that leads to Fermi level pinning and surface recombination. X-ray photoelectron spectroscopy for UHV cleaved {100}-faced *n*-type pyrite single crystals and natural bulk crystals revealed pinning of the Femi level near the valence band edge at surface or iron pyrite [59, 60]. These surface conditions are modeled by ligand field theory (LFT) modeling based on Fe-S coordination [61]. Reducing Fe coordination at surface region forms the intrinsic defect states at the valence band edge, which leads to Fermi level pinning and subsequent band bending [12, 61, 62]. LFT modeling are accounted for the low photovoltages of metal/*n*-FeS_2 junctions which create the leaky tunnel barriers [12, 61, 62]. However, experimental evidence for LFT modeling has not been confirmed yet.

As the third explanation for the low V_{OC} of iron pyrite, the inversion layer at surface region is suggested as the cause of low V_{OC} [43]. This inversion layer was reported as the impact of surface phenomena on bulk electronic transport. As shown in Fig. 1.8, Limpinsel *et al.* observed surface dominated conduction at low temperature in polished flux-grown *n*-type iron pyrite single crystals [43]. Based on Ultraviolet photoelectron spectroscopy and Hall effect measurements, they concluded that Fermi level was pinned above the valence band maximum in iron pyrite single crystal and formed *p*-type surface conductive layer decreased the low V_{OC} in iron pyrite photovoltaic devices shown in Fig. 1.9. Although the evidence for surface conduction presented is strong, there are still some uncertainties as to whether the surface layer is definitely *p*-type. As shown in Fig. 1.8, the sign of Hall coefficient fluctuate between small positive and negative values at low temperature. This phenomenon is different from two-channel conduction model based on an inversion layer at surface region which Limpinsel *et al.* supposed. In addition, they could not obtain foundation that the Mott variable range hopping (Mott-VRH) conduction did not occur. Therefore, further verification is necessary.

As described above, while various problems about low V_{OC} in iron pyrite photovoltaic device have been pointed out, suitable solutions have not been founded yet. However, iron

pyrite single crystals still provide the most well-defined platform to characterize and understand the physical and electrical characteristics, which can then serve as a foundation to evaluate their impacts on different iron pyrite materials.

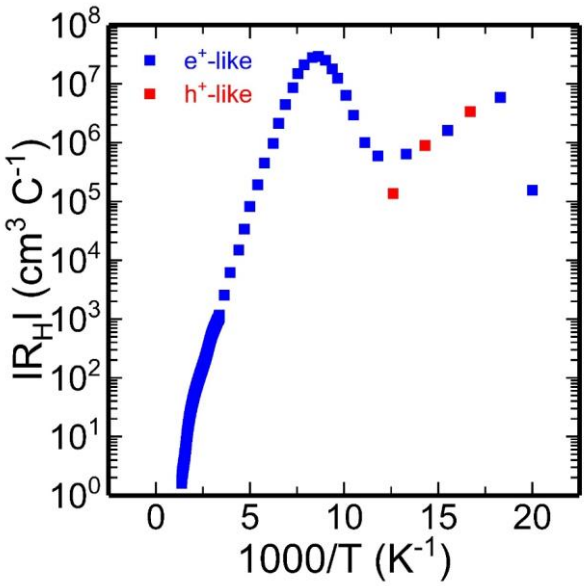

Fig. 1.8 The Hall coefficient data for an iron pyrite single crystal wafer depending temperature [44].

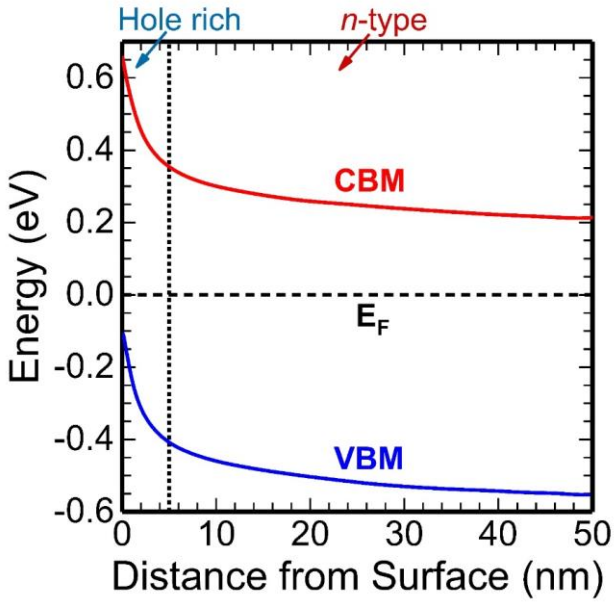

Fig. 1.9 Calculated equilibrium band diagram of the iron pyrite based on data of Hall effect measurement [44].

1.5 Purpose of This Dissertation

As described above, there are many problems about poor performances of iron pyrite photovoltaic devices. In particular, an inversion layer at the surface region of iron pyrite has the potential to cause poor photovoltaic performance. In this thesis, the inversion layer at the surface of iron pyrite has been studied to understand and improve the cause of the poor device performance as shown in Fig. 1.10.

In Chapter 2, an effect of the inversion layer of iron pyrite surface for iron pyrite thin film photovoltaic performance is investigated by utilizing the two-dimensional (2D) device simulator, ATLAS. Photovoltaic device including the inversion layer of iron pyrite layer is modeled and photovoltaic characteristics of the device is calculated. Based on the results obtained, not only the improvement of an inversion layer at surface of iron pyrite but also decreasing bulk defects are essential to fabricate high performance iron pyrite thin film photovoltaic devices. In Chapter 2, my documents which already have been published are quoted [63].

In Chapter 3, iron pyrite single crystal is synthesized by flux method and surface conditions of grown iron pyrite single crystal are evaluated to establish a method of removing oxidation layer at surface region of iron pyrite single crystal. In this chapter, iron pyrite single crystal instead of iron pyrite thin film is utilized for evaluation of the surface conditions because unstable phase purity and poor film quality in iron pyrite thin film might affect evaluations of band structure and electrical characteristic. To evaluate the surface conditions of iron pyrite single crystal, Micro-Raman spectroscopy and X-ray photoelectron spectroscopy (XPS) are performed. From analysis of XPS, chemical-bonding state at iron pyrite surface is discussed.

In Chapter 4, band structure is evaluated by utilizing Photoelectron yield spectroscopy (PYS), Kelvin Force Microscope (KFM) and optical characteristic measurements. In addition, electrical transport characteristics are evaluated by Hall effect measurement. From the

evaluations of band structure and electrical transport characteristic, problems for improvement of characteristics are discussed toward realizing high performance iron pyrite photovoltaic device.

In Chapter 5, the conclusion of this study and future outlook are summarized. In addition, the limit of the proposed method are described, and suggestions for future work to solve these problems are proved.

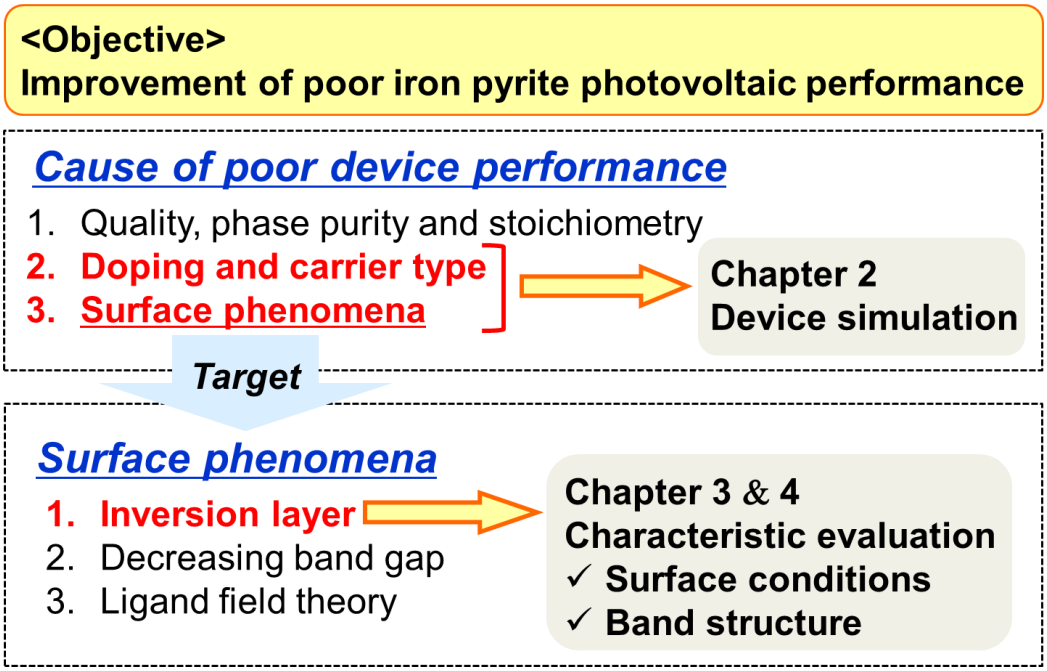

Fig. 1.10 Outline of this thesis.

Reference

[1] R. Corporation, Taiyoukou hatsuden sangyou hattenhenoteigen (PV150), (2017) p.6.

[2] National Renewable Energy Laboratory (NREL), Best research-cell efficiencies, (2018).

[3] W. Shockley, J. Appl. Phys. 32 (1961) 510-519.

[4] Recent development of thin film compound semiconductor photovoltaic cells, (2007) CMC, p.8.

[5] T. Minami, T. Miyata, Y. Nishi, Sol. Energ. 105 (2014) 206-217.

[6] W. Septina, S. Ikeda, Y. Iga, T. Harada, M. Matsumura, Thin Solid Films 550 (2014) 700-704.

[7] W. Wang, M.T. Winkler, O. Gunawan, T. Gokmen, T.K. Todorov, Y. Zhu, D.B. Mitzi, Adv. Energ. Mater. 4 (2014) 5.

[8] R. Jaramillo, V. Steinmann, C. Yang, K. Hartman, R. Chakraborty, J.R. Poindexter, M.L. Castillo, R. Gordon, T. Buonassisi, J. Vis. Exp. 99 (2015) e52705.

[9] M. Nakashima, J. Fujimoto, T. Yamaguchi, M. Izaki, Appl. Phys. Express 8 (2015) 042303.

[10] S. Akari, J. Chantana, S. Nakatsuka, Y. Nose, T. Minemoto, Sol. Energy Mater. Sol. Cells 174 (2018) 412-417.

[11] T. Kato, N. Sakai, H. Sugimoto, Ieee, IEEE, New York, 2014.

[12] A. Ennaoui, S. Fiechter, N. Pettenkofer, N. Alonso‐Vante, K. Büker, M. Bronold, C. Höpfner, H. Tributsch, Sol. Energy Mater. Sol. Cells 29 (1993) 289-427.

[13] A. Ennaoui, S. Fiechter, H. Goslowsky, H. Tributsch, J. Electrochem. Soc. 132 (1985) 1579-1582.

[14] A. Ennaoui, H. Tributsch, Sol. Energ. Mater. 14 (1986) 461-474.

[15] K. Büker, N. Alonso‐Vante, H. Tributsch, J. Appl. Phys. 72 (1992) 5721-5728.

[16] P. P. Altermatt, T. Kiesewetter, K. Ellmer, H. Tributsch, Sol. Energy Mater. Sol. Cells 71 (2002) 181-195.

[17] C. Wadia, A. P. Alivisatos, D. M. Kammen, Environ. Sci. Technol. 43 (2009) 2072-2077.

[18] S. Fiechter, J. Mai, A. Ennaoui, W. Szacki, J. Cryst. Growth 78 (1986) 438-444.

[19] C. Höpfner, K. Ellmer, A. Ennaoui, C. Pettenkofer, S. Fiechter, H. Tributsch, J. Cryst. Growth 151 (1995) 325-334.

[20] B. Thomas, T. Cibik, C. Höpfner, K. Diesner, G. Ehlers, S. Fiechter, K. Ellmer, J. Mater. Sci.: Mater. Electron. 9 (1998) 61-64.

[21] N. Berry, M. Cheng, C. L. Perkins, M. Limpinsel, J. C. Hemminger, M. Law, Adv. Energ. Mater. 2 (2012) 1124-1135.

[22] J. R. Ares, M. Leon, N. M. Arozamena, J. Sanchez-Paramo, P. Celis, I. J. Ferrer, C. Sanchez, J. Phys.: Condens. Matter 10 (1998) 4281-4289.

[23] J. R. Ares, I. J. Ferrer, F. Cuevas, C. R. S´anchez, Thin Solid Films 387 (2001) 97-99.

[24] J. R. Ares, I. J. Ferrer, C. R. Sánchez, Thin Solid Films 431-432 (2003) 511-513.

[25] R. J. Soukup, P. Prabukanthan, N. J. Ianno, A. Sarkar, C. A. Kamler, D. G. Sekora, J. Vac. Sci. Technol. A 29 (2011) 011001.

[26] S. Bausch, B. Sailer, H. Keppner, G. Willeke, E. Bucher, G. Frommeyer, Appl. Phys. Lett. 57 (1990) 25-27.

[27] G. Smestad, A. Ennaoui, S. Fiechter, H. Tributsch, W. K. Hofmann, M. Birkholz, W. Kautek, Sol. Energ. Mater. 20 (1990) 149-165.

[28] M. Caban-Acevedo, M. S. Faber, Y. Tan, R. J. Hamers, S. Jin, Nano Lett. 12 (2012) 1977-1982.

[29] Y. Bi, Y. Yuan, C. L. Exstrom, S. A. Darveau, J. Huang, Nano Lett. 11 (2011) 4953-4957.

[30] T. Kinner, K. P. Bhandari, E. Bastola, B. M. Monahan, N. O. Haugen, P. J. Roland, T. P. Bigioni, R. J. Ellingson, J. Phys. Chem. C 120 (2016) 5706-5713.

[31] S. Shukla, G. Xing, H. Ge, R. R. Prabhakar, S. Mathew, Z. Su, V. Nalla, T. Venkatesan, N. Mathews, T. Sritharan, T. C. Sum, Q. Xiong, ACS Nano 10 (2016) 4431-4440.

[32] C. Steinhagen, T. B. Harvey, C. J. Stolle, J. Harris, B. A. Korgel, J. phys. chem. lett. 3 (2012) 2352-2356.

[33] D. G. Moon, A. Cho, J. H. Park, S. Ahn, H. Kwon, Y. S. Cho, S. Ahn, J. Mater. Chem. A 2 (2014) 17779-17786.

[34] R. Sun, M. K. Y. Chan, G. Ceder, Phys. Rev. B 83 (2011) 235311.

[35] L. Yu, S. Lany, R. Kykyneshi, V. Jieratum, R. Ravichandran, B. Pelatt, E. Altschul, H.A.S. Platt, J.F. Wager, D.A. Keszler, A. Zunger, Adv. Energ. Mater. 1 (2011) 748-753.

[36] M. Caban-Acevedo, D. Liang, K. S. Chew, J. P. DeGrave, N. S. Kaiser, S. Jin, ACS Nano 7 (2013) 1731-1739.

[37] M. Caban-Acevedo, N. S. Kaiser, C. R. English, D. Liang, B. J. Thompson, H. E. Chen, K. J. Czech, J. C. Wright, R. J. Hamers, S. Jin, J. Am. Chem. Soc. 136 (2014) 17163-17179.

[38] S. Seefeld, M. Limpinsel, Y. Liu, N. Farhi, A. Weber, Y. Zhang, N. Berry, Y. J. Kwon, C. L. Perkins, J. C. Hemminger, R. Wu, M. Law, J. Am. Chem. Soc. 135 (2013) 4412-4424.

[39] X. Zhang, T. Scott, T. Socha, D. Nielsen, M. Manno, M. Johnson, Y. Yan, Y. Losovyj, P. Dowben, E. S. Aydil, C. Leighton, ACS Appl. Mater. Inter. 7 (2015) 14130-14139.

[40] J. Puthussery, S. Seefeld, N. Berry, M. Gibbs, M. Law, J. Am. Chem. Soc. 133 (2011) 716-719.

[41] J. M. Lucas, C. C. Tuan, S. D. Lounis, D. K. Britt, R. Qiao, W. Yang, A. Lanzara, A.P. Alivisatos, Chem. Mater. 25 (2013) 1615-1620.

[42] X. Zhang, M. Manno, A. Baruth, M. Johnson, E. S. Aydil, C. Leighton, ACS Nano 7 (2013) 2781-2789.

[43] M. Limpinsel, N. Farhi, N. Berry, J. Lindemuth, C. L. Perkins, Q. Lin, M. Law, Energy Environ. Sci. 7 (2014) 1974-1989.

[44] R. Morrish, R. Silverstein, C. A. Wolden, J. Am. Chem. Soc. 134 (2012) 17854-17857.

[45] X. Zhang, M. Li, J. Walter, L. O'Brien, M. A. Manno, B. Voigt, F. Mork, S. V. Baryshev,

J. Kakalios, E. S. Aydil, C. Leighton, Phys. Rev. Mater. 1 (2017) 015402.

[46] G. Willeke, O. Blenk, C. Kloc, E. Bucher, J. Alloys Compd. 178 (1992) 181-191.

[47] G. Willeke, R. Dasbach, B. Sailer, E. Bucher, Thin Solid Films 213 (1992) 271-276.

[48] D. Lichtenberger, K. Ellmer, R. Schieck, S. Fiechter, H. Tributsch, Thin Solid Films 246 (1994) 6-12.

[49] A. Yamamoto, M. Nakamura, A. Seki, E. L. Li, A. Hashimoto, S. Nakamura, Sol. Energy Mater. Sol. Cells 75 (2003) 451-546.

[50] S. Shukla, N. H. Loc, P. P. Boix, T. M. Koh, R. R. Prabhakar, H. K. Mulmudi, J. Zhang, S. Chen, C. F. Ng, C. H. A. Huan, N. Mathews, T. Sritharan, Q. Xiong, ACS Nano 8 (2014) 10597-10605.

[51] N. Takahashi, Y. Nakatani, T. Yatomi, T. Nakamura, Chem. Mater. 15 (2003) 1763-1765.

[52] J. .Oertel, K. Ellmer, W. Bohne, J. Röhrich, H. Tributsch, J. Cryst. Growth 198-199 (1999) 1205-1210.

[53] R. Sun, M. K. Y. Chan, S. Kang, G. Ceder, Phys. Rev. B 84 (2011) 035212.

[54] F. W. Herbert, A. Krishnamoorthy, K. J. Van Vliet, B. Yildiz, Surf. Sci. 618 (2013) 53-61.

[55] D. R. Alfonso, J. Phys. Chem. C 114 (2010) 8971-8980.

[56] Y. N. Zhang, J. Hu, M. Law, R.Q. Wu, Phys. Rev. B 85 (2012) 085314.

[57] J. Hu, Y. Zhang, M. Law, R. Wu, Phys. Rev. B 85 (2012) 085203.

[58] P. Lazic, R. Armiento, F. W. Herbert, R. Chakraborty, R. Sun, M.K. Chan, K. Hartman, T. Buonassisi, B. Yildiz, G. Ceder, J. Phys.: Condens. Matter 25 (2013) 465801.

[59] C. Pettenkofer, W. Jaegermann, M. Bronold, Ber. Bunsenges. Phys. Chem. 95 (1991) 560-565.

[60] M. Bronold, C. Pettenkofer, W. Jaegermann, J. Appl. Phys. 76 (1994) 5800-5808.

[61] M. Bronold, Y. Tomm, W. Jaegermann, Sur. Sci. Lett. 314 (1994) L931-L936.

[62] M. Bronold, K. Büker, S. Kubala, C. Pettenkofer, H. Tributsch, Phys. Status Solidi A 135

(1993) 231-243.

[63] S. Uchiyama, Y. Ishikawa, Y. Uraoka, Jpn. J. Appl. Phys. 57 (2018) 032301.

Chapter 2

Investigation on the Effect of Inversion Layer at Iron Pyrite Surface on Photovoltaic Device by Two-dimensional Device Simulation

2.1 Introduction

Iron pyrite is a candidate photovoltaic device material because of its strong optical absorption ($\alpha > 10^5$ cm^{-1} for $h\nu > 1.3$ eV), earth-abundance and low cost [1, 2]. Moreover, bulk *n*-type iron pyrite single crystal has high majority carrier mobility (> 300 cm^{2}V^{-1}s^{-1}) and long minority carrier diffusion length (0.1 – 1 μm) [2, 3]. Therefore, iron pyrite thin films have been prepared by various methods such as chemical vapor deposition [4-6], thermal sulfurization of some precursor materials [7-12], nanowires [13], and nanocrystals [14-16]. While these iron pyrite thin film photovoltaic devices are fabricated, these photovoltaic devices have not become commercially available because of poor conversion efficiency [16-18].

In this Chapter, device simulation was performed to investigate the cause of poor performance of iron pyrite thin film photovoltaic devices which have been fabricated in the past, and to understand the effects of the density of states at the deep donor level and the inversion layer on the iron pyrite photovoltaic devices. To clarify the problems in realizing iron pyrite photovoltaic devices, device simulation considering the density of states in iron pyrite was performed. In this Chapter, a two-dimensional (2D) device simulator, ATLAS (Silvaco), was utilized to carry out the numerical simulation and design of an iron pyrite photovoltaic device

on the basis of the drift-diffusion transport model, which consists of a set of fundamental equations including Poisson's equation. Poisson's equation relates variations in electrostatic potential to local charge densities.

2.2 Fundamental Equations

Poisson's Equation relates the electrostatic potential to the space charge density as shown in Eq. (2.1):

$$\mathbf{div}(\boldsymbol{\varepsilon}\nabla\boldsymbol{\psi}) = -\boldsymbol{\rho} \tag{2.1}$$

As seen, ψ is the electrostatic potential, ε is the local permittivity, and ρ is the local space charge density. The continuity equations for electrons and holes are defined by Eq. (2.2) and (2.3):

$$\frac{\partial n}{\partial t} = \frac{1}{q} div\overrightarrow{J_n} + G_n - R_n \tag{2.2}$$

$$\frac{\partial p}{\partial t} = -\frac{1}{q} div\overrightarrow{J_p} + G_p - R_p \tag{2.3}$$

Here, n and p are the electron and hole concentration, and $\overrightarrow{J_n}$ and $\overrightarrow{J_p}$ are the electron and hole current densities, G_n and G_p are the generation rates for electrons and holes, R_n and R_p are the recombination rates for electrons and holes, and q is the magnitude of the charge on an electron. Derivations based upon the Boltzmann transport theory have shown that the current densities in the continuity equations may be approximated by a drift-diffusion model. In this case, the more conventional formulation of drift-diffusion equations to be written by Eq. (2.4) and (2.5).

$$\overrightarrow{J_n} = qn\mu_n\overrightarrow{E_n} + qD_n\nabla n \tag{2.4}$$

$$\overrightarrow{J_p} = qp\mu_p\overrightarrow{E_p} - qD_p\nabla p \tag{2.5}$$

Here, μ_n and μ_p are the electron and hole mobilities, D_n and D_p are the diffusion coefficients for electron and hole, and effective fields are normally defined by Eq. (2.6) and (2.7).

$$\overrightarrow{E_n} = -\nabla\left(\psi + \frac{kT_L}{q} ln n_{ie}\right) \quad (2.6)$$

$$\overrightarrow{E_p} = -\nabla\left(\psi - \frac{kT_L}{q} ln n_{ie}\right) \quad (2.7)$$

Here, n_{ie} is the effective intrinsic concentration and T_L is the lattice temperature.

From Eq. (2.2) and (2.3), G_n and G_p are the generation rates for electrons and holes. In case of Photo-generation rate, it is possible to generate electron-hole pairs inside the device by exposing a photovoltaic device to light. The relationship between the photo-generation and the absorption of irradiation light is given by Eq. (2.8).

$$\mathbf{G(x)} = \int G(x,\lambda)d\lambda = \int \frac{\lambda}{hc} Int.(\lambda)\alpha(\lambda)\exp(-\alpha(\lambda)x)\,d\lambda \quad (2.8)$$

Where $G(x)$ is a total photo-generation rate at a distance x from the front surface, λ is the wavelength of the incident light, $Int.(\lambda)$ is the intensity of the light, (hc/λ) is the energy of the absorbed photon, and $\alpha(\lambda)$ is the absorption coefficient.

From Eq. (2.2) and (2.3), R_n and R_p are the recombination rates for electrons and holes. In the ATALS device simulator, the Shockley-Read-Hall (SRH) recombination model was utilized to calculate carrier recombination rates. In this time, density of states are applied to each layer in the device. To model an inversion layer at the surface of iron pyrite, I divided the pyrite layer into two components, bulk and the surface, which is the inversion layer, and this model utilized the density of states. Here, Eq. (2.9) shows the SRH recombination model utilizing the density of states in the band gap.

$$R_{n,p} = \int_{E_V}^{E_C} \left\{ \frac{v_n v_p \sigma_{nA}\sigma_{pA}(np - n_i^2) g_{GA}(E)}{v_n\sigma_{nA}\left[n + n_i exp\left(\frac{E - E_i}{kT}\right)\right] + v_p\sigma_{pA}\left[p + n_i exp\left(\frac{E_i - E}{kT}\right)\right]} \right\} dE + \int_{E_V}^{E_C} \left\{ \frac{v_n v_p \sigma_{nD}\sigma_{pD}(np - n_i^2) g_{GD}(E)}{v_n\sigma_{nD}\left[n + n_i exp\left(\frac{E - E_i}{kT}\right)\right] + v_p\sigma_{pD}\left[p + n_i exp\left(\frac{E_i - E}{kT}\right)\right]} \right\} dE \quad (2.9)$$

At a steady state, ideal recombination of electrons and holes occurs. n and p are the electron

and hole concentrations, respectively, n_i is the intrinsic carrier density, E_i is the Fermi level, k is the Boltzmann constant, and T is the absolute temperature. The $g_{GA}(E)$ and $g_{GD}(E)$, which are corresponds to Gaussian distributions, are described as deep defect levels of the acceptor and donor. Eqs. (2.10) and (2.11) are the density of states was modeled with a Gaussian distribution at a localized energy level of the acceptor and donor defect distributions.

$$\boldsymbol{g_{GA}(\mathrm{E}) = N_{GA}\exp\left[-\left(\frac{E_{GA}-E}{W_{GA}}\right)^2\right]} \quad (\mathbf{2.10})$$

$$\boldsymbol{g_{GD}(\mathrm{E}) = N_{GD}\exp\left[-\left(\frac{E-E_{GD}}{W_{GD}}\right)^2\right]} \quad (\mathbf{2.11})$$

Here, defect energy is E, and the subscripts G, A, and D stand for Gaussian, acceptor, and donor defect states, respectively. The density of states is characterized by the acceptor and donor levels of density of states N_{GA} and N_{GD}, the decay energies W_{GA} and W_{GD}, and the peak energy positions E_{GA} and E_{GD}.

From Eq. (2.9), the capture cross sections σ_n and σ_p are calculated from the carrier lifetimes τ_p and τ_n as below in Eqs. (2.12) and (2.13). τ_p and τ_n are the carrier lifetimes, and v_{th} is the thermal velocity of the carriers and N_t is the concentration of the defect level.

$$\boldsymbol{\sigma_n = \frac{1}{\tau_n v_{th} N_t}} \quad (\mathbf{2.12})$$

$$\boldsymbol{\sigma_p = \frac{1}{\tau_p v_{th} N_t}} \quad (\mathbf{2.13})$$

2.3 Simulation Parameters

FeS_2 (Iron pyrite)

To model the inversion layer at iron pyrite surface, the simulation parameters were defined for bulk region and surface region of iron pyrite as FeS_2 bulk layer and FeS_2 surface layer, respectively. The simulation parameters of FeS_2 bulk and FeS_2 surface were defined using previously reported values [19, 20]. Table II.I shows the material parameters or FeS_2 bulk layer and FeS_2 surface layer. The parameters of the defect levels in FeS_2 bulk and FeS_2 surface were determined in a previous study, and they were obtained by density functional theory (DFT) calculation [20]. Table II.I shows the parameters of defect levels of FeS_2 bulk layer and FeS_2 surface layer. The DFT calculation reflects the model of the inversion layer at iron pyrite surface shown in Fig. 1.9. The optical properties such as fefractive index $n(\lambda)$ and extinction coefficient $k(\lambda)$ of FeS_2 bulk layer and FeS_2 surface layer are defined from previously reported values [21].

ZnO, CdS and MoO_3 (ITO/ZnO/CdS/FeS_2/MoO_3/Al device)

To demonstrate the previously reported results in simulation model, an ITO/ZnO/CdS/FeS_2/MoO_3/Al photovoltaic device had been fabricated in the past [18] was modeled and calculated by ATLAS. In some previous reports, *n*-CdS/*p*-FeS_2 hetero-junction photovoltaic devices were fabricated because the carrier type of FeS_2 thin film was regarded as *p*-type and *p*-FeS_2 photovoltaic devices were considered to an alternative devices for Cu(In,Ga)(Se,S)$_2$ photovoltaic devices [16-18]. In this time, an ITO/ZnO/CdS/FeS_2/MoO_3/Al photovoltaic device was utilized because device structure and *I–V* characteristics were detailed in comparison with other reports [16-18]. This modeling utilized the *n*-FeS_2 bulk layer and *p*-FeS_2 surface layer as optical absorption layer. While previous report considered that the carrier type of FeS_2 thin film was *p*-type, this modeling regard that the carrier type of *n*-FeS_2 was recognized as *p*-type due to the inversion layer. In this device, In-doped SnO_2 (ITO), ZnO,

MoO_3, and Al were utilized as transparent conductive film, window layer, hole-transporting layer, and back electrode, respectively [18]. All the parameters of ZnO and CdS were defined using material data in ATLAS, except for the electron and hole mobility of ZnO [22, 23]. In addition, some parameters of MoO_3 were defined from material data of previous reports and ATLAS [23-27]. Table II.III shows the material parameters of ZnO, CdS and MoO_3. On the other hand, the density of states without peak energy positions of ZnO, CdS, and MoO_3 are all default parameters of ATLAS, while the peak energy positions of the defect level are defined from the reported defect level; E_{GD} of ZnO, CdS, and MoO_3 are 3.1, 2.2, and 2.7 eV, respectively [23, 28-30]. Table II.IV shows the parameters of defect levels of ZnO, CdS and MoO_3. Defect levels of MoO_3 was obtained by DFT calculation, that of CdS by photoinduced current transient spectroscopy, and that of ZnO by deep level transient spectroscopy. Furthermore, the optical properties of ZnO, and CdS were defined from material data in ATLAS.

Cu_2O (ITO/Cu_2O/FeS_2/Al device)

To examine the effect of inversion layer at iron pyrite surface for iron pyrite photovoltaic characteristics, ITO/Cu_2O/FeS_2/Al photovoltaic device was modeled. In this modeling, both *n*-FeS_2 bulk layer and *p*-FeS_2 surface layer were utilized as optical absorption layer like ITO/ZnO/CdS/FeS_2/MoO_3/Al device. On the other hand, the *p*-Cu_2O was utilized as window layer toward formation of *p*-Cu_2O/*n*-FeS_2 hetero-junction because the band gap of Cu_2O was 2.1 eV. Cu_2O, NiO, and SnO are well-known *p*-type semiconductors with wide band gaps. In this modeling, Cu_2O is utilized because the data for Cu_2O, such as density of states, has been extensively studied allowing the incorporation of the material properties in device simulation [31]. Cu_2O were defined from material data of previous reports and ATLAS shown as Table II.V [23, 32-35]. In addition, Table II.VI shows the parameters of the defect levels of Cu_2O. The density of states without peak energy positions of Cu_2O are all default parameters of

ATLAS, while the peak energy positions of the defect level are defined from the reported defect level; E_{GA} of Cu_2O is 1.65 eV [23, 31]. Defect level of Cu_2O was obtained by DFT calculation

Electrode

The resistivity and work function of ITO are 540 μΩ·cm and 5.15 eV, and the resistivity and work function of Al are 2.65 μΩ·cm and 4.2 eV, respectively. Optical properties of ITO were defined from material data in ATLAS.

Table II.I. Material parameters of FeS_2 bulk layer and FeS_2 surface layer utilized in the simulation [19, 20]

Layer properties	FeS_2 Bulk	FeS_2 Surface
Band gap : E_g (eV)	0.8	0.8
Electron affinity : χ_e (eV)	4.45	4.45
Relative permittivity : ε_r (F cm^{-1})	11	11
Electron mobility : μ_n (cm^2/V s)	245	1
Hole mobility : μ_p (cm^2/V s)	82	1
Conduction band effective density of states : N_C (cm^{-3})	3.0×10^{18}	3.0×10^{18}
Valence band effective density of states : N_V (cm^{-3})	8.5×10^{19}	8.5×10^{19}

Table II.II. Parameters of defect levels of FeS_2 bulk layer and FeS_2 surface layer utilized in the simulation [20]

Gaussian defect states	FeS_2 Bulk	FeS_2 Surface
Gaussian defect density (cm^{-3})	N_{GD} : 6.3×10^{18}	N_{GA} : 1.0×10^{19}
Peak energy position (eV)	E_{GD} : 0.56	E_{GA} : 0.75
Decay energy (eV)	W_{GD} : 0.05	W_{GA} : 0.01
σ_n (cm^2)	3.0×10^{-15}	1.9×10^{-15}
σ_p (cm^2)	3.0×10^{-15}	1.9×10^{-15}

Table II.III. Material parameters utilized in the simulation [22-27]

Layer properties	ZnO	CdS	MoO_3
Band gap : E_g (eV)	3.37	2.48	3.0
Electron affinity : χ_e (eV)	4.5	4.18	5.5
Relative permittivity : ε_r (F cm^{-1})	2	10	12
Electron mobility : μ_n (cm^2/V s)	100	340	170
Hole mobility : μ_p (cm^2/V s)	100	50	170
Conduction band effective density of states : N_C (cm^{-3})	2.2×10^{18}	2.4×10^{18}	2.8×10^{19}
Valence band effective density of states : N_V (cm^{-3})	1.8×10^{19}	2.57×10^{19}	1.04×10^{19}

Table II.IV. Parameters of defect levels utilized in the simulation [23, 28-30]

Gaussian defect states	ZnO, ,	CdS	MoO_3
Gaussian defect density (cm^{-3})	N_{GD} : 1.5×10^{18}	N_{GD} : 1.5×10^{18}	N_{GD} : 1.5×10^{18}
Peak energy position (eV)	E_{GD} : 3.1	E_{GD} : 2.2	E_{GD} : 2.7
Decay energy (eV)	W_{GD} : 0.1	W_{GD} : 0.1	W_{GD} : 0.1
σ_n (cm^2)	1.0×10^{-14}	1.0×10^{-14}	1.0×10^{-14}
σ_p (cm^2)	1.0×10^{-16}	1.0×10^{-16}	1.0×10^{-16}

Table II.V. Material parameters utilized in the simulation [23, 31-34]

Layer properties	Cu_2O
Band gap : E_g (eV)	2.1
Electron affinity : χ_e (eV)	3.3
Relative permittivity : ε_r ($F\ cm^{-1}$)	12
Electron mobility : μ_n ($cm^2/V\ s$)	40
Hole mobility : μ_p ($cm^2/V\ s$)	40
Conduction band effective density of states : N_C (cm^{-3})	2.2×10^{18}
Valence band effective density of states : N_V (cm^{-3})	1.8×10^{19}

Table II.VI. Parameters of defect levels utilized in the simulation [23, 35]

Gaussian defect states	Cu_2O
Gaussian defect density (cm^{-3})	N_{GA} : 5.0×10^{17}
Peak energy position (eV)	E_{GA} : 1.65
Decay energy (eV)	W_{GA} : 0.1
σ_n (cm^2)	1.0×10^{-16}
σ_p (cm^2)	1.0×10^{-14}

2.4 Modeling the ITO/ZnO/CdS/FeS_2/MoO_3/Al Device to Examine the Validity of the Simualtion

Firstly, the ITO/ZnO/CdS/FeS_2/MoO_3/Al device was modeled to determine whether these parameters were suitable. In addition, the previously reported results in simulation model was demonstrated to examine why this device did not obtain satisfactory conversion efficiency.

Figure 2.1 shows the device structure and the corresponding film thickness and the doping concentrations in this simulation model. Since the doping concentrations of FeS_2 thin film were higher (10^{18} – 10^{20} cm^{-3}) than whose of FeS_2 bulk crystal (10^{15} – 10^{16} cm^{-3}), this model utilized the doping concentrations of FeS_2 thin film to compare the calculation result with previous dark current-voltage (*I*–*V*) characteristic data [6, 36].

MoO_3 thin film can also act as an effective hole-transporting or electron-blocking layer to reduce the recombination of electrons and holes [37]. Figure 2.2 shows the band structure of the semiconductor layer. It suggests high potential barriers were formed at the CdS/FeS_2 interface and the FeS_2/MoO_3 interface. The potential barrier height at both the CdS/FeS_2 interface and the FeS_2/MoO_3 interface were about 0.9 eV. Since FeS_2 was reported as an *n*-type semiconductor, CdS/FeS_2 did not form a *p*-*n* junction. Figure 2.2 also shows that the Fermi level of FeS_2 was located at a position above the conduction band minimum (CBM). Electrons in the CdS layer moved to the FeS_2 layer by band bending at the FeS_2/MoO_3 interface, which made the position of the Fermi level higher than the CBM.

The electrical characteristics was calculated by applying a voltage from -1 to 2 V under a dark condition using the modeled ITO/ZnO/CdS/FeS_2/MoO_3/Al structure, as shown in Fig. 2.3. The calculated and reported *I*–*V* characteristics are similar [18], especially below the onset voltage, indicating that this simulation modeling reasonably demonstrates the electrical performance. Although the *I*–*V* curves show a large difference above 1.5 V, the difference may

be caused by the difference in the series resistances of the actual and simulated cells.

The onset voltage of each *I–V* characteristic was around 1.4 eV from Fig. 2.3. This result did not correspond well with the built-in potential formed at the *p*-*n* junction by ZnO/CdS/FeS_2 in this device because the band gap of FeS_2 was 0.8 eV, indicating that identifying the origin of this high onset voltage is necessary. By performed a simulation under an illumination condition, it is found that there is no photovoltage generation, which is consistent with the reported results [18]. This suggests the parameters utilized for the device simulation are suitable for modeling the previously reported FeS_2 thin film photovoltaic devices.

Here, the band structure after voltage application was investigated to consider the origin of the high onset voltage. Figure 2.4(a) and 2.4(b) show the changes in the band structures at the front and rear sides, respectively. The CBM and the valence band maximum (VBM) in CdS, FeS_2, and MoO_3 decrease with increasing applied voltage, while the CBM and VBM in ZnO were constant. In particular, the potential barrier at the FeS_2/MoO_3 interface in the region of 740–750 nm from the ITO markedly decreased with applied voltage, suggesting that the origin of high onset voltage is related to the potential barrier at the FeS_2/MoO_3 interface. It was confirmed that the depletion layer was not formed at the ZnO/CdS/FeS_2 layer, so it was difficult to obtain photovoltaic characteristics because of the inversion layer on the iron pyrite surface.

Front contact ITO	200 nm	
Window layer n-ZnO	200 nm	$1\times10^{16}cm^{-3}$
Buffer layer n-CdS	50 nm	$1\times10^{16}cm^{-3}$
Surface layer FeS_2	4 nm	$1\times10^{19}cm^{-3}$
Bulk layer n-FeS_2	492 nm	$1\times10^{19}cm^{-3}$
Surface layer FeS_2	4 nm	$1\times10^{19}cm^{-3}$
Transport layer p-MoO_3	15 nm	$1\times10^{16}cm^{-3}$
Back contact Al	200 nm	

Fig. 2.1 Device structure of ITO/ZnO/CdS/FeS_2/MoO_3/Al. The surface layer of FeS_2 is set on both sides of the bulk layer of FeS_2 to model the inversion layer.

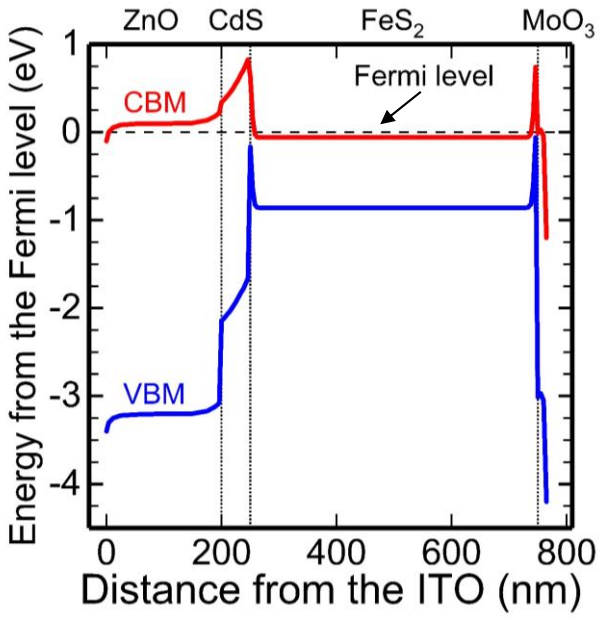

Fig. 2.2 Band structure of ZnO/CdS/FeS_2/MoO_3 layer at thermal equilibrium with the inversion layer of FeS_2.

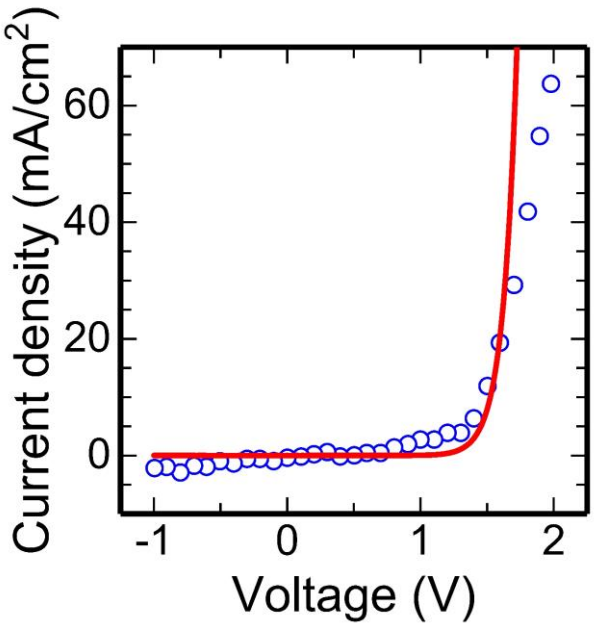

Fig. 2.3 *I–V* characteristics of the ITO/ZnO/CdS/FeS_2/MoO_3/Al device under the dark condition.

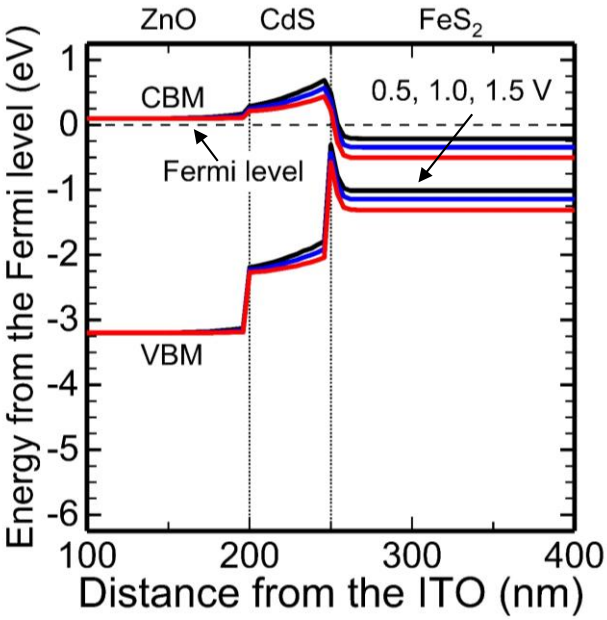

Fig. 2.4(a) Change in band structure after applying voltage of 0.5, 1.0, and 1.5 V. This figure shows the ZnO/CdS/FeS_2 region.

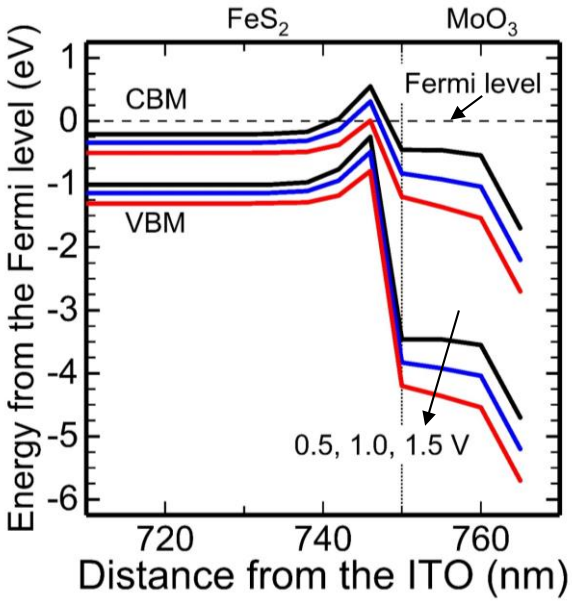

Fig. 2.4(b) Change in band structure after applying voltage of 0.5, 1.0, and 1.5 V. This figure shows the FeS_2/MoO_3 region.

2.5 Modeling the ITO/Cu_2O/FeS_2/Al Device to Examine the Effect of Inversion Layer at Iron Pyrite Surface for Photovoltaic Characteristics

From section 2.4, device modeling indicated that *n*-CdS/*p*-FeS_2 hetero-junction of ITO/ZnO/CdS/FeS_2/MoO_3/Al device reported in previous study was not formed and *n*-FeS_2 might be regarded as *p*-type semiconductor due to inversion layer at iron pyrite surface. Therefore, fabrication of *p*-window layer/*n*-FeS_2 hetero-junction is desirable toward high performance FeS_2 photovoltaic device. Here, Cu_2O was utilized as a *p*-type window layer to model *p*-Cu_2O/*n*-FeS_2 hetero-junction photovoltaic device. In this section, ITO/Cu_2O/FeS_2/Al device including the inversion layer of FeS_2 was modeled by utilizing both parameters of FeS_2 bulk layer and surface layer like section 2.4. In addition, an ITO/Cu_2O/FeS_2/Al device without the FeS_2 inversion layer was modeled to study the improvement in photovoltaic characteristics achieved by removing the inversion layer. It is expected that the modification of the potential barrier formed at the interface of Cu_2O/FeS_2 by removing the inversion layer.

Figure 2.5(a) shows the device structure that includes the inversion layer of FeS_2, and Fig. 2.6(a) shows the band structure of the *p*-Cu_2O/*n*-FeS_2 region at thermal equilibrium calculated using the parameters shown in Tables of section 2.3. Figure 2.7(a) shows an enlargement of the graph around the interface of *p*-Cu_2O/*n*-FeS_2. On the other hand, Fig. 2.5(b) shows the device structure of Cu_2O/FeS_2 without the inversion layer and Fig. 2.6(b) shows its band structure at thermal equilibrium. The FeS_2 device film thickness is set so that it will be the same as the FeS_2 thickness with an inversion layer, as shown in Fig. 2.5(a). Figure 2.7(b) shows an enlargement of the graph at the interface of Cu_2O/FeS_2.

In Figs. 2.6(a) and 2.7(a), a notch at the VBM was observed, formed owing to the FeS_2 inversion layer. This notch was formed as a result of the difference in ionization potentials

between Cu_2O and the hole-rich layer of FeS_2. The ionization potentials of FeS_2 and Cu_2O are 5.25 and 5.4 eV, respectively, which is a difference (ΔE_V) of 0.15 eV. While a high potential barrier was not found at the interface of the Cu_2O/FeS_2 region, as shown in Figs. 2.6(b) and 2.7(b), a slight spike remained on the VBM at the interface of the Cu_2O/FeS_2 region. Next, the current density was calculated by applying a voltage from -1 to 1 V under dark and illumination conditions and obtained the photovoltaic characteristics.

The obtained result are shown in Figs. 2.8 and 2.9. In Figs. 2.8(a) and (b), *I–V* characteristics under both dark and illumination condition show overlap because the current density sharply increases by applying a positive voltage. On the other hand, Fig. 2.9 shows the enlargement figure of Fig. 2.8. In Fig. 2.9(a), the *I–V* curve under the illumination condition was shifted downward from that under the dark condition, indicating that this device structure shows a photovoltaic effect, although the conversion efficiency was 0.8%, which is very low. The conversion efficiency of the ITO/Cu_2O/FeS_2/Al device that included an inversion layer of FeS_2 was 0.8%. However, it was founded that the device structure of *p*-Cu_2O/*n*-FeS_2 hetero-junction showed a photovoltaic effect. Similarly, the *I–V* characteristic was calculated by applying a voltage from -1 to 1 V under both dark and illumination conditions for the device without the inversion layer, as shown in Fig. 2.9(b). The *I–V* characteristics under the illumination condition produced higher photovoltage. Owing to the removal of the inversion layer, the conversion efficiency was improved from 0.8 to 1.2%, V_{OC} increased from 0.09 to 0.26 V, and J_{SC} decreased from 19.49 to 7.51 mA/cm^2.

The cause of the decrease in J_{SC} is assumed to be the recombination of photogenerated carriers owing to the spike in the VBM at the interface of Cu_2O/FeS_2. The calculated recombination rate of the device with the inversion layer was 8×10^{21} cm^{-3}s^{-1} at the interface of Cu_2O/FeS_2 whereas the rate of the device without the inversion layer was 1.2×10^{23} cm^{-3}s^{-1}, suggesting that the spike in the VBM at the interface of Cu_2O/FeS_2 markedly decreased J_{SC} by

increasing carrier recombination owing to the prevention of hole transport. On the other hand, V_{OC} was increased by removing the inversion layer. The shunt resistance of the Cu_2O/FeS_2 photovoltaic device with the inversion layer was 148 Ωcm^2, and that of the Cu_2O/FeS_2 photovoltaic device without an inversion layer was 763 Ωcm^2. Therefore, the shunt resistance was increased by removing the inversion layer, suggesting that the leakage current was prevented and charge separation was promoted.

Front contact ITO	100 nm	
Window layer p-Cu_2O	100 nm	$1\times10^{16}cm^{-3}$
Surface layer FeS_2	4 nm	$1\times10^{19}cm^{-3}$
Bulk layer n-FeS_2	492 nm	$5\times10^{15}cm^{-3}$
Surface layer FeS_2	4 nm	$1\times10^{19}cm^{-3}$
Back contact Al	200 nm	

Fig. 2.5(a) Device structure of ITO/Cu_2O/FeS_2/Al. Surface layers of FeS_2 are set on both sides of the bulk layer of FeS_2 to model the inversion layer.

Front contact ITO	100 nm	
Window layer p-Cu_2O	100 nm	$1\times10^{16}cm^{-3}$
Bulk layer n-FeS_2	500 nm	$5\times10^{15}cm^{-3}$
Back contact Al	200 nm	

Fig. 2.5(b) Device structure of ITO/Cu_2O/FeS_2/Al without inversion layers.

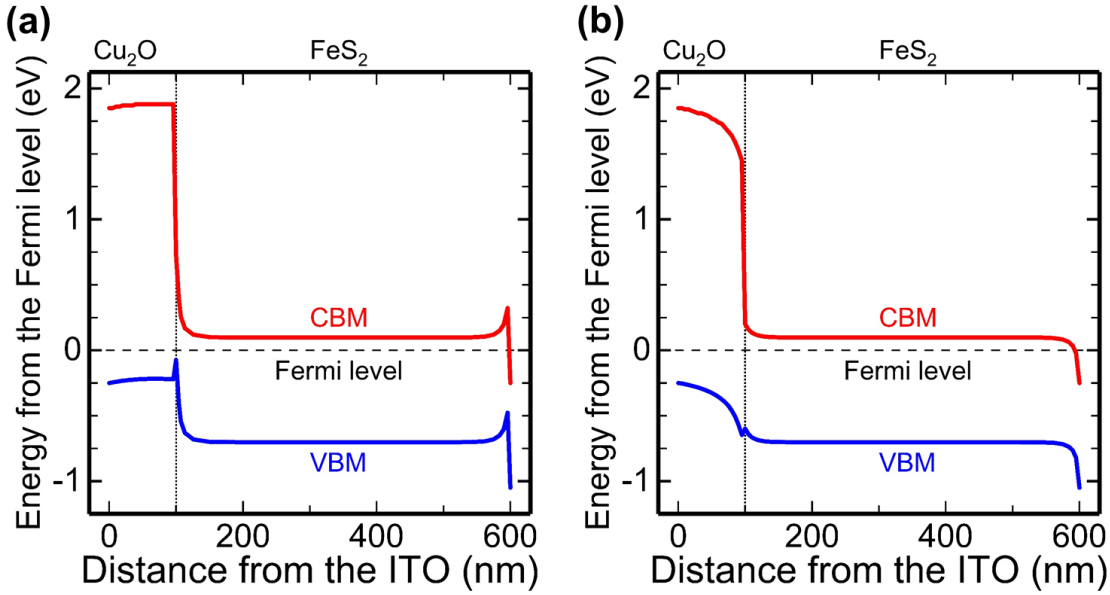

Fig. 2.6(a) Band structure of the Cu_2O/FeS_2 layer at thermal equilibrium with the inversion layer of FeS_2 and **(b)** without the inversion layer of FeS_2.

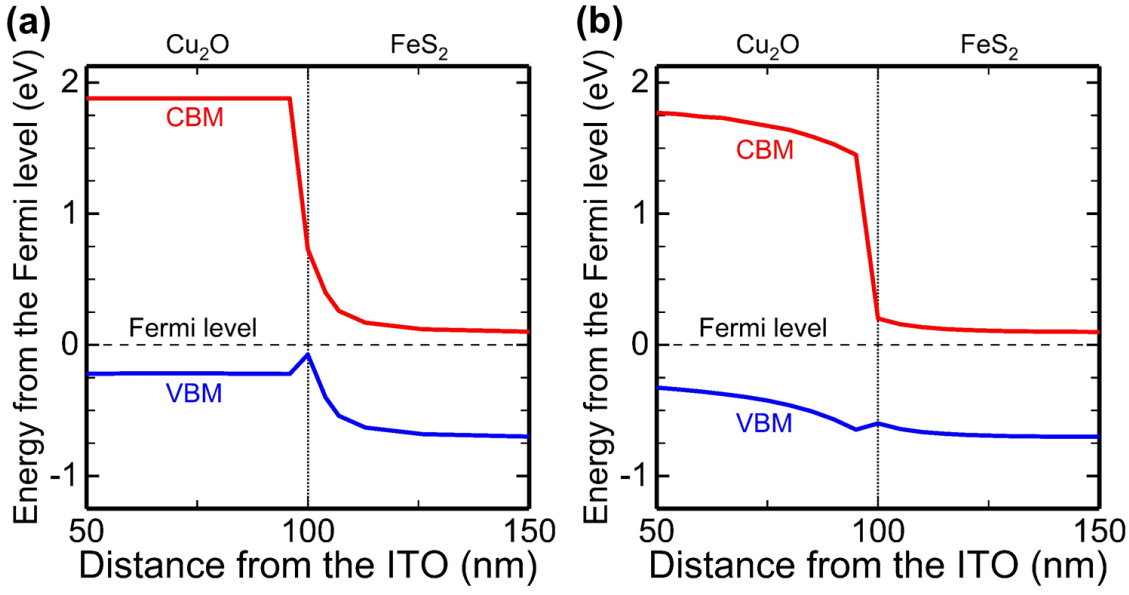

Fig. 2.7(a) Band structure of the Cu_2O/FeS_2 layer between 50 and 150 nm with the inversion layer of FeS_2 and **(b)** without the inversion layer of FeS_2.

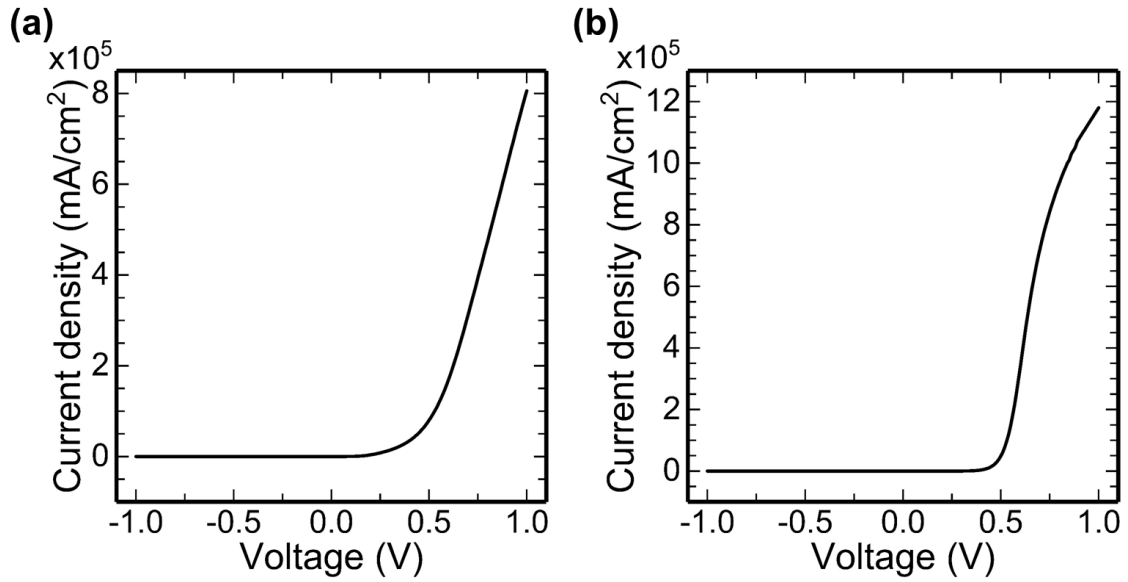

Fig. 2.8(a) *I–V* characteristics of ITO/Cu_2O/FeS_2/Al device by applying a voltage from -1 to 1 V under both dark and illumination condition. This device includes the inversion layer of FeS_2. **(b)** This device does not include the inversion layer of FeS_2. In both figures, *I–V* characteristics under both dark and illumination condition show overlap because the current density sharply increases by applying a positive voltage.

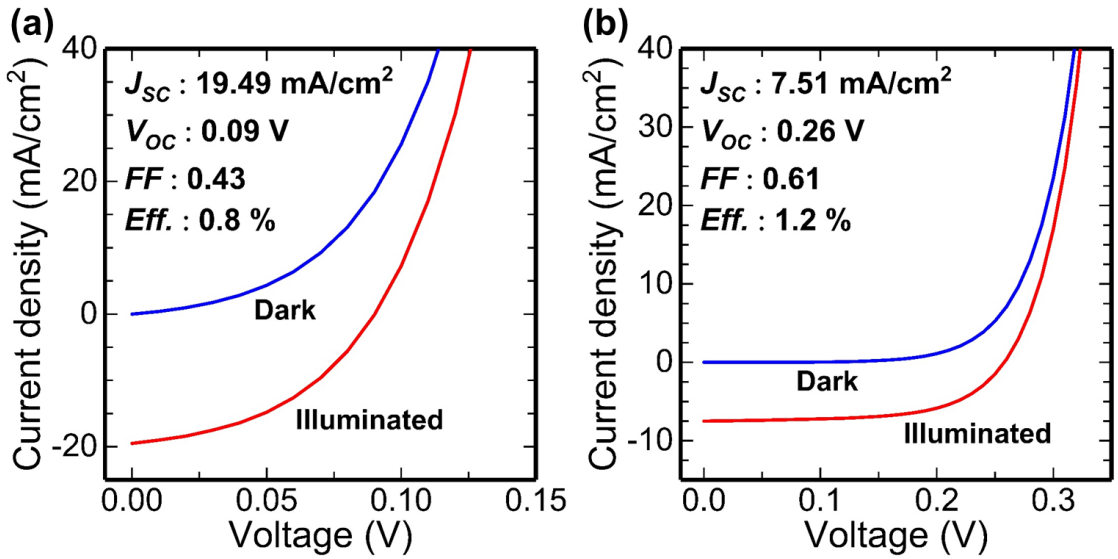

Fig. 2.9(a) The enlargement figure of Fig. 2.8(a). This device includes the inversion layer of FeS_2. **(b)** The enlargement figure of Fig. 2.8(b). This device does not include the inversion layer of FeS_2.

2.6 Influence by Changing Parameters

Removing the inversion layer had little effect on improving conversion efficiency. It is essential to consider other factors such as the effect of a high deep donor level in the bulk on the photovoltaic device performance. In this section, the results of changing the defect level density in the bulk layer from 1×10^{13} to 1×10^{19} cm^{-3} are presented.

Figure 2.10(a) shows the obtained photovoltaic device characteristics. J_{SC} of about 30 mA/cm^2 was achieved when the density of states was decreased to less than 1×10^{17} cm^{-3}. On the other hand, V_{OC} remained at around 0.3 V until the defect density was decreased to 1×10^{15} cm^{-3}, and V_{OC} reached 0.54 V when the defect density was less than 1×10^{14} cm^{-3}. In addition, *FF* was enhanced when the defect level density in the bulk layer was 1×10^{19} cm^{-3}. The enhancement of *FF* is related to increasing V_{OC}, and V_{OC} was increased by increasing the built-in potential through increasing the defect density in the bulk layer. Figure 2.10(b) shows the change in the band structure caused by changing the deep donor level defect density of states. The change in the *I–V* characteristics under the dark condition in the bulk layer shows that the onset voltage increased from 0.3 to 0.4 V on increasing the defect density from 1×10^{17} to 1×10^{19} cm^{-3}.

When the defect density was reduced to less than 1×10^{15} cm^{-3}, the recombination rate was also reduced. As a result, the conversion efficiency increased greatly and saturated. Consequently, the conversion efficiency was about 13.4% when the defect density was decreased to around 1×10^{14} cm^{-3}. Although decreasing the recombination rate leads to an improvement in the conversion efficiency, carrier lifetime also affects cell performance. Thus, it is necessary to investigate the effect of carrier lifetime in the bulk layer.

Next, the carrier lifetimes of electrons and holes were changed from 100 ps to 100 μs, and photovoltaic characteristics were calculated to investigate the influence the effect of carrier

lifetime on photovoltaic performance. The density of states of the deep donor level was set at 1×10^{15} and 1×10^{18} cm^{-3}. Figure 2.11(a) shows the calculated results of the Cu_2O/FeS_2 hetero-junction photovoltaic device including the inversion layer of FeS_2. In this model, only the carrier lifetime in the FeS_2 bulk layer was changed while the carrier lifetime in the surface layer was not changed in order to check the effect of carrier lifetime on the cell with the inversion layer. The device structure was the same as in Fig. 2.5(a). Figure 2.11(b) shows the results of the Cu_2O/FeS_2 hetero-junction photovoltaic device without the inversion layer of FeS_2, where the device structure was the same as in Fig. 2.5(b). In Fig. 2.11(a), J_{SC} was about 27 mA/cm^2 and V_{OC} was 0.35 V; consequently, the conversion efficiency reached 7% when the donor level density was 1×10^{15} cm^{-3} and the carrier lifetime was longer than 100 ns. However, conversion efficiency was saturated when the carrier lifetime increased to more than 100 ns because V_{OC} was saturated at 0.35 V.

Figure 2.11(b) shows that the conversion efficiency, J_{SC}, V_{OC}, and FF reached 13.4%, 30.94 mA/cm^2, 0.54 V, and 0.8, respectively, when the donor level density was 1×10^{15} cm^{-3} and the carrier lifetime was 100 μs. Conversion efficiency exceeded 10% when the carrier lifetime was more than 100 ns. The results shown in Figs. 2.11(a) and 2.11(b) suggest that the inversion layer tends to prevent charge separation at the interface of Cu_2O/FeS_2, although the recombination rate decreases in the FeS_2 bulk layer. In addition, the variation in J_{SC} with increasing lifetime is different with the presence of the inversion layer.

When the donor defect density was 1×10^{18} cm^{-3} and the inversion layer was not included, J_{SC} was enhanced with increasing carrier lifetime. Since the Cu_2O/FeS_2 photovoltaic device without the inversion layer had a spike in the VBM, the hole recombination at the interface of Cu_2O/FeS_2 was affected when the carrier lifetime was short and donor defect density was high. On the other hand, the Cu_2O/FeS_2 photovoltaic device with the inversion layer was not affected by hole recombination at the spike. As a result, these calculations suggest that it is necessary to

improve not only the defect density in the FeS_2 bulk layer but also that in the surface layer because the inversion layer prevents charge separation at the interface of the hetero-junction.

Recently, it was reported that a polysulfide layer was formed on the surface of FeS_2 crystal during the formation of FeS_2 crystal and affected its electrical properties [20, 38], indicating that a technique for removing the polysulfide layer also can open the door to the development of high-efficiency FeS_2 photovoltaic devices. The ideal limit of conversion efficiency predicted by the Shockley-Queisser limit is about 16% since the band gap of FeS_2 is 0.8 eV in this study [39]. In this device simulation, optimization of the thickness of each film, such as the transparent conductive film or a window layer that can decrease the reflectance of light at the surface, was not considered, so the conversion efficiency was lower than the ideal limit of conversion efficiency. It is assumed that by decreasing the density of states to about 1×10^{15} cm^{-3} and increasing the lifetime to over 100 ns, it is possible to reach the ideal limit of conversion efficiency, which would indicate that this simulation has produced qualitative guidelines for the development of FeS_2 photovoltaic devices. The deep donor level defects in the bulk are caused by the intrinsic sulfur vacancies [36]. To avoid a high deep donor density, sulfur annealing and synthesis of iron chalcogenide may be effective [14].

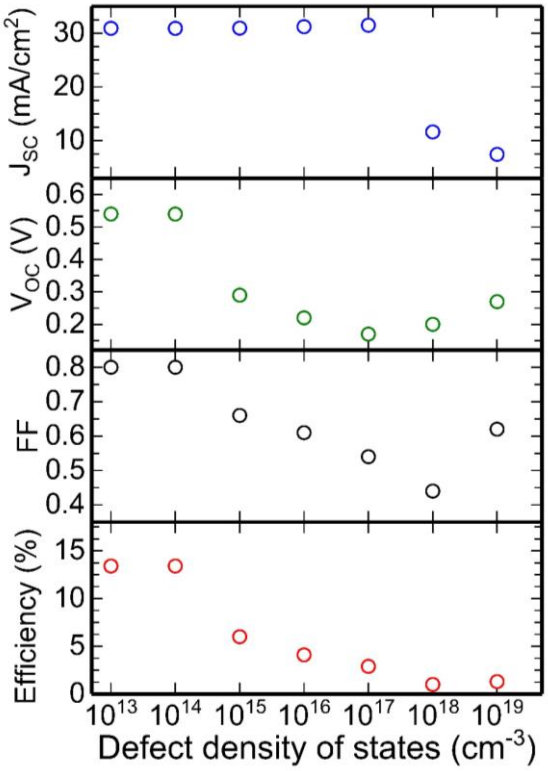

Fig. 2.10(a) Change in the solar cell properties on changing the defect density of states of the deep donor level. This device does not include the inversion layer of FeS_2.

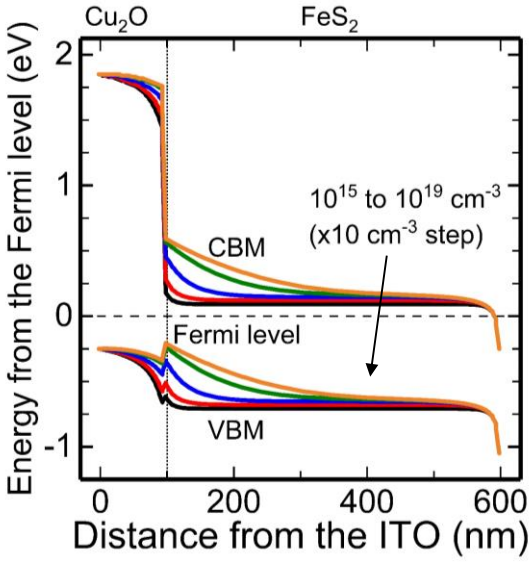

Fig. 2.10(b) Change in band structure on changing the defect density of states of the deep donor level. The band structure of the Cu_2O/FeS_2 layer at thermal equilibrium does not include the inversion layer of FeS_2.

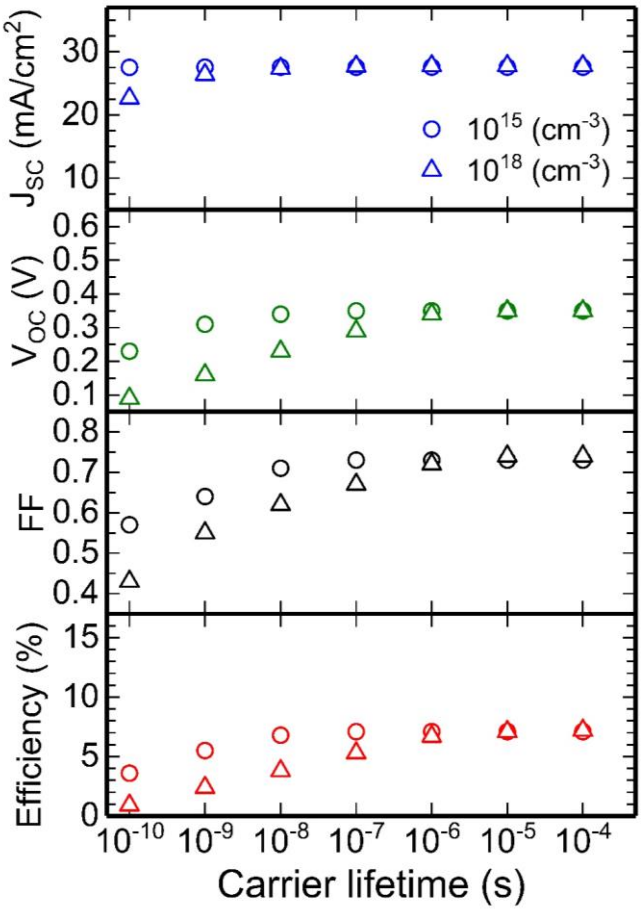

Fig. 2.11(a) Photovoltaic characteristic dependence on the carrier lifetime in bulk FeS_2 layer with the inversion layer of FeS_2.

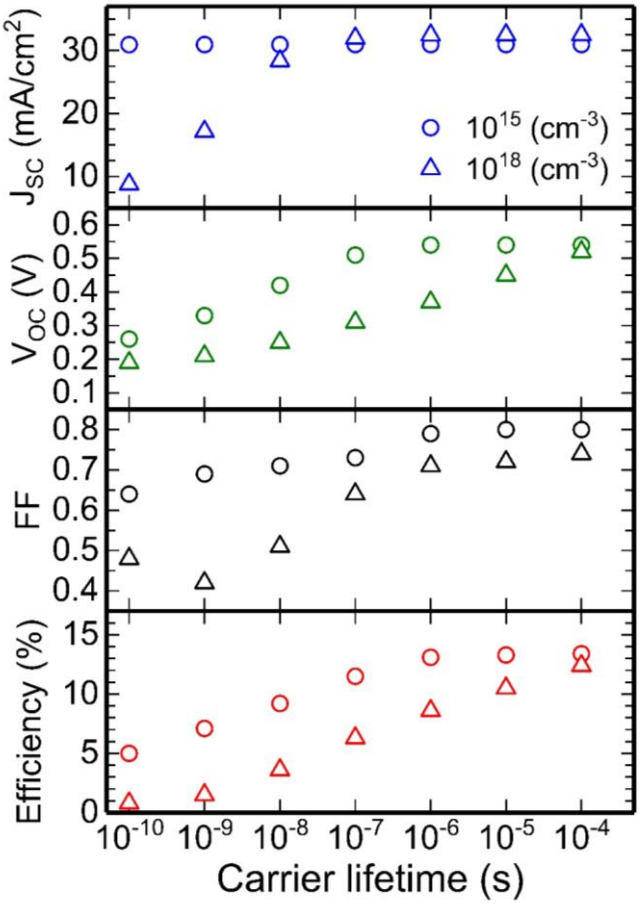

Fig. 2.11(b) Photovoltaic characteristic dependence on the carrier lifetime in bulk FeS_2 layer without the inversion layer of FeS_2.

2.7 Summary

Through combing the density of states in the surface and bulk layers of iron pyrite (FeS_2), the photovoltaic characteristics of FeS_2 photovoltaic devices toward higher efficiency were calculated by 2D device simulation. It was founded that the following factors allow an FeS_2 photovoltaic device efficiency as high as around 13.5% to be achieved: a *p*-Cu_2O/*n*-FeS_2 hetero-junction, a density of states in the bulk layer of less than 1×10^{15} cm^{-3}, and carrier lifetime in the bulk of longer than 1 μs. To realize higher efficiency FeS_2 photovoltaic device, it is necessary to remove the surface layer and reduce the density of states of the deep donor level during the fabrication of the FeS_2 bulk layer.

Reference

[1] A. Ennaoui, S. Fiechter, H. Goslowsky, H. Tributsch, J. Electrochem. Soc. 132 (1985) 1579-1582.

[2] A. Ennaoui, S. Fiechter, N. Pettenkofer, N. Alonso-Vante, K. Büker, M. Bronold, C. Höpfner, H. Tributsch, Sol. Energy Mater. Sol. Cells 29 (1993) 289-427.

[3] A. Ennaoui, H. Tributsch, Sol. Energ. Mater. 14 (1986) 461-474.

[4] C. Höpfner, K. Ellmer, A. Ennaoui, C. Pettenkofer, S. Fiechter, H. Tributsch, J. Cryst. Growth 151 (1995) 325-334.

[5] B. Thomas, T. Cibik, C. Höpfner, K. Diesner, G. Ehlers, S. Fiechter, K. Ellmer, J. Mater. Sci.: Mater. Electron. 9 (1998) 61-64.

[6] N. Berry, M. Cheng, C. L. Perkins, M. Limpinsel, J. C. Hemminger, M. Law, Adv. Energ. Mater. 2 (2012) 1124-1135.

[7] S. Bausch, B. Sailer, H. Keppner, G. Willeke, E. Bucher, G. Frommeyer, Appl. Phys. Lett. 57 (1990) 25-27.

[8] G. Smestad, A. Ennaoui, S. Fiechter, H. Tributsch, W. K. Hofmann, M. Birkholz, W. Kautek, Sol. Energ. Mater. 20 (1990) 149-165.

[9] J. R. Ares, M. Leon, N. M. Arozamena, J. Sanchez-Paramo, P. Celis, I. J. Ferrer, C. Sanchez, J. Phys.: Condens. Matter 10 (1998) 4281-4289.

[10] J. R. Ares, I. J. Ferrer, F. Cuevas, C. R. S´anchez, Thin Solid Films 387 (2001) 97-99.

[11] J. R. Ares, I. J. Ferrer, C. R. Sánchez, Thin Solid Films 431-432 (2003) 511-513.

[12] R. J. Soukup, P. Prabukanthan, N. J. Ianno, A. Sarkar, C. A. Kamler, D. G. Sekora, J. Vac. Sci. Technol. A 29 (2011) 011001.

[13] M. Caban-Acevedo, M. S. Faber, Y. Tan, R. J. Hamers, S. Jin, Nano Lett. 12 (2012) 1977-1982.

[14] L. Yu, S. Lany, R. Kykyneshi, V. Jieratum, R. Ravichandran, B. Pelatt, E. Altschul, H. A.

S. Platt, J. F. Wager, D. A. Keszler, A. Zunger, Adv. Energ. Mater. 1 (2011) 748-753.

[15] Y. Mikhlin, Y. Tomashevich, S. Vorobyev, S. Saikova, A. Romanchenko, R. Felix, Appl. Surf. Sci. 387 (2016) 796-804.

[16] S. Shukla, G. Xing, H. Ge, R. R. Prabhakar, S. Mathew, Z. Su, V. Nalla, T. Venkatesan, N. Mathews, T. Sritharan, T. C. Sum, Q. Xiong, ACS Nano 10 (2016) 4431-4440.

[17] C. Steinhagen, T. B. Harvey, C. J. Stolle, J. Harris, B. A. Korgel, J. phys. chem. lett. 3 (2012) 2352-2356.

[18] D. G. Moon, A. Cho, J. H. Park, S. Ahn, H. Kwon, Y. S. Cho, S. Ahn, J. Mater. Chem. A 2 (2014) 17779-17786.

[19] J. Hu, Y. Zhang, M. Law, R. Wu, J. Am. Chem. Soc. 134 (2012) 13216-13219.

[20] M. Limpinsel, N. Farhi, N. Berry, J. Lindemuth, C.L. Perkins, Q. Lin, M. Law, Energy Environ. Sci. 7 (2014) 1974-1989.

[21] T. A. Bither, R. J. Bouchard, W. H. Cloud, P. C. Donohue, W. J. Siemons, lnorg. Chem. 7 (1968) 2208-2220.

[22] A. Janotti, C. G. Van de Walle, Rep. Prog. Phys. 72 (2009) 126501.

[23] Atlas User's Manual, Device Simulation Software, Silvaco International, S. Clara, CA.

[24] T. Matsushima, Y. Kinoshita, H. Murata, Appl. Phys. Lett. 91 (2007) 253504.

[25] C. Tao, S. Ruan, X. Zhang, G. Xie, L. Shen, X. Kong, W. Dong, C. Liu, W. Chen, Appl. Phys. Lett. 93 (2008) 193307.

[26] D. Y. Kim, J. Subbiah, G. Sarasqueta, F. So, H. Ding, Irfan, Y. Gao, Appl. Phys. Lett. 95 (2009) 093304.

[27] M. Kröger, S. Hamwi, J. Meyer, T. Riedl, W. Kowalsky, A. Kahn, Appl. Phys. Lett. 95 (2009) 123301.

[28] W.-I. Lee, R.-L. Young, W.-K. Chen, Jpn. J. Appl. Phys. 35 (1996) L1158-L1160.

[29] H. Ashour, F. El Akkad, Phys. Status Solidi A 184 (2001) 175-178.

[30] Y. Guo, J. Robertson, Appl. Phys. Lett. 105 (2014) 222110.

[31] A. F. Wright, J. S. Nelson, J. Appl. Phys. 92 (2002) 5849-5851.

[32] J. W. Hodby, T. E . Jenkins, C. Schwab, H. Tamura, D. Trivich, J. Phys. C Solid State Phys. 9 (1976) 1429-1439.

[33] S. Hussain, C. Cao, W. S. Khan, G. Nabi, Z. Usman, A. Majid, T. Alharbi, Z. Ali, F. K. Butt, M. Tahir, M. Tanveer, F. Idress, Mater. Sci. Semicond. Process. 25 (2014) 181-185.

[34] S. H. Wee, P. S. Huang, J. K. Lee, A. Goyal, Sci. Rep. 5 (2015) 16272.

[35] H. A. Al-Jawhari, Mater. Sci. Semicond. Process. 40 (2015) 241-252.

[36] M. Caban-Acevedo, N. S. Kaiser, C. R. English, D. Liang, B. J. Thompson, H. E. Chen, K. J. Czech, J. C. Wright, R. J. Hamers, S. Jin, J. Am. Chem. Soc. 136 (2014) 17163-17179.

[37] D. Y. Wang, Y. T. Jiang, C. C. Lin, S. S. Li, Y. T. Wang, C. C. Chen, C. W. Chen, Adv. Mater. 24 (2012) 3415-3420.

[38] D. Liang, M. Caban-Acevedo, N. S. Kaiser, S. Jin, Nano Lett. 14 (2014) 6754-6760.

[39] W. Shockley, H. J. Queisser, J. Appl. Phys. 32 (1961) 510-519.

Chapter 3

Evaluation on Surface Condition of Iron Pyrite Single Crystal to Establish a Method of Oxidation Layer Removing at Iron Pyrite Surface

3.1 Introduction

In Chapter 2, two-dimensional device simulation, ATLAS (Silvaco), was utilized to demonstrate the effect of an inversion layer at the surface of iron pyrite for the photovoltaic characteristics of iron pyrite thin film photovoltaic devices. Numerical analysis suggested that the inversion layer formed at surface degraded the photovoltaic performance of iron pyrite thin film photovoltaic devices and it was essential to improve the inversion layer for enhancement of the performance of these devices.

Evidences about an origin of the inversion layer at surface of iron pyrite has not been reported yet. One of some hypothesis was suggested that the existence of intrinsic surface states which formed band bending and Fermi level pinning. This surface condition was modeled by ligand field theory (LFT) [1, 2]. The symmetry reduction of the Fe coordination sphere was broken at surface and forms the acceptor level which leaded to band bending and Fermi level pinning [1, 3, 4]. However, an absence of experimental evidence about acceptor level has not been confirmed.

Other hypothesis was suggested that existing of an oxidation layer such as iron hematite at the surface region forms band bending [5]. Figure 3.1 shows the potential difference between

iron pyrite and iron hematite. If oxide such as iron hematite is formed, the surface states in Fig. 3.2(a) appear. Fermi level of *n*-type iron pyrite was placed at mid gap, and Fermi level of hematite was placed at the top of its band gap in anticipation of *n*-type conduction in the oxide productions. As shown in Fig. 3.2(b), formation of the oxidation production created an empty band into which these electrons could be transferred, which resulted in forming band bending. This was related to Fermi level pinning by surface states and resulted from equilibration of bulk and surface Fermi level. In addition, the band bending might lead to the formation of the hole accumulation layer (inversion layer).

In this Chapter, iron pyrite single crystals were grown and the surface conditions of the crystals were evaluated to establish a method of removing oxidation layer at iron pyrite surface because the oxidation layer might encourage the formation of band bending as shown in Fig. 3.2(b). Band structure and electrical transport evaluations of iron pyrite after establishing a method of removing oxidation layer were described in Chapter 4. Iron pyrite single crystal instead of iron pyrite thin film was utilized for evaluation of the surface conditions because unstable phase purity and poor film quality in iron pyrite thin film might affect evaluation such as Hall effect measurement [6]. At first time, iron pyrite single crystals were grown by utilizing the flux method, and grown single crystals were sliced and polished to make wafers. These wafers are treated by alcohol solution and aqua regia solution. Aqua regia solution was utilized as a candidate of removing oxidation layer at the surface region. To evaluate surface conditions, Micro-Raman spectroscopy, X-ray photoelectron spectroscopy (XPS) and atomic force microscopy (AFM) were performed.

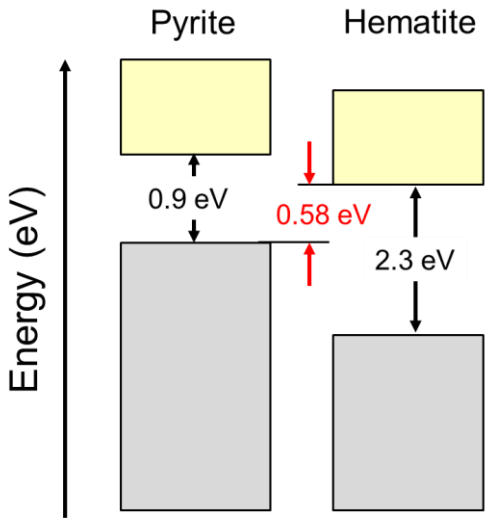

Fig. 3.1 Band edges of iron pyrite and iron hematite [4].

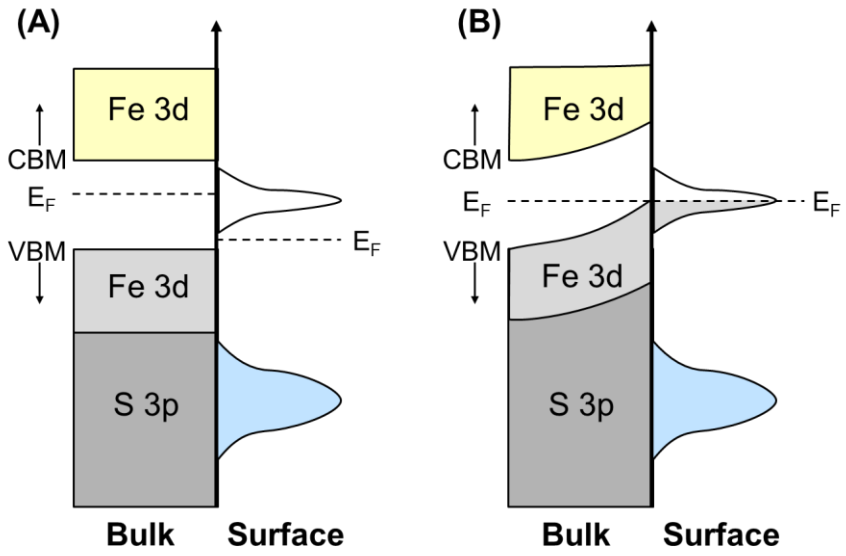

Fig. 3.2 (A) Band structure of the bulk and suraface of iron pyrite, given the formation of an oxide (hematite-like) surface state. **(B)** Band bending resulting from equilibration between the iron pyrite bulk and surface, including the hematite-like surface states [4].

3.2 Growth of Iron Pyrite Bulk Crystal

3.2.1 Flux method

The flux method is a technique for growing a high quality single crystal at a temperature much lower than the melting point of a material. Single crystals are regularly arranged three-dimensionally and are very important for basic research to evaluate the structure and physical properties of substances.

Crystal growth methods are classified into liquid phase method, gas phase method and solid phase method. The method utilizing the liquid phase is better to make large scale crystals because it is easy to restructure the constituent element. Methods of crystal growth using the liquid phase are divided into a melting process and a solution process. Melting processes such as Czochralski process and vertical Bridgeman method are crystal growth methods that utilizes same composition as that of the target. Melting processes is necessary to heat sample at a temperature above the melting point. Super-cooling in process is driving force of crystallization. An advantage of this process is that large crystals ban be grown in a short time.

On the other hand, the solution process corresponds to solution growth method, hydrothermal growth method and flux method. Supersaturation by slow cooling and evaporation of solvent in process is driving force of crystallization. In the solution growth method, crystal is grown by utilizing water as solvent at room temperature. In the hydrothermal growth method, crystal is grown by utilizing water which is heated over 100 °C. The solution growth method and the hydrothermal growth method is essential to solve the sample and grow crystal in water under certain conditions. In the flux method, inorganic materials and metals melting at high temperature region are utilized as solvent, and this solvent is called flux. In the crystal growth by the flux method, the liquidus line of the state diagram is utilized. Figure 3.3 shows the crystal-flux binary phase diagram. The flux (B) decrease the melting point of crystal (A) in the range from crystal (A) to eutectic composition (X_E). When the composition (X) is

heated to the temperature (T_1), X reaches to point (a) in liquid phase. After vaporing flux in the solution and reaching the point (b) by concentrating solute, growth of crystal is started. Growth of crystal continues with vaporing flux. As another process, the liquid phase at point (a) is cooled slowly and reached to the point (c) at the temperature (T_2), growth of crystal is started. Growth of crystal continues at the temperature (T_3) and this growth continues until the temperature (T_E). Therefore, since crystal (A) is formed at lower temperature than the melting point (T_A), flux method enables growth of various materials including high melting point and polymorphous transition.

The flux method has several advantages. For example, (i) the crystal is grown at much lower temperature than the melting point of the material, (ii) flat crystal reflecting the crystal structure is formed, (iii) an equipment for crystal growth is simple and operation is easy. On the other hand, disadvantages of the flux method are suggested that impurities are mixed into the grown crystal, size of grown crystal is small, and time for growth is long.

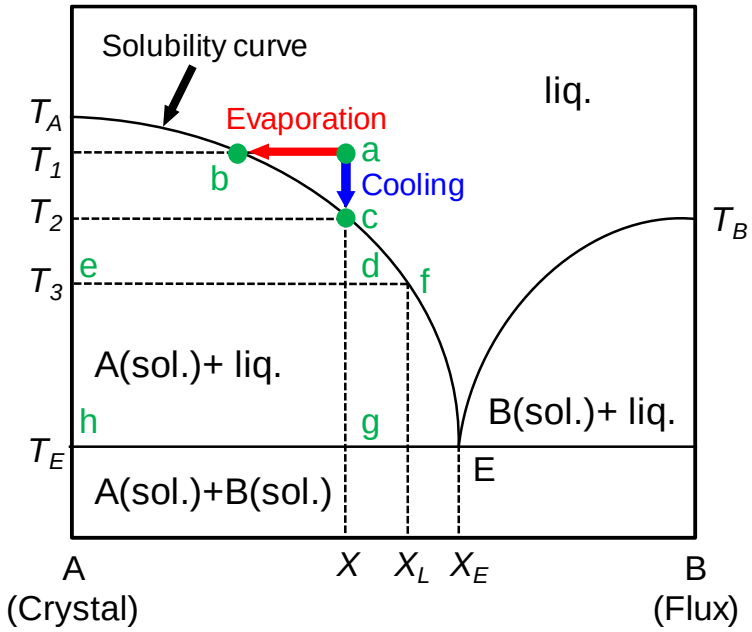

Fig. 3.3 Crystal-Flux binary phase diagram.

3.2.2 Experimental detail

Iron powder (99.9%, Kojundo Chemical Lab.) was loaded on a quartz boat and set in a quartz tube furnace, and the powder was heated in a flow a 5% H_2/ 95% Ar at 300 °C for 15 h to remove water and surface oxides. Sulfur powder (99%, FUJIFILM Wako Pure Chemical) was degassed and dried in a borosilicate glass flask under a vacuum at 130 °C for 3 h. $Na_2S{\cdot}9H_2O$ (99%, FUJIFILM Wako Pure Chemical) was dried and degassed in a teflon beaker at 320 °C for 5 h, resulting in a mixture of fine colorless and yellow powder which includes Na_2S and polysulfides. After the pre-treatment, these materials were loaded in alumina crucibles and sealed in evacuated quartz ampoules under a pressure of 4×10^{-3} Pa. 0.51 g of iron powder (9.13 mmol), 0.98 g of Na_2S (12.56 mmol) and 1.21 g of sulfur powder (37.71 mmol) were loaded in alumina crucibles. This rate was referred to two diagrams of the Na-S binary phase and Fe-S binary phase shown in Fig. 3.4(a) and (b) [6, 7]. As shown in Fig. 3.4 (a), mixtures of Na_2S and S have eutectics as low as 240°C, which suggest that Na-S liquid at low temperature prevents the burst of quartz ampoule due to an increase of sulfur vapor pressure. Next, the ampoule was placed in a muffle furnace and held vertically to entire time to avoid mixing or spilling the contents of the crucible. Figure 3.5 presents a typical procedure for crystal growth of iron pyrite used in this study. The ampoule was raised to 810 °C at a heating rate of 50 °C/h. When heating temperature reached to each 300 °C and 400 °C, the ampoule was held for 3 h at each temperature to avoid burst of quartz ampoule. After reaching to 810 °C, the ampoule was held for 6 h to react materials in alumina crucible. Next, the ampoule was cooled to 600 °C in 240 h, and finally cooled to room temperature in 24 h. The crucible was then removed from the ampoule and placed in beaker of Millipore water several hours to dissolve the flux. After removing crystal from the crucible, the crystal was rinsed with Millipore water and dried. Consequently, iron pyrite ingots with the diameter of about 7 mm were obtained as shown in Fig. 3.6(a). The ingots were then sliced utilizing SiC wheel saw and polished with a series of

emery papers (#100, #400, #800, #1200, #200, Maruto Instrument), and mirror-finished with a slurry containing diamond particles with an average particle size of 1.0 μm (Aqua diamond solution, Maruto Instrument) on a buff sheet (Hard type of polishing cloth, Maruto Instrument). Figure 3.6(b) shows the photograph of a wafer after polishing.

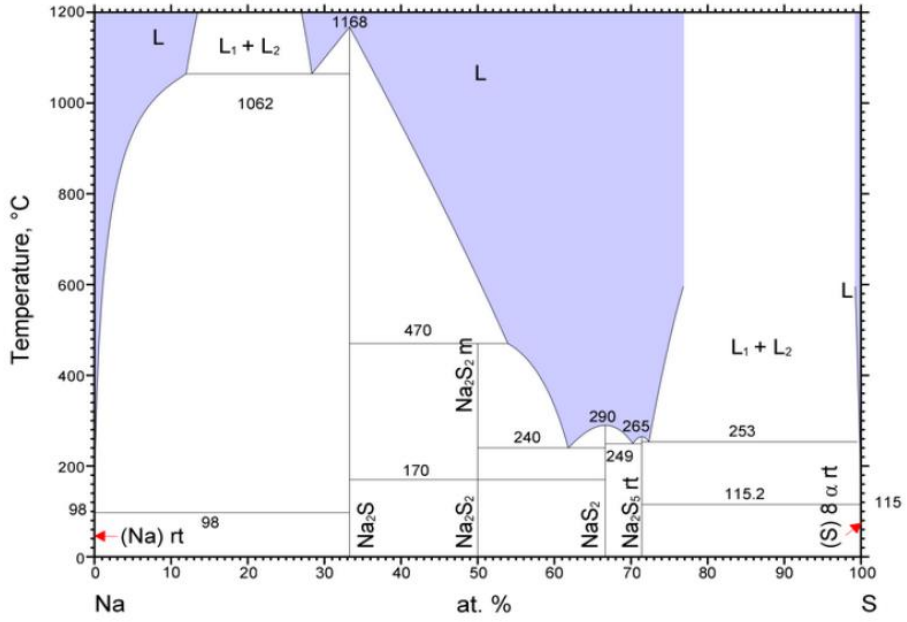

Fig. 3.4(a) The Na-S binary phase diagram [5].

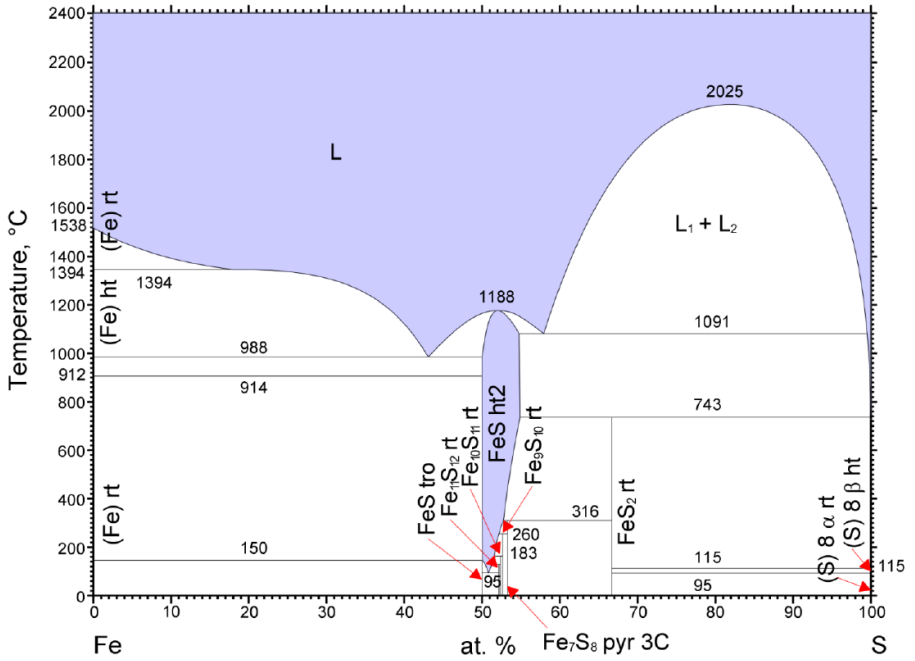

Fig. 3.4(b) The Fe-S binary phase diagram [6].

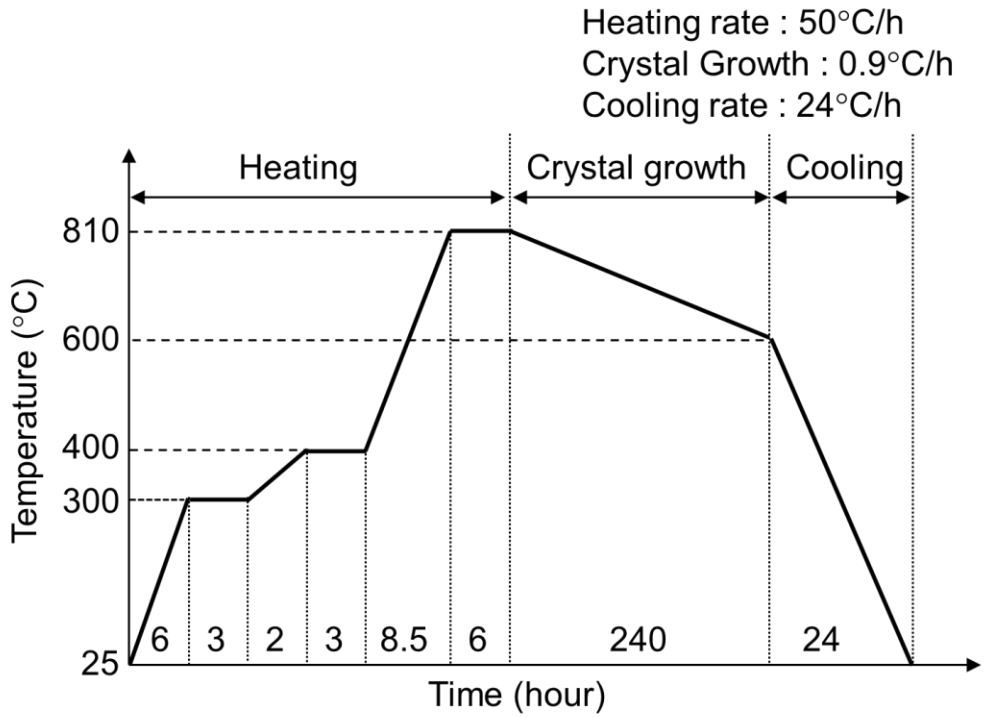

Fig. 3.5 Typical procedure for crystal growth of iron pyrite used in this study.

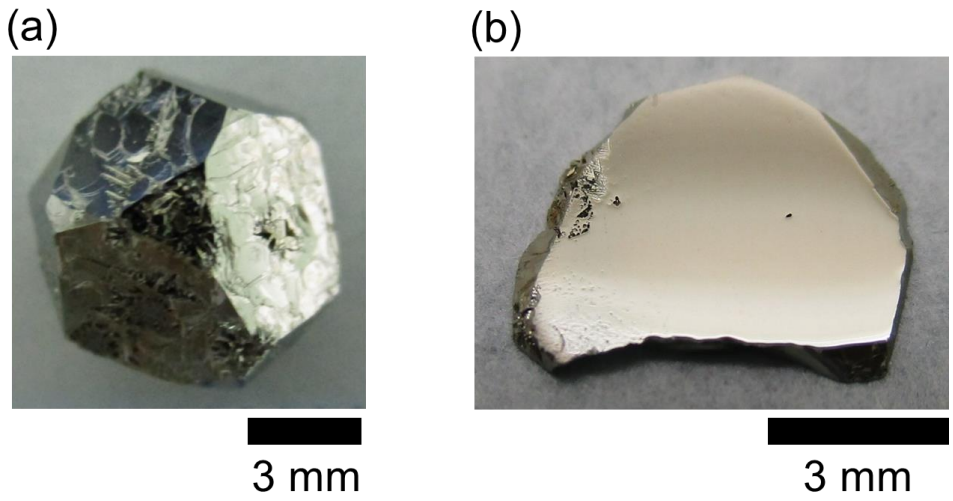

Fig. 3.6 Typical photographs of **(a)** grown crystal and **(b)** as-cut and polished wafer of grown crystal.

3.3 Characterization of crystal structure

The grown crystal was analyzed using X-ray diffraction (XRD) for phase identification. The XRD measurement was performed using Rigaku RINT-TTR III with Cu Kα radiation diffracted from a Graphite monochromator was used as an incident X-ray. The tube voltage and the tube current were 50kV and 300 mA, respectively.

Figure 3.7(a) shows the XRD profile of the powder of grown crystal. The strong peaks in the profile were assigned to the reference pattern of FeS_2 pyrite (ICDD#00-042-1340). On the other hand, Fig. 3.7(b) shows the XRD profile of crystal face of the grown crystal shown in Fig. 3.6(a). Two peaks were assigned to the reference pattern of FeS_2 pyrite (ICDD#00-042-1340). It is evident from Fig. 3.7(b) that grown crystal corresponds to iron pyrite single crystal. However, the XRD profiles of the wafers after slicing and polishing grown crystals are not detected because crystal face is not controlled in the experiment of crystal growth.

In addition, structure determination by micro crystal X-ray diffraction was performed on a Rigaku R-AXIS RAPID diffractometer using filtered Mo-Kα radiation at 103 K. Diffraction data was collected on a CCD area detector using Mo Kα radiation. A full sphere of data was collected for each crystal.

Figure 3.8 shows the view of the experimentally determined iron pyrite unit cell by micro crystal X-ray diffraction. Brown spheres are iron ions, and yellow spheres are sulfur ions. Table III.I shows crystal data of iron pyrite single crystal calculated by the micro crystal X-ray diffraction.

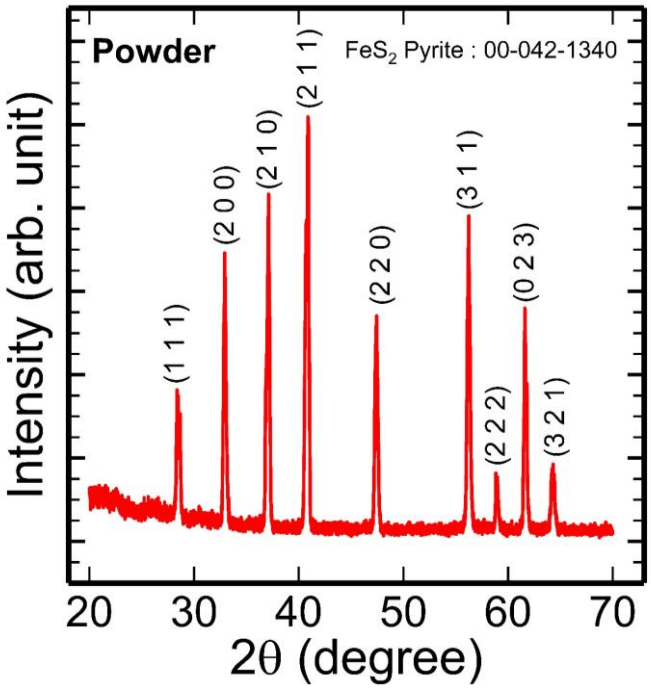

Fig. 3.7(a) XRD profile of powder made by crushing grown crystal.

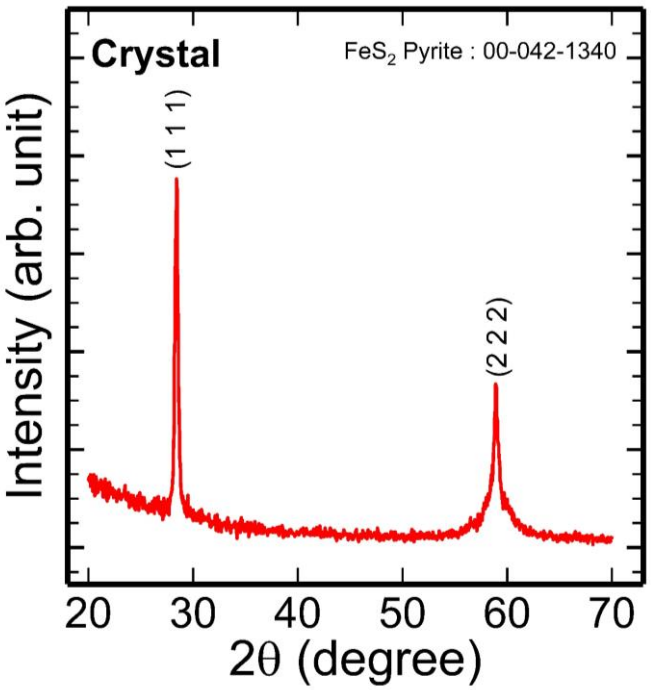

Fig. 3.7(b) XRD profile of grown crystal.

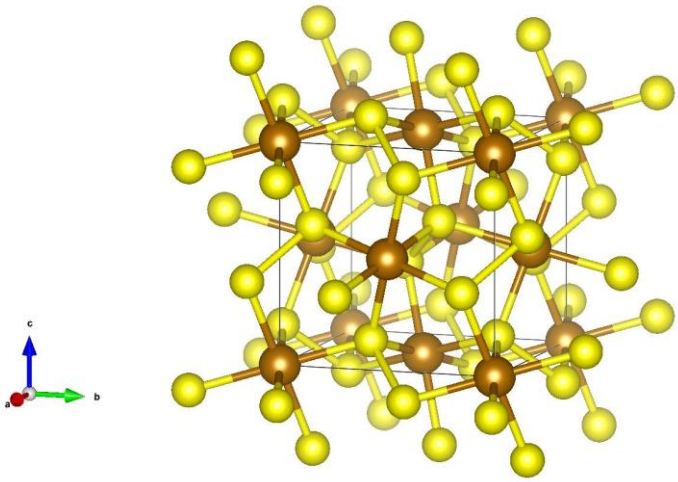

Fig. 3.8 A view of the experimentally determined iron pyrite unit cell by micro crystal X-ray diffraction. Brown spheres are iron ions, and yellow spheres are sulfur ions.

Table III.I Crystal data of iron pyrite single crystal by micro crystal X-ray diffraction

Crystal and structure data	
Empirical formula	FeS_2
Formula weight	119.97
Temperature	103 K
Crystal system	Cubic
Lattice type	Primitive
Space group	Pa-3
Unit cell dimensions	a = 5.40875(19) Å
Unit cell volume	V = 158.231(10) $Å^3$
Density	5.036 g/cm^3
F(000)	232.00
Absorption of coefficient (MoKα)	115.027 cm^{-1}
Lengths of Fe-S	2.2610(9) Å
Lengths of S-S	2.1502(13) Å
Angles of S-Fe-S	85.68(3)°, 94.32(3)
Angles of S-S-Fe	102.42(4)°
Angles of Fe-S-Fe	115.51(4)°

3.4 Evaluation of Composition Ratio in Iron Pyrite Single Crystal by Electron Probe Micro Analyzer

To evaluate composition ratio of iron pyrite single crystal wafers, electron probe micro analyzer (EPMA) was performed with SHIMADZU EPMA-1610. Samples were treated by aqua regia solution for 1 min before measurement. Table III.II shows the results of quantitative analysis for Fe and S. In this time, three points were measured per one sample. In Table III.II, molar ratios are shown. As shown in Table III.II, molar ratios of Fe and S were 33.349–33.574 % and 66.426–66.651 %, respectively. Therefore, it was found that sulfur in iron pyrite single crystal wafers is less than stoichiometric ratio of Fe : S = 1 : 2.

In addition, qualitative analysis were performed on these samples, however no other elements than Fe and S are detected.

Table III.II Molar ratio (%) of Fe and S in iron pyrite single crystal

	Molar ratio (%)	Sample1	Sample2	Sample3	Sample4	Sample5
1	Fe	33.692	33.202	33.811	33.562	33.553
	S	66.308	66.798	66.189	66.438	66.447
2	Fe	32.824	33.696	33.262	33.329	33.527
	S	67.176	66.304	66.738	66.671	66.473
3	Fe	33.532	33.746	33.648	33.475	33.544
	S	66.468	66.254	66.352	66.525	66.456
Ave.	Fe	33.349	33.548	33.574	33.455	33.541
	S	66.651	66.452	66.426	66.545	66.459

3.5 Surface treatment by aqua regia etching

3.5.1 Experimental detail

Iron pyrite single crystal wafers were made by mechanical processing such as slicing the samples with SiC wheel saw and polishing the samples with a series of emery papers and buff sheet. For cleaning particles on wafers, wafers were washed by ultrasonic cleaning in acetone for 10 min. After that, the wafers were washed by ultrasonic cleaning in ethanol for 10 min. In addition, the wafers were etched in aqua regia diluted double with acetic acid for 1min, and immediately rinsed in ethanol.

In this section, Micro-Raman spectroscopy, XPS and AFM were performed, respectively. To compare the surface condition of iron pyrite single crystal, the samples only treated by alcohol washing and the samples treated by both alcohol washing and aqua regia etching were measured, respectively.

3.5.2 Micro-Raman spectroscopy

Micro-Raman spectroscopy were performed to evaluate the phase purity at surface of iron pyrite single crystal wafer. The samples only treated by alcohol washing and the samples treated by both alcohol washing and aqua regia etching were utilized, respectively. Micro-Raman spectroscopy utilized JASCO NRS-4100 with a 50× objective lens and a 532 nm excitation laser operating. Samples were measured in air.

Figure 3.9(a) shows the Raman spectrum of iron pyrite single crystal treated by alcohol washing. Three peaks are detected at 348 cm^{-1}, 383 cm^{-1} and 433 cm^{-1}, and each peak is shifted to high wavenumbers with comparing some references [9-11]. In previous reports, Raman spectra of iron pyrite have shown three peaks corresponding to the characteristic active modes for iron pyrite of S_2 vibration (E_{ge}) mode at 343 cm^{-1}, S-S in-phase stretch (A_{ge}) mode at 377

cm^{-1}, and coupled vibration and stretch ($T_{ge(3)}$) mode at 430 cm^{-1} [9-11]. Therefore, mechanical process such as slicing and polishing might have applied compressive stress to the sample because all peaks were shifted to high wavenumbers of reference data and the line width of the peaks became thick.

In contrast, Fig. 3.9(b) shows the Raman spectra of iron pyrite single crystal treated by both alcohol washing and aqua regia etching. As shown in Fig. 3.9(b), three sharp peaks are confirmed at 343 cm^{-1}, 377 cm^{-1} and 430 cm^{-1}. Since these peaks corresponds to reference data, other phase such as FeS_2 marcasite and pyrrhotite are never detected. In addition, compressive stress at surface region has been improved by aqua regia etching.

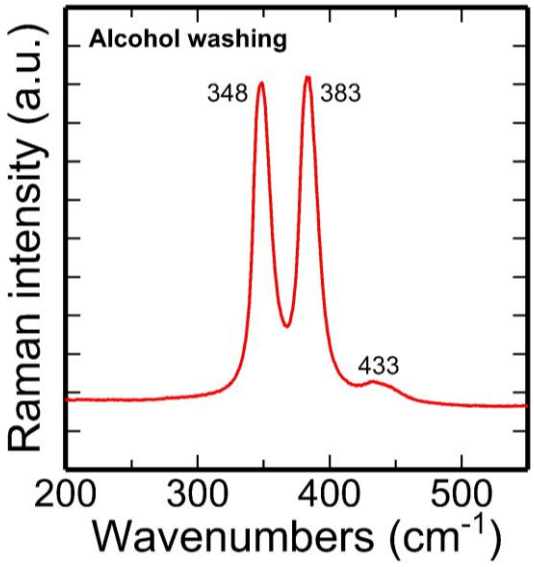

Fig. 3.9(a) Typical Raman spectra of iron pyrite single crystal treated by alcohol washing. Each peak position is different with previous data [7-9].

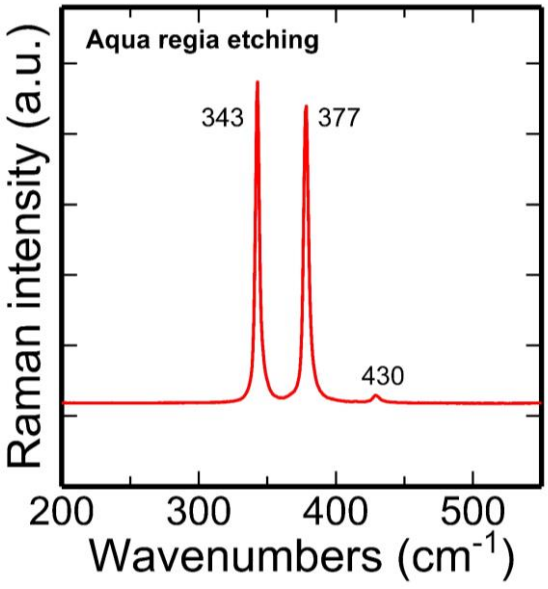

Fig. 3.9(b) Typical Raman spectra of iron pyrite single crystal treated by both alcohol washing and aqua regia etching. After aqua regia etching, each peak position corresponds to previous data [7-9].

3.5.3 X-ray photoelectron spectroscopy

XPS was performed by ULVAC-PHI PHI5000 VersaProbe II. Collected XPS spectra were analyzed by utilizing ULVAC-PHI MultiPak software. All spectra were calibrated with C 1s peak with a fixed value of 284.8 eV. After calibration, the background from each spectrum was subtracted by using a Shirley type background to remove most of the extrinsic loss structure. All survey scans were analyzed to determine the stoichiometry of the compound by using the appropriate sensitivity factors.

Figure 3.10(a) shows O 1s spectrum of iron pyrite single crystal treated by alcohol washing, and Fig. 3.10(b) shows O 1s spectrum of the sample treated by both alcohol washing and aqua regia etching. In Fig. 3.10(a), three bands at 530.2 eV, 531.6 eV and 532.8 eV are obtained in O 1s spectrum, and these bands are likely due to oxide (O^{2-}), hydroxide (OH^-) and other oxide (contaminant) [11]. Such oxide and hydroxide are formed by reaction with water due to mechanical processing such as cutting and polishing. O 1s spectrum in Fig. 3.10(b) also shows three bands at 530.4 eV, 531.9 eV and 533.1 eV, and these peaks corresponds to oxide (O^{2-}), hydroxide (OH^-) and other oxide (contaminant). However, the intensity of O 1s spectrum in Fig. 3.10(b) is smaller than the spectrum in Fig. 3.10(a). This result suggests that aqua regia reacts with surface of iron pyrite single crystal and removes oxide compounds. However, weak O 1s spectrum in Fig. 3.10(b) is detected although the sample was treated by aqua regia solution. These oxides should be formed by reaction with moisture in the air [11].

Figure 3.11(a) shows the depth profiles of O 1s spectrum by Ar^+ ion sputtering. Iron pyrite single crystal treated by alcohol washing was measured. From Fig. 3.11(a), while hydroxide (OH^-) specie immediately is removed by Ar^+ ion sputtering, oxide (O^{2-}) specie is even confirmed after sputtering. In contrast, Fig. 3.11(b) shows the depth profiles of O 1s spectrum of iron pyrite single crystal treated by both alcohol washing and aqua regia etching. As shown in Fig. 3.11(b), oxide productions such as hydroxide (OH^-) specie and oxide (O^{2-}) specie are

not detected after Ar^+ ion sputtering.

From these results of Fig. 3.10 and Fig. 3.11, mechanical processing forms oxide layer at the surface layer of iron pyrite single crystal due to reaction with water. This layer was removed after aqua regia etching, however moisture in the air should be absorbed at surface of iron pyrite because of exposure to the atmosphere during preparation for measurement.

Figure 3.12(a) shows S 2p spectrum of iron pyrite single crystal treated by alcohol washing, and Fig. 3.12(b) shows S 2p spectrum of the sample treated by both alcohol washing and aqua regia etching. These spectra were fitted with S $2p_{3/2}$–S $2p_{1/2}$ spin orbit doublets with a fixed 2 : 1 intensity ratio and 1.2 eV separation in both Fig. 3.12(a) and (b), which are due to S_2^{2-} anions in iron pyrite [12]. Additionally, a high binding energy shoulder features are observed at 164–167 eV, which corresponds to satellite. As other components, monosulfide (S^{2-}) at 161–164 eV are also observed in these spectra [12]. Moreover, S 2p spectrum of the sample only treated by alcohol washing shows sulphite (SO_3^{2-}) and sulfate (SO_4^{2-}) at 166–171 eV as shown in Fig. 3.12(a) [13]. While these bonds of sulphite and sulfate are also formed by mechanical processing, aqua regia solution removes them as shown in Fig. 3.12(b).

Figure 3.13(a) shows Fe 2p spectrum of iron pyrite single crystal treated by alcohol washing, and Fig. 3.13(b) shows Fe 2p spectrum of the sample treated by both alcohol washing and aqua regia etching. Photoelectron intensity of Fe $2p_{3/2}$ peak in Fig. 3.13(b) is bigger than the intensity of Fe $2p_{3/2}$ peak in Fig. 3.13(a). To analyze the high resolution Fe 2p spectra, Shirley background was utilized for the Fe $2p_{3/2}$ envelope. The Fe $2p_{3/2}$ envelope from compounds containing a high-spin Fe cation was fitted by peaks corresponding to the GS multiplets and satellites [2, 11, 13-15]. GS multiplets are patterns calculated by Gupta and Sen for free ions of various transition metals [16, 17]. Gupta and Sen remark that the number of unpaired electrons determines the number and intensity of the signal related to multiplets whereas the binding energy shift is a function of the atomic number [16, 17].

Figure 3.14(a) shows the Fe $2p_{3/2}$ spectrum of iron pyrite single crystal treated by alcohol washing and calculation result by fitting. From Fig. 3.14(a), the Fe $2p_{3/2}$ spectrum was fitted by many bands such as Fe^{2+} bulk at 707.15 eV, Fe^{2+} multiplets at 707–711 eV, Fe^{3+} multiplets at 709–714 eV and satellite peak at 714.0 eV. These bands are explained by LFT [1, 2, 13]. Fe^{2+} in the iron pyrite bulk has six paired electrons at the 3d t_{2g} level and is consequently represented by a narrow single peak in the Fe $2p_{3/2}$ spectrum with a binding energy of 707.15 eV [2, 13]. In contrast, Fe^{2+} multiplet splitting is associated with high-spin Fe^{2+} compounds at surface sites of iron pyrite [2, 11, 13]. Presence of a Fe–S bond leads to Fe^{2+} surface states with reduced coordination symmetry. As it was shown by Bronold et al. [1], the symmetry changes from an octahedral (O_h) to a square pyramidal (C_{4v}) ligand field leads to stabilization of the d_{z2} orbital and destabilization of the d_{xy} orbital as shown in Fig. 3.15 [1]. The energy separating the two new states (a_1 and b_2) above the valence band (0.35 eV) is lower than the electron pairing energy. Therefore unpaired electrons leads to high-spin Fe^{2+} compounds at surface sites and formed multiplet splitting in Fe 2p spectra. Since monosulfide (S^{2-}) is observed from S 2p spectra in Fig. 3.13, it is considered to reduce Fe coordination at surface region. In addition, Fe^{3+} multiplet splitting of the Fe $2p_{3/2}$ signal is associated with high-spin Fe^{3+} oxide productions such as FeOOH, Fe_2O_3, iron sulphate and hydrogen sulphate [11, 13, 14, 18, 19]. According to results of S 2p and O 1s spectra of the sample treated by alcohol washing, various oxide productions are formed at the surface of iron pyrite due to the reaction between the surface of iron pyrite and water during mechanical processing. Additionally, previous report about XPS Fe 2p spectra of iron oxide compounds indicated the single peak between 709–715 eV and Fe^{3+} multiplet splitting [11, 13, 14, 18, 19].

Fe $2p_{3/2}$ spectrum of the sample treated by both alcohol washing and aqua regia etching in Fig. 3.14(b) is different with Fe $2p_{3/2}$ spectrum of the sample only treated by alcohol washing in Fig. 3.14(a). The intensity of a narrow single peak in the Fe $2p_{3/2}$ spectrum with a binding

energy of 707.15 eV increases and different broad single peak between 708−716 eV is not detected. Instead of broad single peak, tail on the high binding energy side of the main peak are detected. This tail also includes Fe^{2+} and Fe^{3+} multiplet splitting of the Fe $2p_{3/2}$ signal by utilizing the GS mulitplet as shown in Fig. 3.14(c). These multiplet corresponds to high-spin Fe^{2+} compounds at surface sites and high-spin Fe^{3+} oxide productions [11, 13, 14, 18, 19].

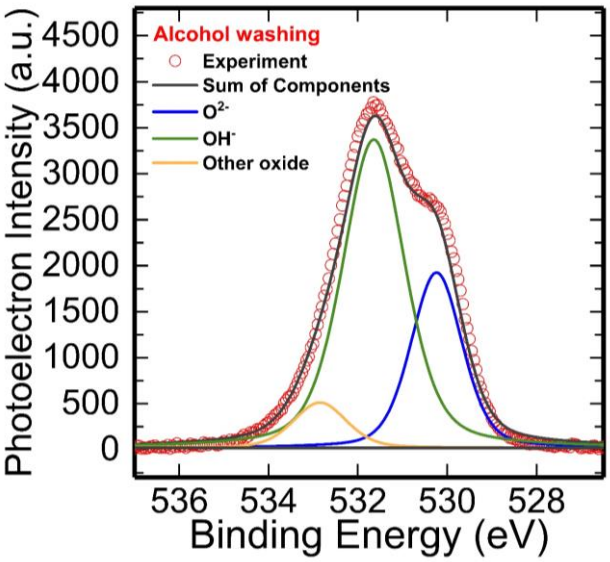

Fig. 3.10(a) XPS spectrum of O 1s for iron pyrite single crystal treated by alcohol washing.

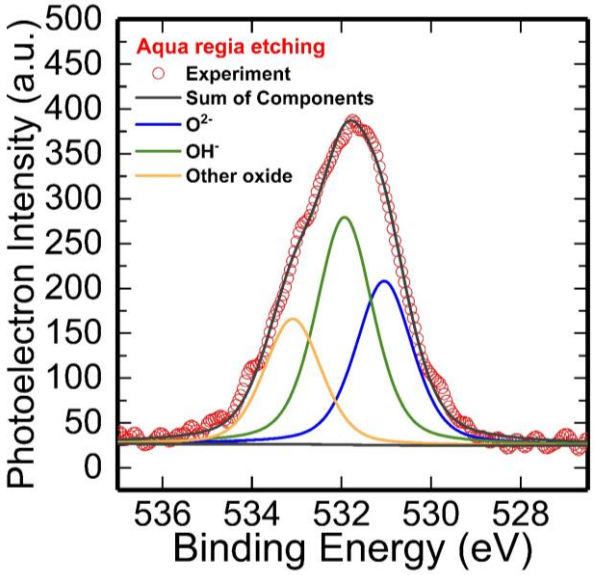

Fig. 3.10(b) XPS spectrum of O 1s for iron pyrite single crystal treated by both both alcohol washing and aqua regia etching.

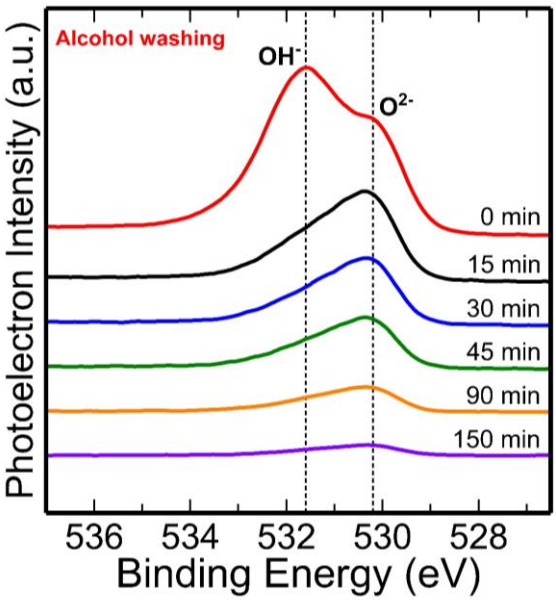

Fig. 3.11(a) XPS depth profiles of O 1s for iron pyrite single crystal treated by alcohol washing. The surface of the crystal was etched with Ar^+ ion gas for 150 min, and XPS measurement was performed every 15 min.

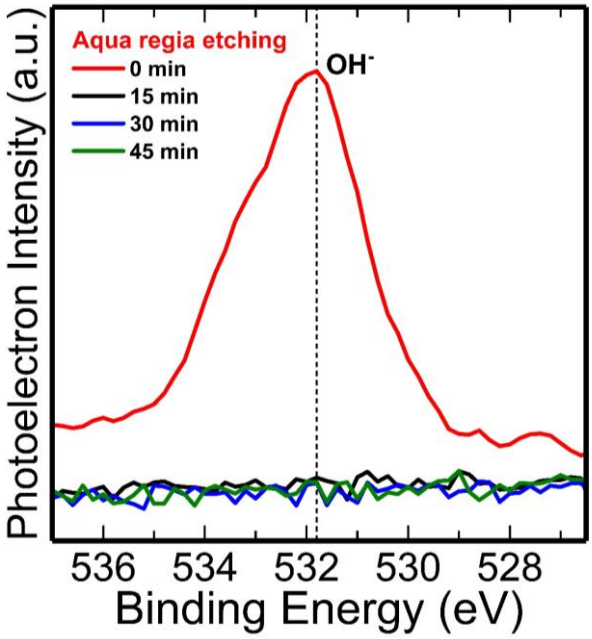

Fig. 3.11(b) XPS depth profiles of O 1s for iron pyrite single crystal treated by both both alcohol washing and aqua regia etching. The surface of the crystal was etched with Ar^+ ion gas for 45 min, and XPS measurement was performed every 15 min.

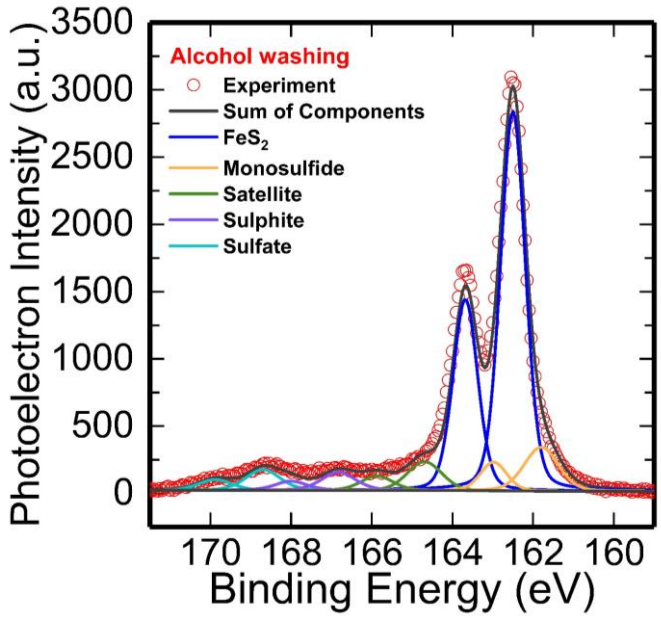

Fig. 3.12(a) XPS spectrum of S 2p for iron pyrite single crystal treated by alcohol washing.

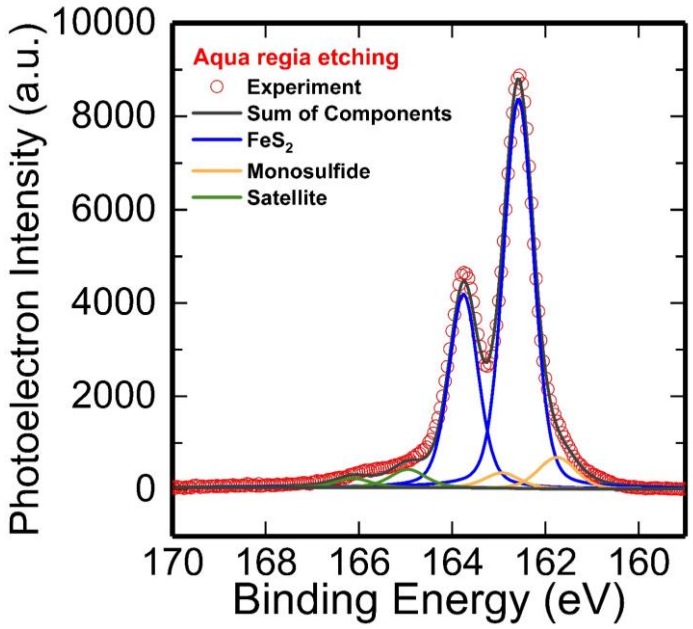

Fig. 3.12(b) XPS spectrum of S 2p for iron pyrite single crystal treated by both both alcohol washing and aqua regia etching.

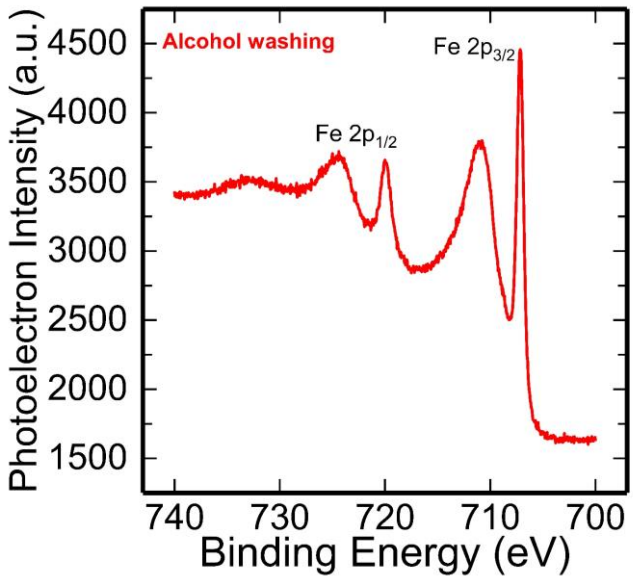

Fig. 3.13(a) XPS spectrum of Fe 2p for iron pyrite single crystal treated by alcohol washing.

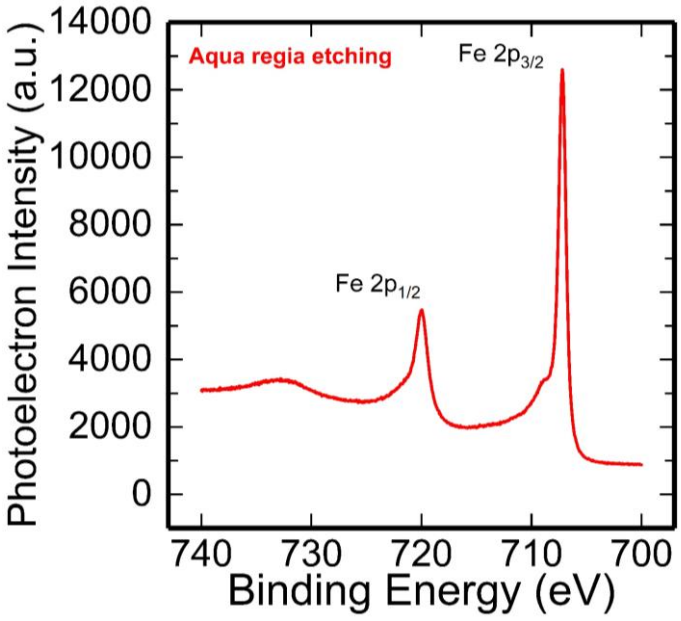

Fig. 3.13(b) XPS spectrum of Fe 2p for iron pyrite single crystal treated by both both alcohol washing and aqua regia etching.

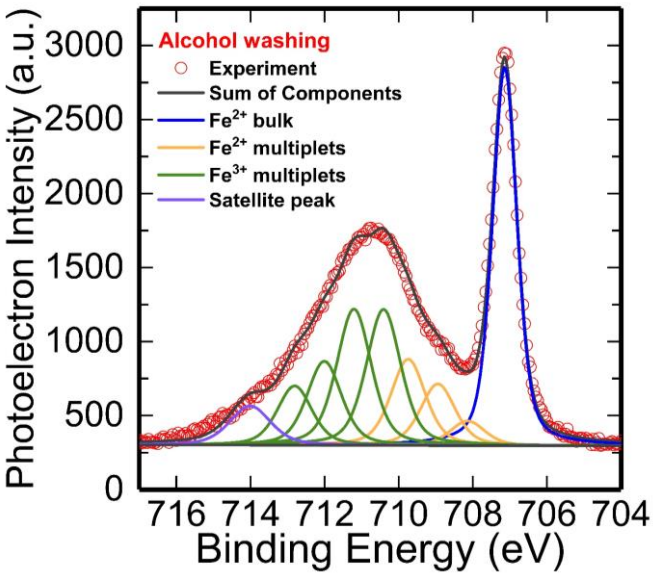

Fig. 3.14(a) XPS spectrum of Fe $2p_{3/2}$ for iron pyrite single crystal treated by alcohol washing.

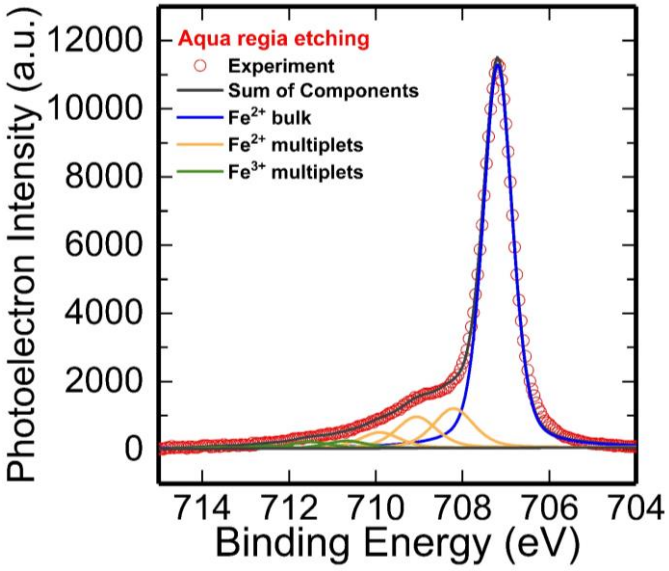

Fig. 3.14(b) XPS spectrum of Fe $2p_{3/2}$ for iron pyrite single crystal treated by both both alcohol washing and aqua regia etching.

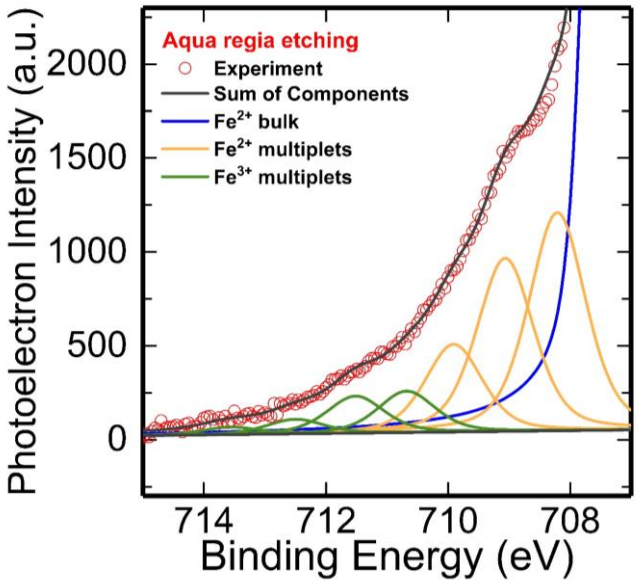

Fig. 3.14(c) Magnified figure at high energy tail region of Fig. 3.12(b).

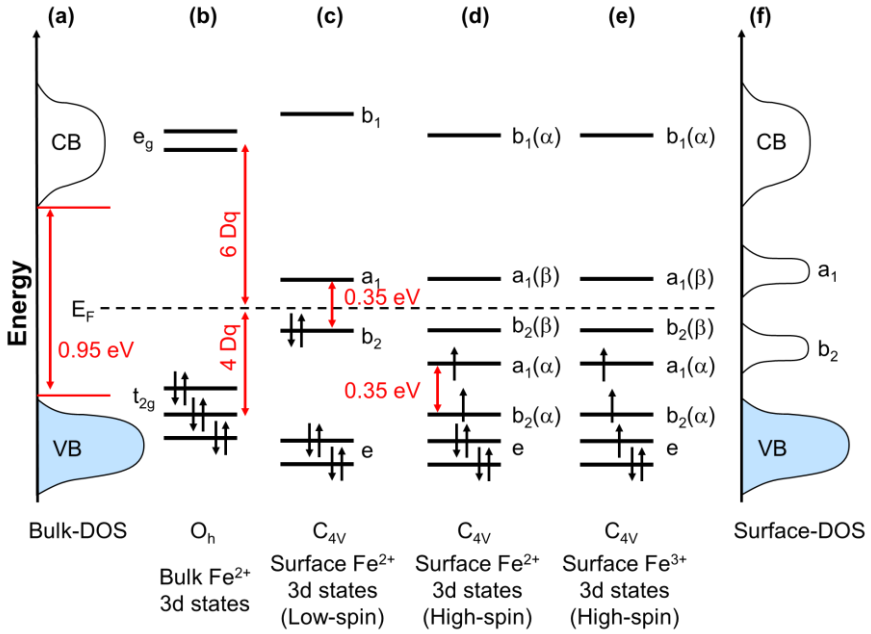

Fig. 3.15 The Fe (3d) ligand field splitting due to reduced coordination resulting from fracture. **(a)** The bulk density of states (DOS) for iron pyrite. **(b)** The electronic levels for Fe^{2+} in bulk iron pyrite in octahedral coordination (O_h). **(c)** Electronic levels of surface low-spin Fe^{2+} in square pyramidal coordination (C_{4V}). **(d)** Electronic levels of surface high-spin Fe^{2+} in square pyramidal coordination (C_{4V}) with unpaired electron. **(e)** Electronic levels of surface high-spin Fe^{3+} in square pyramidal coordination (C_{4V}) with unpaired electron. **(f)** The surface density of states (DOS) for iron pyrite. The ordinate is not drawn to scale. CB denotes conduction band and VB denotes the valence band. The energy separating a_1 and b_2 in (c), (d) and (e) is 0.35 eV and the electron pairing energy is about 1.6 eV for square pyramidal symmetry [1,2].

3.5.4 Atomic force microscope

AFM in a dynamic mode was performed by SHIMADZU SPM-9600 to measure the roughness of iron pyrite single crystal wafer. In a dynamic mode, non-contact scanning of the cantilever is performed with vibrating of the cantilever at resonant frequency. In this time, EFM-50 (NANOWORLD) was utilized as the cantilever of dynamic mode scan. Scan area was 5 × 5 μm.

Figure 3.16(a) shows the surface image of iron pyrite single crystal treated by alcohol washing. As shown in Fig. 3.16(a), a lot of particles at the surface are observed although the sample was treated by alcohol washing. The largest particle size is about 30 nm, and the value of room-mean-square height (Rq) is 2.210 nm. Figure 3.16(b) shows the surface image of iron pyrite single crystal treated by both alcohol washing and aqua regia etching. As shown in Fig. 3.16(b), while particles at the surface are not observed after aqua regia etching, Rq increases to 7.296 nm. It is indicated that aqua regia solution reacts with the surface of iron pyrite single crystal, and the surface roughness becomes worse.

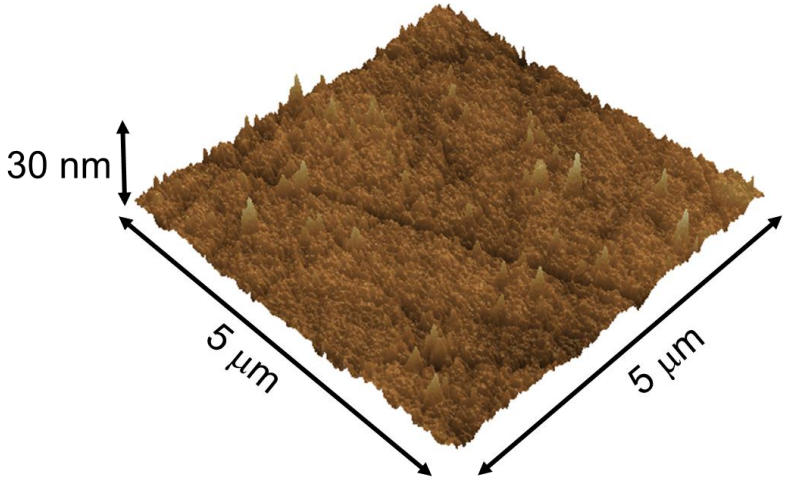

Fig. 3.16(a) AFM image of iron pyrite single crystal treated by alcohol washing. Scan area is 5 × 5 µm. Rq is 2.210 nm.

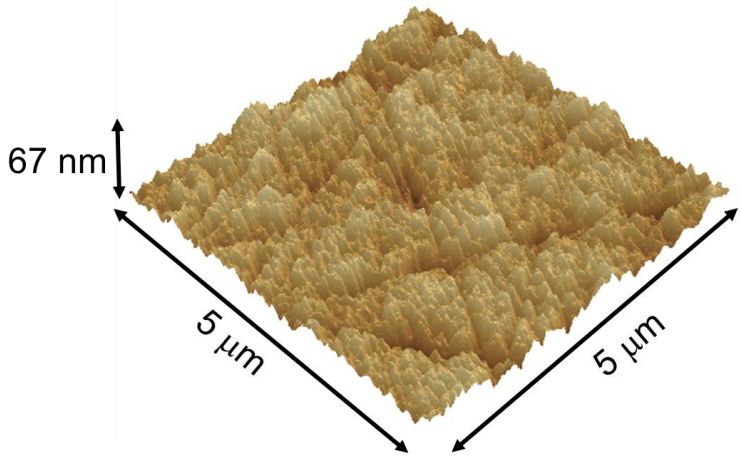

Fig. 3.16(b) AFM image of iron pyrite single crystal treated by both alcohol washing and aqua regia etching. Scan area is 5 × 5 µm. Rq is 7.296 nm.

3.5.5 Discussion

From the Micro-Raman spectroscopy, stress at surface region of iron pyrite formed by mechanical processing was improved by aqua regia etching. After aqua regia etching, Raman spectrum showed three modes as S_2 vibration (E_{ge}) mode, S-S in-phase stretch (A_{ge}) mode and coupled vibration and stretch ($T_{ge(3)}$) mode.

From XPS, oxide productions formed at surface of iron pyrite were removed by aqua regia etching because the intensity of O 1s spectrum and oxide peaks of Fe $2p_{3/2}$ and S 2p spectra decreased. However, Fe $2p_{3/2}$ spectrum of the sample treated by aqua regia solution showed the Fe^{3+} multiplet corresponding to oxide productions. This result suggests that the surface of iron pyrite immediately reacts with moisture in air. In this time, the samples were set in the vacuum chamber of XPS within 5 min after etching samples. This phenomena is explained by DFT study. DFT study suggests that oxidation at the surface of iron pyrite occurs through reactions of the surface with adsorbed O_2 and water molecules [21]. Firstly, O_2 and water molecules are found to adsorb at undercoordinated surface Fe atoms, and it is energetically favorable for adsorbed O_2 to dissociate. This dissociation leads to the formation of ferryl-oxo, $Fe^{4+}=O^{2-}$ species. The presence of undercoorinated Fe atoms at surface is possible because the S2p spectrum of the sample etched by aqua regia solution shows the monosulfides. Water molecules can form H-bonds with $Fe^{4+}=O^{2-}$ species, and proton-coupled electron transfer through the H-bond leads to the formation of ferric-hydroxo, $Fe^{3+}–OH^-$, groups. Their calculation indicates that these groups are predicted to fully cover the surface of iron pyrite when this is exposed to air under normal conditions. Therefore, the results of Fe $2p_{3/2}$ spectra and O 1s spectra suggests that aqua regia solution can dissolve the oxide at the surface of iron pyrite, however O_2 and water in air quickly react with the surface of iron pyrite and form $Fe^{3+}–OH^-$ species. On the other hand, Fe $2p_{3/2}$ spectra showed the Fe^{2+} multiplets. These multiplets are associated with the presence of a Fe–S bond which leads to high-spin Fe^{2+} surface states with reduced

coordination symmetry. Reduced coordination symmetry of iron is indicated by monosulfide of S 2p spectrum and oxygen dissociative adsorption. High-spin Fe^{2+} is possible to create acceptor level and lead to band bending.

As discussed above, high-spin Fe^{2+} and oxide were observed although aqua regia solution etched oxidation layer at the surface region of iron pyrite single crystal. To investigate the effect of high-spin Fe^{2+} and oxide, I will evaluate the band structure and electrical transport of iron pyrite single crystal and discuss these evaluations in Chapter 4.

3.6 Summary

Iron pyrite bulk crystal was grown by flux method and confirmed as single crystal by XRD measurement. To evaluate surface condition of iron pyrite single crystal, Micro-Raman spectroscopy and XPS were performed. Micro-Raman spectroscopy indicated that the crystalline at the surface region of iron pyrite single crystal was improved by aqua regia etching. While the surface crystalline degenerated through the mechanical processing, aqua regia solution removed poor crystalline layer. Aqua regia solution also removed the oxidation layer at surface region of iron pyrite single crystal from results of XPS. While photoelectron intensity of O 1s spectrum decreased after aqua regia etching, the intensity of $Fe2p_{3/2}$ and S 2p spectra increased. However, O 1s spectrum and Fe^{3+} multiplet were observed after aqua regia etching although this solution removed the oxide productions. This result suggests the oxide and water in air immediately reacts the surface of iron pyrite and creats $Fe^{3+}{-}OH^{-}$ species. Moreover XPS analysis revealed the presence of high-spin Fe^{2+} which is possible to form acceptor level in band gap. Therefore, $Fe^{3+}{-}OH^{-}$ species and high-spin Fe^{2+} considered to be a cause of the inversion layer at surface region have been observed after aqua regia etching. In Chapter 4, I will evaluate and discuss the band structure and electrical transport to investigate the effect by aqua regia etching.

Reference

[1] M. Bronold, Y. Tomm, W. Jaegermann, Sur. Sci. Lett. 314 (1994) L931-L936.

[2] H. W. Nesbitt, G. M. Bancroft, A. R. Pratt, M. J. Scaini, Am. Mineral. 83 (1998) 1067–1076.

[3] M. Bronold, K. Büker, S. Kubala, C. Pettenkofer, H. Tributsch, Phys. Status Solidi A 135 (1993) 231-243.

[4] A. Ennaoui, S. Fiechter, N. Pettenkofer, N. Alonso‐Vante, K. Büker, M. Bronold, C. Höpfner, H. Tributsch, Sol. Energy Mater. Sol. Cells 29 (1993) 289-427.

[5] C. M. Eggleston, J.-J. Ehrhardt, W. Stumm, Am. Mineral. 81 (1996) 1036-1056.

[6] X. Zhang, M. Manno, A. Baruth, M. Johnson, E. S. Aydil, C. Leighton, ACS Nano 7 (2013) 2781-2789.

[7] J. Sangster, A. D. Pelton, J. Phase Equilib. 18 (1997) 89-96.

[8] P. Waldner, A. D. Pelton, J. Phase Equilib. Diff. 26 (2005) 23-38.

[9] A. K. Kleppe, A. P. Jephcoat, Mineral. Mag. 68 (2004) 433-441.

[10] M. Caban-Acevedo, N. S. Kaiser, C. R. English, D. Liang, B. J. Thompson, H. E. Chen, K. J. Czech, J. C. Wright, R. J. Hamers, S. Jin, J. Am. Chem. Soc. 136 (2014) 17163-17179.

[11] M. Limpinsel, N. Farhi, N. Berry, J. Lindemuth, C. L. Perkins, Q. Lin, M. Law, Energy Environ. Sci. 7 (2014) 1974.

[12] H. W. Nesbitt, I. J. Muir, Geochim. Cosmochim. Acta 58 (1994) 4667-4679.

[13] Y. Mikhlin, Y. Tomashevich, S. Vorobyev, S. Saikova, A. Romanchenko, R. Felix, Appl. Surf. Sci. 387 (2016) 796-804.

[14] A. G. Schaufu, H. W. Nesbitt, I. Kartio, K. Laajalehto, G. M. Bancroft, R. Szargan, J. Electron. Spectrosc. Relat. Phenom. 96 (1998) 69-82.

[15] J. R. Mycroft, H. W. Nesbitt, A. R. Pratt, Geochim. Cosmochim. Acta 59 (1994) 721-733.

[16] H. W. Nesbitt, M. Scaini, H. Höchst, G. M. Bancroft, A. G. Schaufuss, R. Szargan, Am. Mineral. 85 (2000) 850-857.

[17] R. P. Gupta, S. K. Sen, Phys. Rev. B 10 (1974) 71-77.

[18] R. P. Gupta, S. K. Sen, Phys. Rev. B 12 (1975) 15-19.

[19] N. S. McIntyre, D. G. Zetaruk, Anal. Chem. 49 (1977) 1521-1529.

[20] A. P. Grosvenor, B. A. Kobe, M. C. Biesinger, N. S. McIntyre, Surf. Interface Anal. 36 (2004) 1564-1574.

[21] P. H. Sit, M. H. Cohen, A. Selloni, J. Phys. Chem. Lett. 3 (2012) 2409-2414.

Chapter 4

Evaluation on Band Structure of Iron Pyrite Single Crystal

4.1 Introduction

In Chapter 3, surface conditions were evaluated to investigate the effect of removing oxidation layer by aqua regia etching. Aqua regia solution also removed the oxidation layer at surface region of iron pyrite single crystal from results of XPS. However, O 1s spectrum and Fe^{3+} multiplets related to oxide productions were observed by XPS after aqua regia etching although the surface of iron pyrite was treated by aqua regia solution. This result suggested that oxide and water in air immediately reacted the surface of iron pyrite and created Fe^{3+}–OH^{-} species. Based on these results, the evaluation on band structure of iron pyrite single crystal was important to examine the effect of inversion layer and the relationship between the surface oxidation and band structure.

In this Chapter, photoelectron yield spectroscopy, Kelvin force microscopy, spectroscopic ellipsometry, Micro-photoluminescence were performed to evaluate the band structure of iron pyrite single crystal. In addition, Hall effect measurement was also performed to evaluate electronic transport of iron pyrite single crystals which was treated by aqua regia solution.

4.2 Evaluation on Band Structure of Iron Pyrite Single Crystal

4.2.1 Pretreatment of iron pyrite single crystal before measurement

Iron pyrite single crystal wafers were made by mechanical processing such as slicing the samples with SiC wheel saw and polishing the samples with a series of emery papers and buff sheet. For cleaning particles on wafers, wafers were washed by ultrasonic cleaning in acetone for 10 min. After that, the wafers were washed by ultrasonic cleaning in ethanol for 10 min. In addition, the wafers were etched in aqua regia diluted double with acetic acid for 1min, and immediately rinsed in ethanol. To compare the surface condition of iron pyrite single crystal, the samples only treated by alcohol washing and the samples treated by both alcohol washing and aqua regia etching were measured, respectively.

4.2.2 Photoelectron yield spectroscopy

Photoelectron yield spectroscopy (PYS) was performed by Riken Keiki AC-3 with ultraviolet light from deuterium lamp to evaluate ionization potential of iron pyrite single crystal. Measurement range was from 4.0 eV (310 nm) to 7.0 eV (177.1 nm) and measurement temperature was room temperature.

Figure 4.1(a) shows the emission yield plots of iron pyrite single crystal wafer treated by alcohol washing. Ionization potential is calculated by fitting the emission yield plots as shown in Fig. 4.1(a), and obtained ionization potential is 5.0 eV. In contrast, Fig. 4.1(b) shows the emission yield plots of iron pyrite single crystal treated by both alcohol washing and aqua regia etching. Calculated ionization potential is also 5.0 eV. Ionization potential corresponds to the energy difference between vacuum level and valence band maximum. Therefore, the energy difference between vacuum level and valence band maximum was 5.0 eV regardless of surface

treatment method. This result was similar with previous result reported as 4.9 eV by ultraviolet photoelectron spectroscopy (UPS) [1].

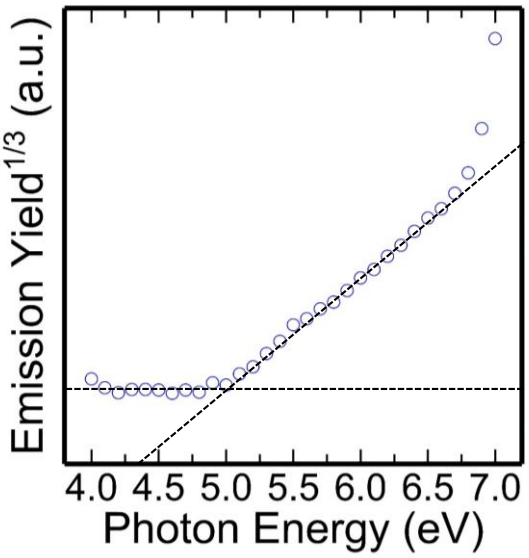

Fig. 4.1(a) Emission yield plot by PYS measurement of iron pyrite single crystal treated by alcohol washing.

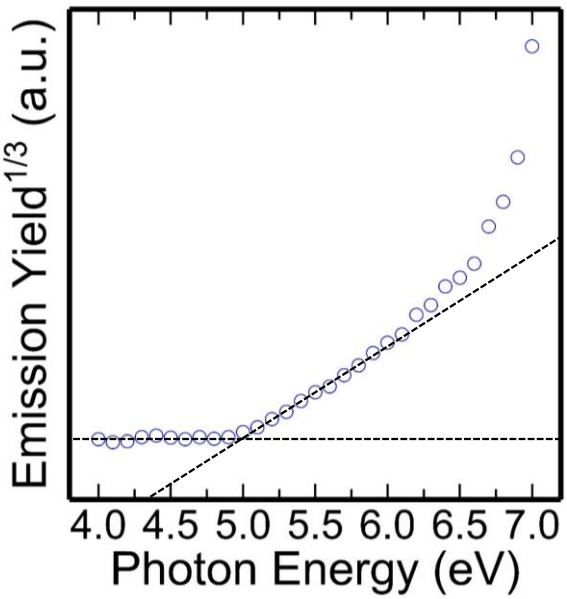

Fig. 4.1(b) Emission yield plot by PYS measurement of iron pyrite single crystal treated by both alcohol washing and aqua regia etching.

4.2.3 Kelvin force microscope

Kelvin force microscopy (KFM) was performed by SHIMADZU SPM-9600 to measure the surface potential of iron pyrite single crystal wafer. Surface potential was obtained by detecting electrostatic force between the cantilever and the surface of sample. Surface potential is defined as the energy required to draw electrons from the Fermi level and put it into the vacuum level. Surface potential depends on the material and its surface condition. Figure 4.2 shows an energy band diagram between the cantilever and sample for KFM measurements. When the cantilever and the sample are independent as shown Fig. 4.2(a), each potential difference $\Phi(P)$ and $\Phi(S)$ is given as from Eq. (4.1) and (4.2):

$$\boldsymbol{\Phi(P) = |E_{VAC} - E_F(P)|} \quad (\mathbf{4.1})$$

$$\boldsymbol{\Phi(S) = |E_{VAC} - E_F(S)|} \quad (\mathbf{4.2})$$

After the junction formation of the cantilever and the sample surface as shown in Fig. 4.2(b), $E_F(P)$ is equal to $E_F(P)$, and an electrostatic force occurs between the cantilever and the sample, which generates the difference in surface potential V_S. V_S is given as Eq. (4.3):

$$\boldsymbol{V_S = |\Phi(P) - \Phi(S)|} \quad (\mathbf{4.3})$$

Next, the cantilever is forcibly vibrated by applying the alternating current voltage V_{AC} to the cantilever at the resonant frequency ω_r as shown in Fig. 4.2(c). The ω_r changes due to the difference in potential of the sample surface, and this change is canceled out by feedback to direct current voltage V_{DC}. In the applying V_{DC} and V_{AC} at ω_m as shown in Fig. 4.2(c), the electrostatic force F is defined by the Eq. (4.4):

$$\boldsymbol{F = -\frac{1}{2}\frac{\partial C}{\partial Z}(V_s + V_{DC} + V_{AC}cos\omega_m t)^2} \quad (\mathbf{4.4.1})$$

$$\boldsymbol{= -\frac{1}{2}\frac{\partial C}{\partial Z}\{(V_s + V_{DC})^2 + 2(V_s + V_{DC})V_{AC}cos\omega_m t + {V_{AC}}^2 cos^2\omega_m t\}} \quad (\mathbf{4.4.2})$$

$$\boldsymbol{= -\frac{1}{2}\frac{\partial C}{\partial Z}\left\{(V_s + V_{DC})^2 + 2(V_s + V_{DC})V_{AC}cos\omega_m t + {V_{AC}}^2 \frac{cos2\omega_m t + 1}{2}\right\}} \quad (\mathbf{4.4.3})$$

Here, C is capacitance between the cantilever and the sample, and Z is distance between the cantilever and the sample. In the Eq. (4.4.3), first term indicates a static attraction force between the cantilever and sample. In addition, second term and third term indicate force from alternating electric field induced by surface charges and electrostatic force between the cantilever and sample generated by V_{AC}, respectively in Eq. (4.4.3). By performing feedback control of V_{DC} with the lock-in amplifier to cancel out the surface potential V_S, the difference in surface potential between the cantilever and the sample surface is calculated as $V_S = -V_{DC}$. In the KFM measurements, the cantilever does not contact to the sample surface at all times, because F does not become 0 if $V_S + V_{DC} = 0$. In this KFM measurement, EFM-50 (NANOWORLD) was utilized as the cantilever.

Firstly, surface potential of aluminum plate (99+%, Nilaco) and platinum plate (99.98%, Nilaco) were measured to confirm the polar characteristics of contact potential shown in measurement images. From Fig. 4.3(a) and 4.3(b), aluminum and platinum show positive and negative potential, respectively. Therefore in KFM measurement with SHIMADZU SPM-9600, positive V_{DC} is applied to the cantilever when work function of the cantilever is higher than the sample, and positive contact potential image shows that potential difference is equal to positive V_{DC} as shown Fig. 4.4(a). On the other hand, negative V_{DC} is applied to the cantilever when work function of the cantilever is lower than the sample as shown Fig. 4.4(b).

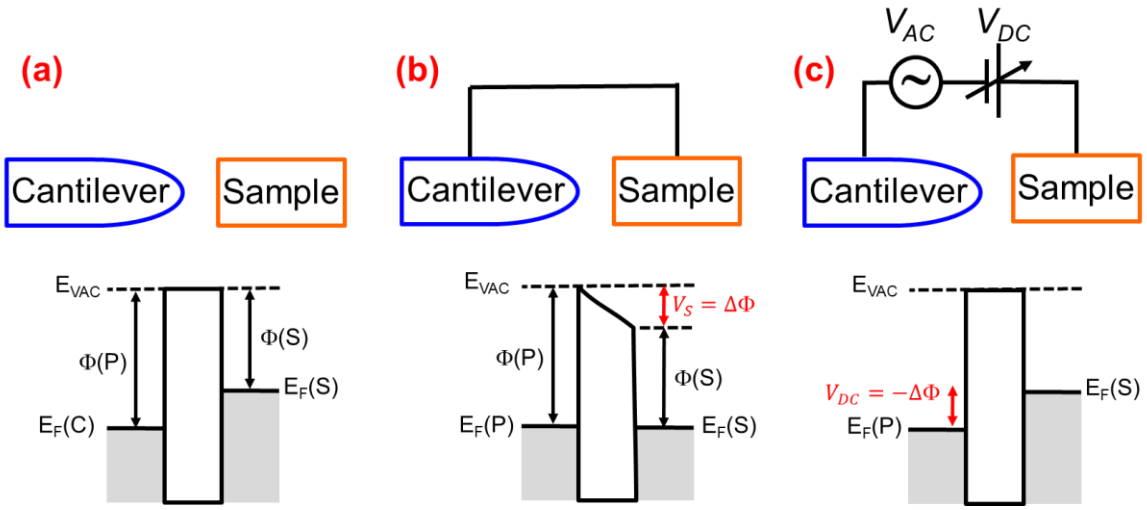

Fig. 4.2 Schematic diagram of contact potential difference by KFM measurement. **(a)** Independence between the cantilever and the sample. **(b)** Electrical contact between the cantilever and the sample. **(c)** Contact potential is canceled by applying bias voltage V_{DC}.

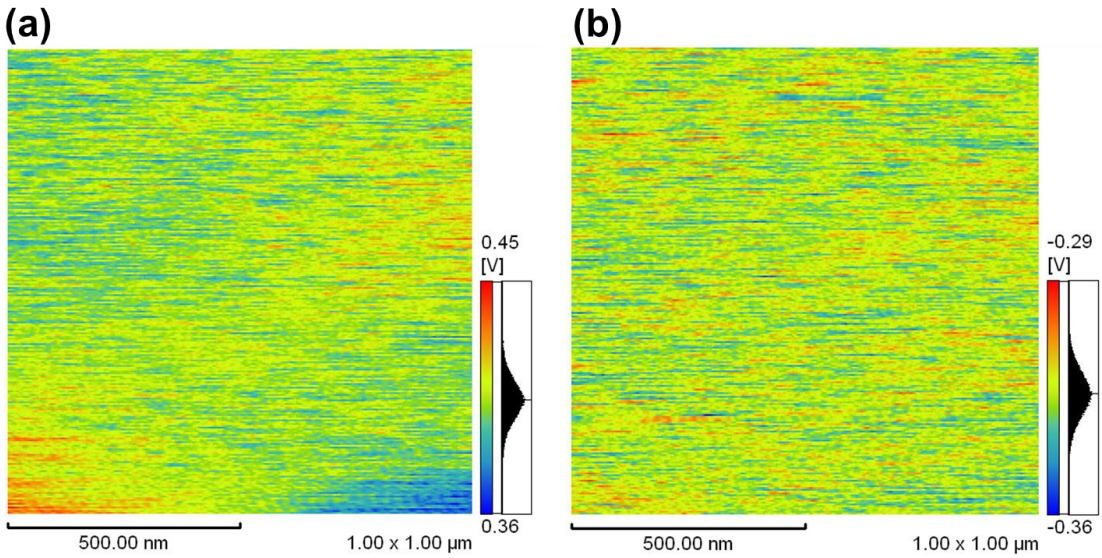

Fig. 4.3 Contact potential image. **(a)** Aluminum plate. **(b)** Platinum plate.

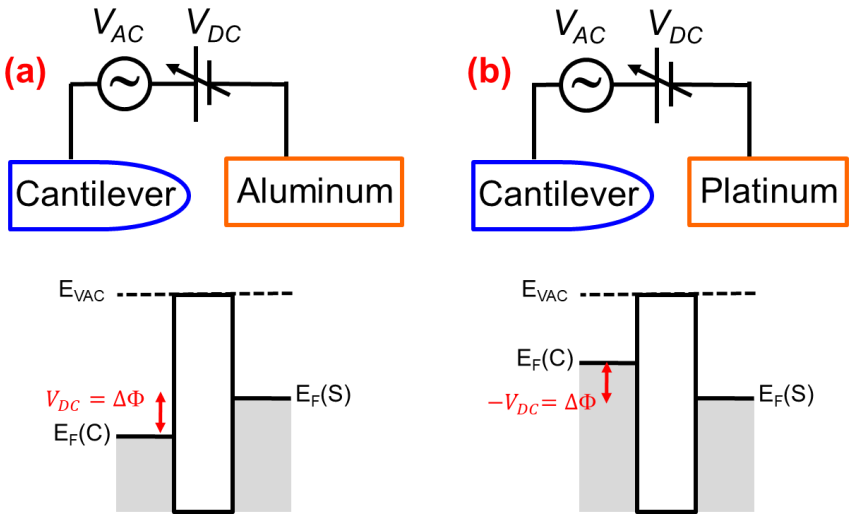

Fig. 4.4 Schematic diagram of contact potential difference with SHIMADZU SPM-9600. **(a)** Positive V_{DC} is applied to the cantilever when the low work function such as aluminum is measured. **(b)** Negative V_{DC} is applied to the cantilever when the high work function such as platinum is measured.

To measure the contact potential difference of iron pyrite single crystal wafer, iterative measurement was performed between the iron pyrite single crystal wafer and Au thin film on same sample holder as shown Fig. 4.5. Au thin film was deposited by thermal deposition on non-alkaline glass which was ultrasonically washed in ethanol solutions for 10 min. Deposited film thickness was 130 nm. Au thin film was fixed by silver paste on sample holder.

In this measurement, the contact potential difference of Au thin film was calibrated to 0.00 eV to evaluate contact potential difference of iron pyrite with Au thin film, which leads to the evaluation of Fermi level of iron pyrite. Figure 4.6 shows the calibrated contact potential difference and histogram. To compare the contact potential difference, the value of measured potential was taken as the median of the histogram. From Fig. 4.6, contact potential of Au thin film corresponds to 0.00 eV. In addition, the work function of Au thin film was measured by PYS as shown Fig. 4.7, which indicates that work function of Au thin film is 4.85 eV.

Figure 4.8 shows the result of iterative measurement between iron pyrite treated by alcohol washing and Au thin film. On the other hand, Fig. 4.9 shows the result of iterative measurement between iron pyrite treated by both alcohol washing and aqua regia etching and Au thin film. These measurement were performed under nitrogen atmosphere. Table IV.I summarizes these results of Fig. 4.8 and Fig. 4.9. Surface potentials shown in the table IV.I indicates potential difference from the work function of Au thin film. In this time, all potentials are positive, which results that the work function of iron pyrite is lower than Au thin film. Compared the potential difference in Table IV.I, the work function of the sample treated by only alcohol washing is 0.04 eV lower than the sample treated by both alcohol washing and aqua regia etching. Therefore, Fermi level of iron pyrite corresponds to 4.60 ~ 4.67 eV. From these results of PYS and KFM, energy difference between Fermi level and Valence band maximum was about 0.3 ~ 0.4 eV.

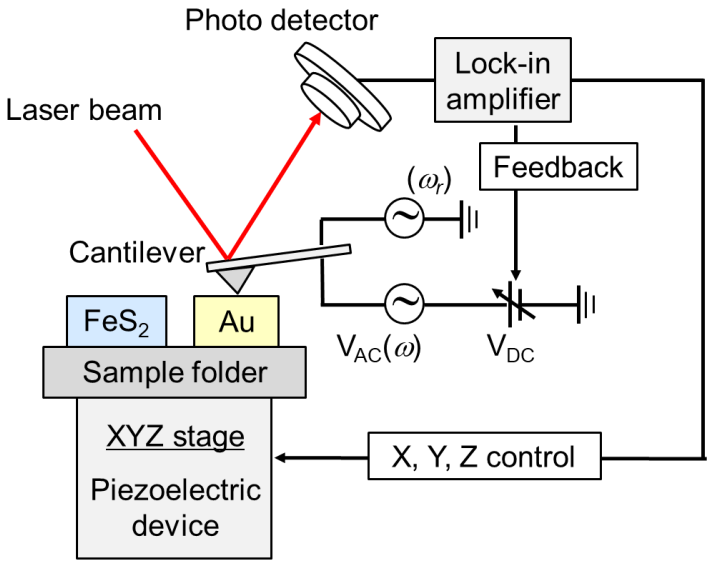

Fig. 4.5 Schematic illustration of iterative measurement between FeS_2 (iron pyrite single crystal) and Au thin film on same sample holder.

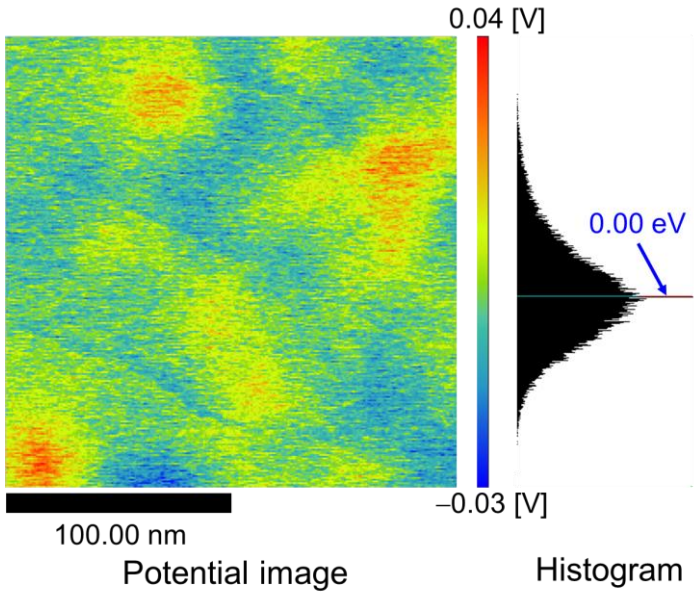

Fig. 4.6 Contact potential image of Au thin film calibrated to 0.00 eV. Based on potential image, the median of the histogram is calculated. This result shows that the median of Au thin film corresponds to 0.00 eV.

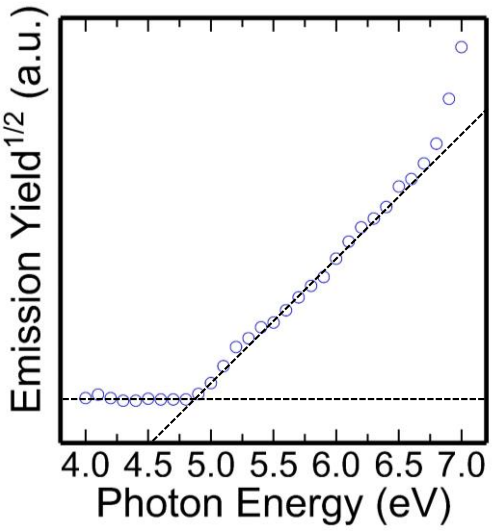

Fig. 4.7 PYS measurement of Au thin film. Work function is 4.85 eV.

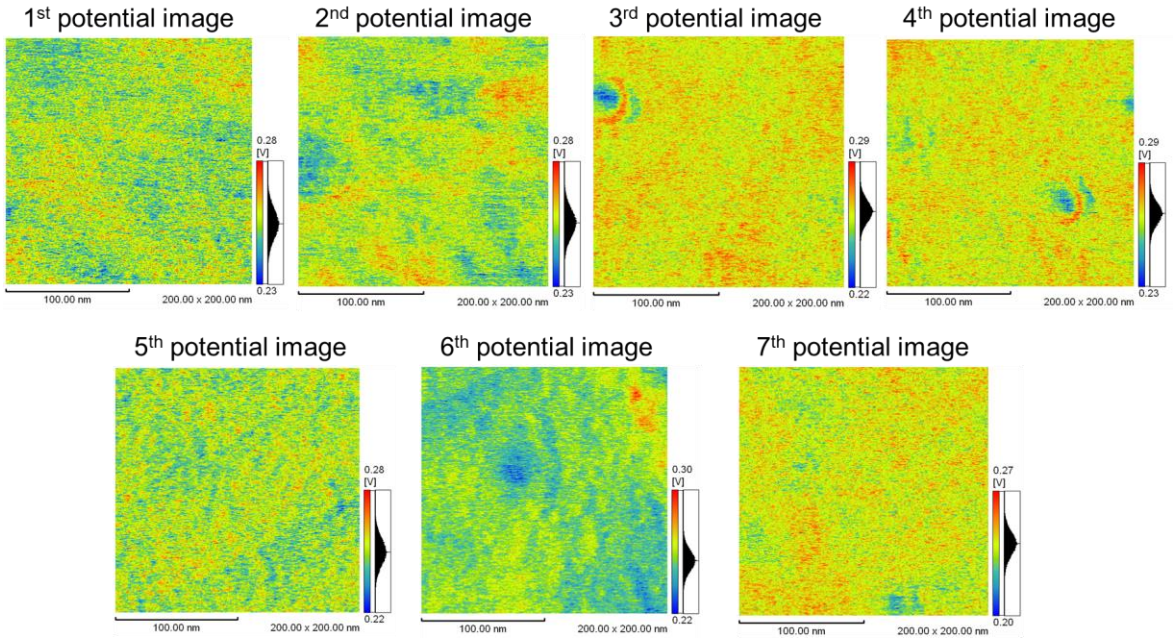

Fig. 4.8 Contact potential images of iron pyrite single crystal treated by alcohol washing. Iterative measurement of 7 times was performed.

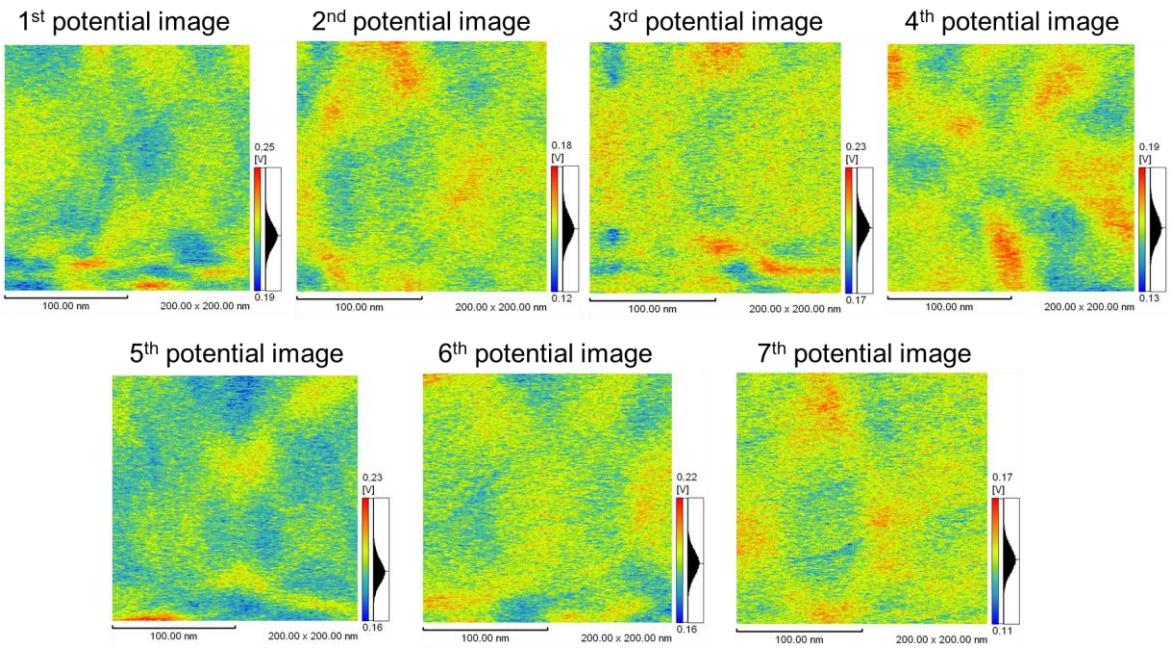

Fig. 4.9 Contact potential images of iron pyrite single crystal treated by both alcohol washing and aqua regia etching. Iterative measurement of 7 times was performed.

Table IV.I Summary of Fig. 4.8 and Fig. 4.9. This table shows contact potential difference between iron pyrite single crystal and Au thin film.

	Alcohol washing	Aqua regia etching
1st	+0.25 eV	+0.21 eV
2nd	+0.26 eV	+0.15 eV
3rd	+0.26 eV	+0.20 eV
4th	+0.27 eV	+0.16 eV
5th	+0.25 eV	+0.20 eV
6th	+0.25 eV	+0.19 eV
7th	+0.24 eV	+0.14 eV
Average	+0.25 eV	+0.18 eV
S.D.	0.01 eV	0.02 eV

4.2.4 Spectroscopic ellipsometry

Spectroscopic ellipsometry was performed by HORIBA JOBIN YVON UVISEL ER AGMS-NSD to measure optical absorption of iron pyrite single crystal wafer. Iron pyrite single crystal wafer was treated by both alcohol washing and aqua regia etching. Measurement region was from 300 nm to 2100 eV. Figure 4.10(a) shows refractive index $n(\lambda)$ and extinction coefficient $k(\lambda)$ and Fig. 4.10(b) shows optical absorption calculated from extinction coefficient. Optical absorption is calculated by Eq (4.5):

$$\alpha = \frac{4\pi k}{\lambda} \qquad (4.5)$$

An optical absorption coefficient $\alpha > 1 \times 10^5$ cm^{-1} for $h\nu > 0.74$ eV is obtained as shown in Fig. 4.10(b). From Tauc analysis, intercepts of the liner extrapolations of the different slopes on the energy axis could be interpreted as optical transitions corresponding to those specific energy levels. The electronic behavior of iron pyrite is governed by these energy level transitions. From Fig. 4.11(a), the band gap estimated is 1.0 eV. This result is well within the range commonly reported for iron pyrite. However, this band gap value appears to be direct as it fits linearly with n = 2 value in the parameter $(\alpha h\nu)^n$ in the Tauc equation, which shows in Fig. 4.11(b).

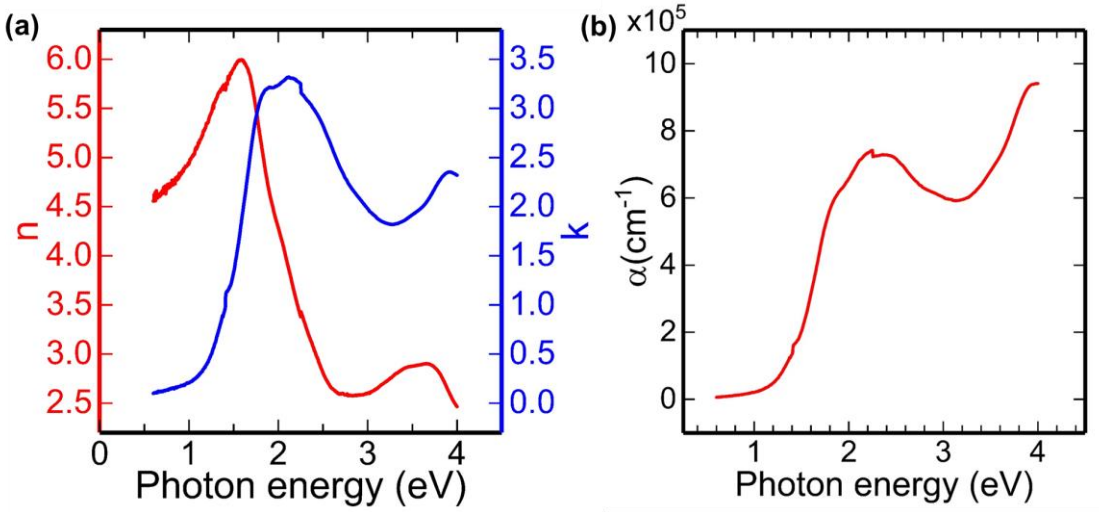

Fig. 4.10 Evaluation of optical characteristics of iron pyrite single crystal treated by aqua regia solution. **(a)** Refractive index $n(\lambda)$ and extinction coefficient $k(\lambda)$. **(b)** Optical absorption coefficient calculated by extinction coefficient $k(\lambda)$.

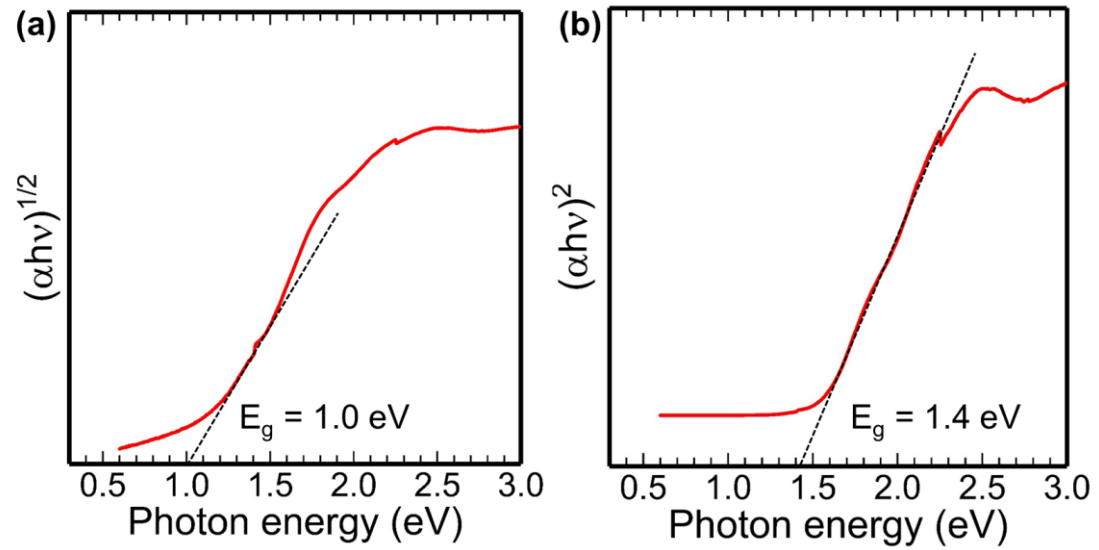

Fig. 4.11 Tauc plot analysis of iron pyrite single crystal. **(a)** Indirect band edge intercept at 1.0 eV. **(b)** Direct band edge intercept at 1.4 eV.

4.2.5 Micro-photoluminescence

The results of spectroscopic ellipsometry suggested direct transition although previous report considered electron transition of iron pyrite as indirect transition from band calculation [2]. Therefore, Micro-photoluminescence (Micro-PL) was performed to investigate the electron transition in band gap of iron pyrite. In addition, the effect of surface recombination by oxidation productions at iron pyrite surface was investigated by comparing differences of emission intensity and peak position of photoluminescence (PL) spectra between the sample only treated by alcohol washing and the sample treated by both alcohol washing and aqua regia etching. Micro-PL was performed with 635 nm excitation laser focused with spot size of few μm on the sample. Spectra were analyzed by a grating monochromator, and detected utilizing a Si-CCD detector to investigate measurement region from 750 nm to 1200 nm. Measurement temperature was room temperature (RT) and sample were measured in air.

Figure 4.12 shows PL spectra of iron pyrite single crystal wafers only treated by alcohol washing and treated by both alcohol washing and aqua regia etching, respectively. Emission intensity and peak position are similar in both spectra, and two peaks are observed in 1.316 eV and 1.358 eV. Emission intensity and peak position of spectrum are not changed after aqua regia etching, which suggests that the surface recombination is not changed although oxidation layer at iron pyrite surface was removed by aqua regia solution. Therefore, the formation of oxidation layer at the surface region of iron pyrite don't contribute to surface recombination. In two peaks of PL spectrum, a sharp emission line is detected at 1.358 eV, and the energy difference between two peaks is about 0.042 eV.

Here, variations in the PL spectrum with different excitation light intensity were investigated to examine the origin of PL spectrum. In this measurement, ND filter was utilized to decrease excitation light intensity. As the number of ND filter increases, the excitation light intensity decreases. The excitation light intensity with ND1.0 corresponds to one tenth of the

intensity with ND0. As shown in Fig. 4.13, the intensity of PL spectrum decreases with increasing the number of ND filter. Comparing each PL spectrum, the peak positions are not changed although emission peak intensity decreases. While this phenomena should be consider as band-edge emission, it is difficult to determine the origin of emission because the peak disappears by a slight decrease of excitation light intensity.

Therefore, the origin of emission was estimated by two peaks in PL spectrum. By calculating wavenumber from the energy difference of 0.042 eV, the wavenumber was estimated to 340 cm^{-1}. This wavenumber was similar with the peak of Raman spectrum in section 3.5.2 of Chapter 3. From Raman spectrum, S_2 vibration (E_{ge}) mode was observed at 343 cm^{-1}, whose mode should be double degeneracy of TO phonon and LO phonon. Therefore, the energy difference of two peaks in PL spectrum corresponds to phonon energy from electron-phonon interaction, and two peaks are considered as phonon replica derived from donor-acceptor pair (DAP) emission.

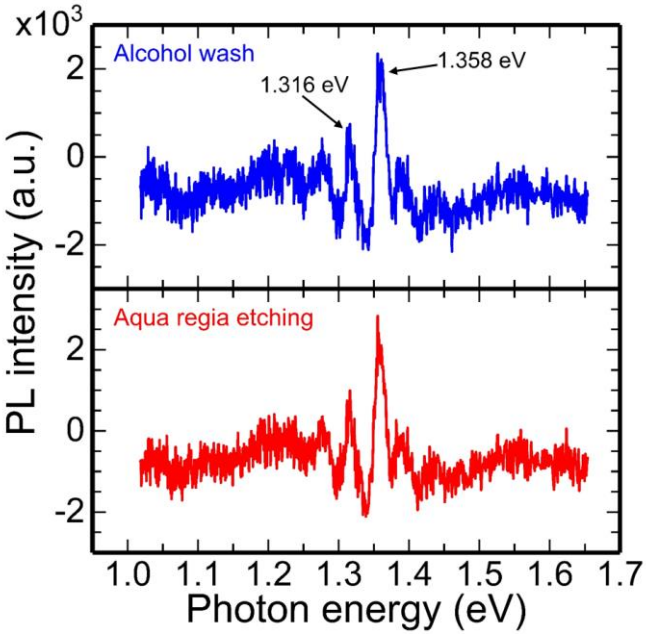

Fig. 4.12 Photoluminescence spectra of iron pyrite single crystal. Both spectra were similar in intensity and shape, and two peaks were observed at 1.316 eV and 1.358 eV.

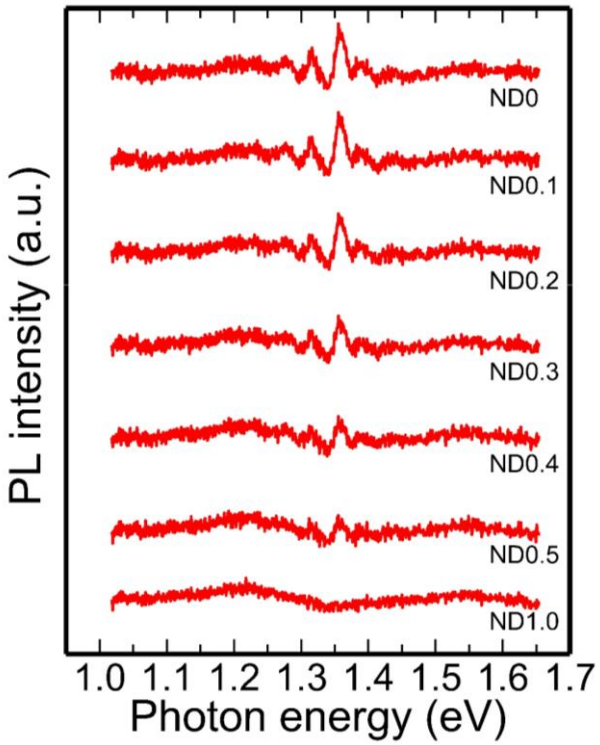

Fig. 4.13 Photoluminescence spectra of iron pyrite single crystal in different excitation laser intensity. Increasing number of ND filter, excitation laser intensity decreases. The intensity of ND1.0 corresponds to one tenth of the intensity of ND0.

4.2.6 Discussion

Energy difference between Fermi level and valence band maximum was 0.3 ~ 0.4 eV from PYS and KFM. Although iron pyrite single crystal was reported as *n*-type semiconductor as described in Chapter 1, Fermi level was located at acceptor level above valence band. This result is considered to the energy difference derived from Fe (3d) spin splitting on LFT as described in Chapter 3 [2, 3]. From Fe $2p_{3/2}$ spectra by XPS measurement, high-spin Fe^{2+} multiplets and high-spin Fe^{3+} multiplets were observed, whose high-spin Fe should encourage the formation of energy level in band gap. Therefore, Fermi level at iron pyrite surface was located at acceptor level above valence band. Energy difference between Fermi level and valence band was not much changed after aqua regia etching. In micro-PL measurement, intensity and peak position of PL spectrum of iron pyrite single crystal which was treated by both alcohol washing aqua regia etching was not different with the PL spectrum of the sample only treated by alcohol washing. In Chapter 3, removing oxidation layer at surface region was confirmed by XPS measurement. Therefore, defect level formed at iron pyrite surface was derived from oxidation layer at surface region. From LFT of Fe (3d) splitting in Fig. 4.14, reducing Fe coordination due to sulfur vacancy is suggested as forming high-spin Fe^{2+}. Therefore, some techniques such as not only removing oxidation layer but also passivation at iron pyrite surface is necessary to improve the reducing Fe coordination.

From results of ellipsometry, band gap of iron pyrite single crystal was obtained by Tauc plot. In the fitting by Tauc plot, 1.0 eV and 1.4 eV were estimated as indirect band gap and direct band gap, respectively. In addition, the result of micro-PL indicated that two peaks were observed at 1.318 eV and 1.358 eV. These peaks should be derived from phonon replica of DAP emission, which results that band gap exceeds 1.358 eV. Such indirect to direct transition in iron pyrite nanocube has already been observed by optical pump-probe studies [4]. In this research, I observed the electron transition by evaluations of optical absorption and PL for iron

pyrite single crystal. Such indirect to direct transition is not unusual in semiconductors with high density of detects and disorder, which suggests an indication of the presence of band tail below conduction band in like disordered semiconductors [5, 6]. Potential fluctuations derived from defects perturb the electronic band edges and should result in broadening of electronic states, which leads to band tails below the band edges. Therefore sub-band gap optical absorption has been observed by band tails [7].

4.3 Evaluation on Electrical Transport Characteristics of Iron Pyrite Single Crystal by Hall Effect Measurement

4.3.1 Theory

Conductivity

Resistivity on irregularly shaped samples is measured by van der Pauw method. Consider the flat sample of a conducting material of arbitrary shape, with contacts 1, 2, 3, and 4 along the periphery as shown in Fig. 4.14 to satisfy the conditions above. The resistance $R_{12,34}$ is defined by Eq. (4.6):

$$\boldsymbol{R_{12,34} = \frac{V_{34}}{I_{12}}} \qquad (\mathbf{4.6})$$

The current I_{12} enters the sample through contact 1 and leaves thorough contact 2 and V_{34} is the voltage difference between the contacts 3 and 4 ($V_{34} = V_3 - V_4$). $R_{23,41}$ is defined similarly.

The resistivity is given by Eq. (4.7):

$$\boldsymbol{\rho = \frac{\pi}{ln(2)} t \frac{(R_{12,34} + R_{23,41})}{2} F} \qquad (\mathbf{4.7})$$

F is a function only of the ratio $R_r = R_{12,34} / R_{23,41}$, satisfying the relation as shown in Eq. (4.8):

$$\frac{R_r - 1}{R_r + 1} = \frac{F}{\ln(2)} arcosh\left(\frac{exp\left[\frac{\ln(2)}{F}\right]}{2}\right) \quad (4.8)$$

For a symmetrical sample such as the circle or the square in Fig. 4.15, $R_r = 1$ and $F = 1$. This allows Eq. (7) to be simplified as shown in Eq. (4.9):

$$\rho = \frac{\pi}{\ln(2)} t R_{12,34} = 4.532 t R_{12,34} \quad (4.9)$$

Therefore the conductivity is calculated by Eq. (4.10):

$$\sigma = \frac{1}{\rho} \quad (4.10)$$

Hall coefficient

Hall effect measurement is the ability to determine the carrier density, the carrier type, and the mobility. Hall theory predicts the Hall coefficient R_H as shown in Eq. (4.11):

$$R_H = \frac{r(p - b^2 n)}{q(p + bn)^2} \quad (4.11)$$

Here, $b = \mu_n/\mu_p$ and r is the scattering factor whose value lies between 1 and 2, depending on the scattering mechanism in the semiconductor. The scattering factor is also a function of magnetic field and temperature. In the high magnetic field limit $r \rightarrow 1$. The scattering factor can be determined by measuring R_H in the high magnetic field limit, i.e., $r = R_H(B) / R_H(B = \infty)$ where B is the magnetic field. The high fields necessary for r to approach unity are not achievable in most laboratories. Typical is usually not known, it is frequently assumed to be unity. The Hall coefficient is determined experimentally by Eq. (4.12):

$$R_H = \frac{tV_H}{BI} \quad (4.12)$$

Here, t is the sample thickness, V_H the Hall voltage, B the magnetic field, and I the current. For extrinsic p-type material with $p >> n$, R_H is shown by Eq. (4.13):

$$R_H = \frac{r}{qp} \quad (4.13)$$

On the other hand, for extrinsic *n*-type material with $p >> n$, R_H is shown by Eq. (4.14):

$$\boldsymbol{R_H = -\frac{r}{qn}} \qquad (\mathbf{4.14})$$

From Hall coefficient, Hall mobility is calculated by Eq. (4.15):

$$\boldsymbol{\mu = R_H \sigma} \qquad (\mathbf{4.15})$$

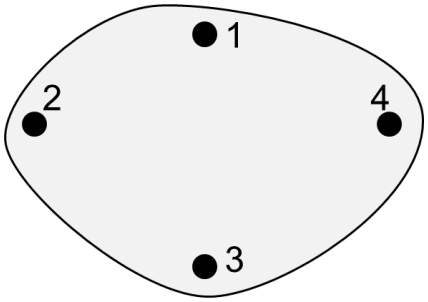

Fig. 4.14 Arbitrarily shaped sample with four contacts.

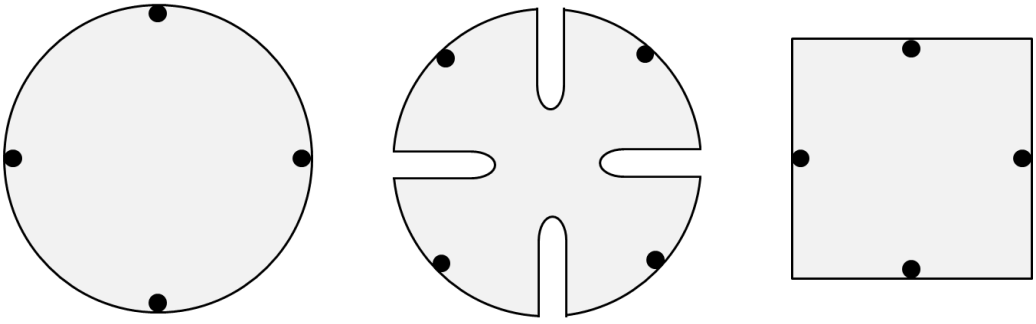

Fig. 4.15 Typical symmetrical circular and square sample geometries.

4.3.2 Experiment

Conductivity and Hall coefficient were performed from 50 to 300 K on ResiTest 8300 (Toyo Corporation) under helium atmosphere. Samples were iron pyrite single crystal wafers treated by both alcohol washing and aqua regia etching. To prepare ohmic contacts, Au thin film was deposited on samples by electron beam deposition. The thickness of Au thin film was 200 nm. To measure resistivity and Hall coefficient, the applied current was adjusted from 100 nA at 50 K to 100 μA at 300 K.

4.3.3 Result

Figure 4.18 shows results of conductivity and Hall coefficient at a temperature range of 50–300 K. In Fig. 4.18, measurement results are compared with reference data which was the result obtained by Hall effect measurement utilizing untreated iron pyrite single crystal [8]. The conductivity variation is smaller than reference data as shown in Fig. 4.16(a). Figure 4.16(b) shows the Hall coefficient variation. Hopping crossover of Hall coefficient at low temperature region is confirmed in the measurement results, whose behavior is also confirmed in reference data. In addition, Fig. 4.17 shows the carrier type from the sign of Hall coefficient. Figure 4.17 shows that *p*-type is measured at 50–85 K and *n*-type is measured at 90-300K. At low temperature region, the sign of Hall coefficient fluctuate between small positive and negative values. Thus, the Mott variable range hopping (Mott-VRH) conduction at low temperature region was examined and shown in Fig. 4.18(a) to investigate the cause that the sign of Hall coefficient fluctuated. Mott-VRH conduction was fitted by Eq. (4.16):

$$\sigma = \sigma_0 exp\left(-\frac{T_0}{T}\right)^{\frac{1}{4}} \qquad (4.16)$$

Here, σ_0 is a prefactor and T_0 is the characteristics temperature, also known as the Mott-VRH temperature. The exact temperature dependence of the prefactor σ_0 is determined by the

assumption from the electron-phonon interaction during hopping. From linear fitting of $Ln(\sigma)$ vs $1/T^{1/4}$ in Fig. 4.18(a), Mott temperature (T_0) is determined as 1.5×10^7 K. Therefore, Mott-VRH conduction is confirmed at 50–240 K. In previous reports, Mott-VRH conduction was confirmed at 40–220 K [1, 4, 9-11].

Activation energy was calculated by Eq. (4.17):

$$\boldsymbol{\sigma = \sigma_1 exp\left(\frac{E_a}{k_B T}\right)} \qquad (\mathbf{4.17})$$

In Eq. (4.17), activation energy E_a is determined by Arrhenius equation. σ_1 is a temperature independent prefactor, k_B is Boltzmann constant and T is temperature. E_a was fitted by plots of $Ln(\sigma)$ vs $1/T$ as shown in Fig. 4.18(b). In Fig. 4.18(b), each activation energy is determined to 32 meV (50–120 K), 64 meV (120–240 K) and 250 meV (240–300 K). These activation energies were much lower than the band gap obtained by evaluation of optical characteristics.

Moreover, carrier concentration and Hall mobility obtained by Hall effect measurements are shown in Fig. 4.19.

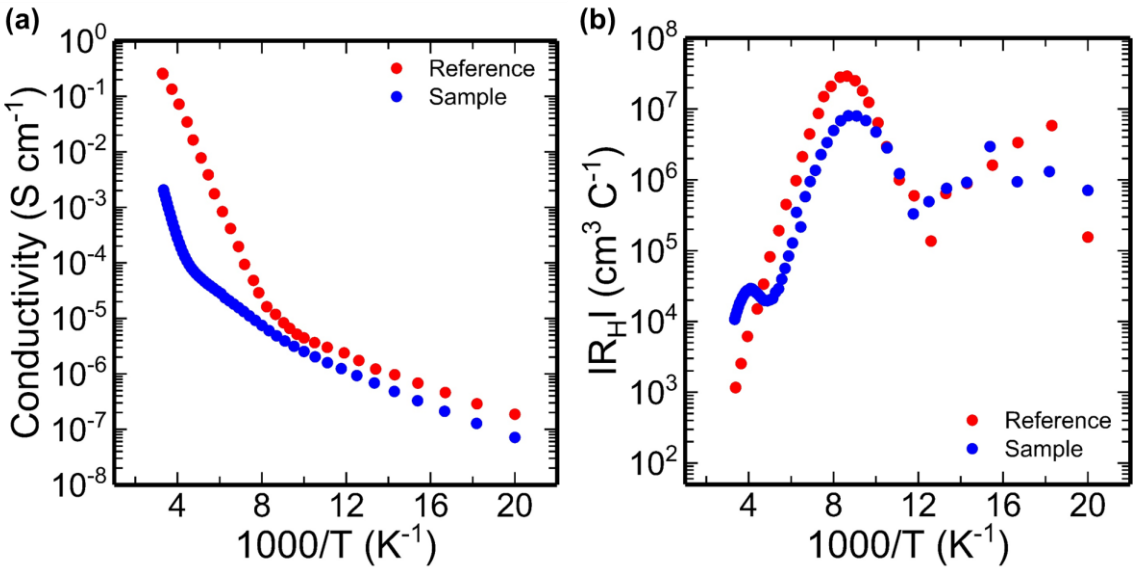

Fig. 4.16 Hall effect data of iron pyrite single crystal treated by both alcohol washing and aqua regia etching at a temperature range of 50–300 K. This result is compared with reference data. **(a)** Conductivity calculated from resistivity. **(b)** Absolute value of Hall coefficient (R_H).

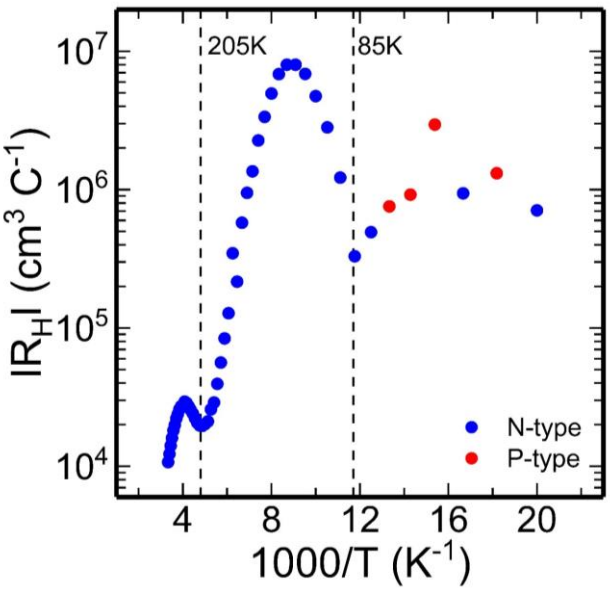

Fig. 4.17 Carrier type determination from Hall coefficient data.

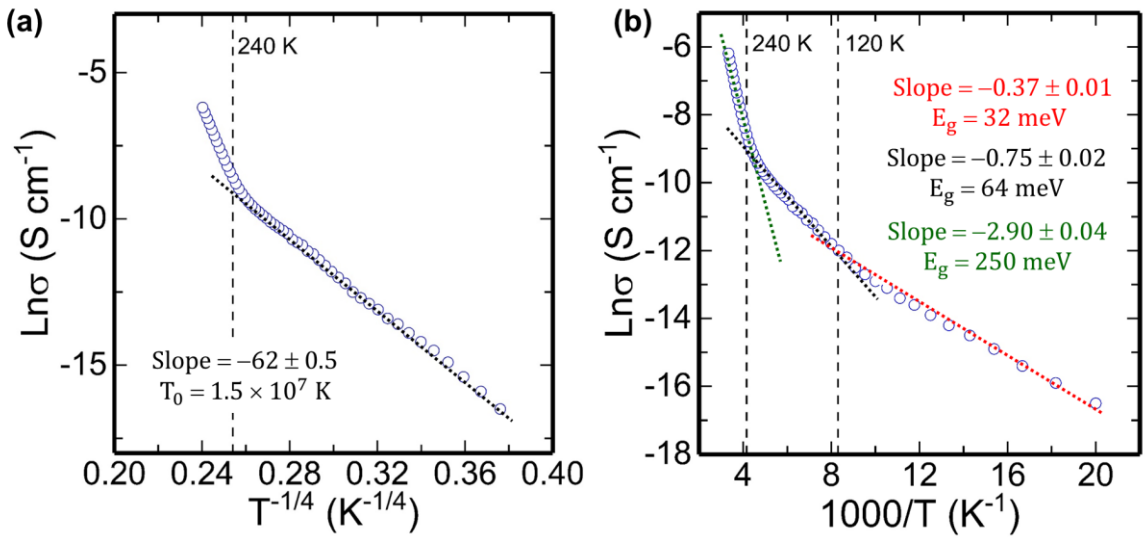

Fig. 4.18 (a) Low temperature conductivity plotted as $Ln(\sigma)$ vs $T^{-1/4}$. This plot was fitted to examine Mott-VRH conduction. From fitting the plot, T_0 is 1.5×10^7 K. **(b)** Conductivity plotted as $Ln(\sigma)$ vs T^{-1}. Activation energy (E_a) is calculated by Arrhenius equation. Each E_a is calculated as 32 meV (50–120K), 64 meV (120–240K) and 250 meV (240–300K).

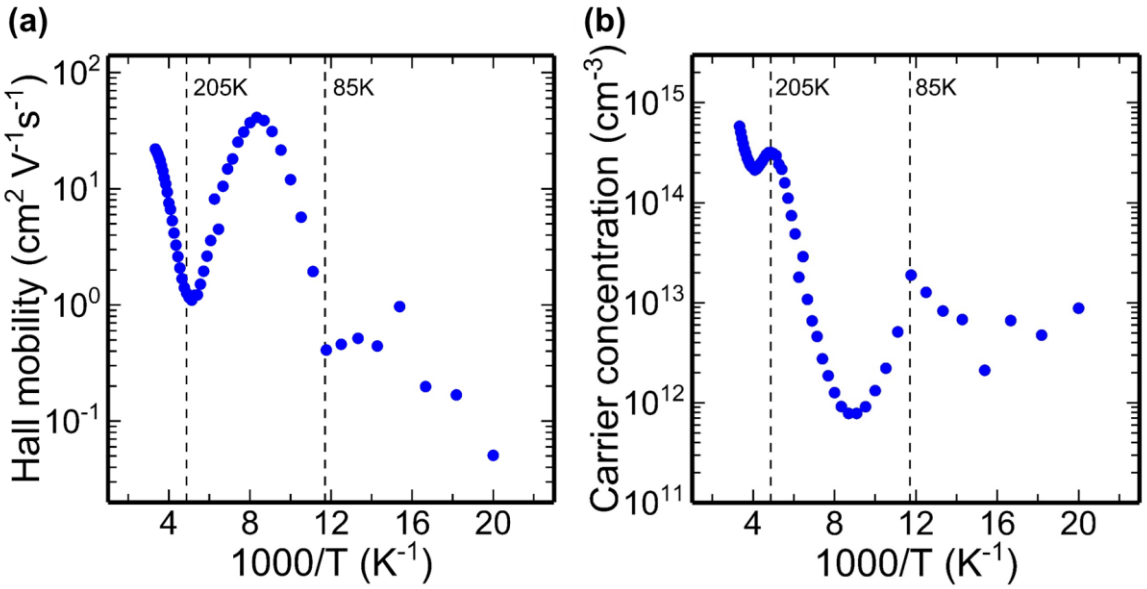

Fig. 4.19 (a) Hall mobility from Hall coefficient data. **(b)** Carrier concentration from Hall coefficient data.

4.3.4 Discussion

Temperature dependent electrical transport in iron pyrite single crystal was evaluated by Hall effect measurement to compare the samples treated by aqua regia solution with previous report which utilized untreated iron pyrite single crystal [9]. Behaviors of conductivity and Hall coefficient depending on temperature variation were similar with previous report [9]. In Fig. 4.18(a), Mott-VRH mechanism for charge transport was observed. Such conducting behavior is marked by changing transport through the localized states via phonons. The Mott-VRH type conduction phenomena in iron pyrite has been reported already [1, 5, 10-12]. Therefore, the Mott-VRH conduction was observed although iron pyrite single crystal was treated by aqua regia etching, which leaded to the result that oxidation at iron pyrite surface did not contribute to the conduction mechanism.

This hopping mechanism contributes to disorder and intrinsic defects in iron pyrite which causes localized states within the band gap and electron hops from one site to another spatially separated site. The selection of the site is based on the criteria of minimum activation energy which maximizes the hopping probability [13]. Previous study which indicated the presence of high density of defect states by optical pump probe measurement suggested that the disorder and intrinsic defects in iron pyrite caused the defect states that trapped the charge carriers and consequently assisted recombination [5]. In this measurement, hall mobility was about 0.05−40 $m^2V^{-1}s^{-1}$ at the temperature region where Mott-VRH conduction was confirmed in Fig. 4.19(b), and majority carrier type was *n*-type. Therefore, on the origin of Mott-VRH conduction, it is considered that the Fermi level is located at near localization states below conduction band minimum and hopping transport occurs in the localization states. From Fig. 4.17, the sign of Hall coefficient fluctuates between small positive and negative values at low temperature region below 85K. Based on the result of Mott-VRH conduction, the carrier type determination of Hall effect measurement should not be performed because Mott-VRH conduction is not influenced

by Lorentz force [14]. Therefore, it is difficult to determine the inversion layer at iron pyrite surface from Hall effect measurement regardless of whether the inversion layer is formed. In addition, it is also difficult to consider the value of carrier concentration and Hall mobility at low temperature below 240 K as correct value.

On the origin of the localized states below conduction band minimum, intrinsic sulfur vacancy in iron pyrite single crystal should contribute to the formation of localized states because the result of EMPA in section 3.4 of Chapter 3 indicated that sulfur in iron pyrite single crystal was less than ideal stoichiometric ratio of Fe : S = 1 : 2. As an example of the formation of localized states in band gap by vacancy, $ZnIn_2Te_4$ was reported [15]. The crystal structure of $ZnIn_2Te_4$ was defect chalcopyrite structure and vacancy was formed in crystal, which leaded to the formation of band tail below conduction band and broadened Gaussian level above valence band [15]. In iron pyrite at low temperature, the crystals tend to reduce their total energy due to sulfur vacancy diffusion into some low energy configurations where exchange coupling of the unpaired electrons could occur via the Fe ions [16]. Therefore, it is necessary to improve localized states of iron pyrite to eliminate the effect of Mott-VRH to Hall effect measurement and determine suitably the change of carrier type depending on temperature.

4.4 Description of band diagram of iron pyrite single crystal

From evaluation of band structure and electrical transport characteristics, band structures are described in Fig. 4.20. As shown in Fig. 4.20(a), Fermi level in bulk region is located near indirect conduction band edge and Mott-VRH conduction occurs thorough the localized states below direct conduction band edge. On the other hand, Fermi level at surface region is located in acceptor level as shown in Fig. 4.20(b) from the results of KFM and PYS. The difference of Fermi level between the bulk region and the surface region should form upward band bending and lead to the inversion layer.

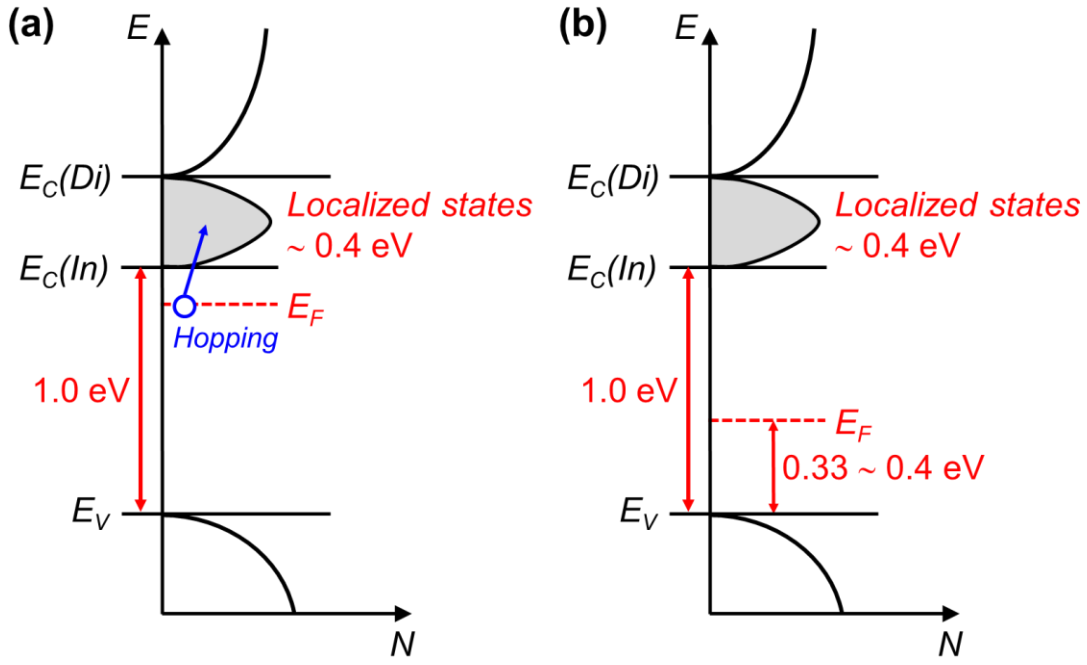

Fig. 4.20 (a) Band diagram in bulk region of iron pyrite single crystal, **(b)** at surface region.
$E_C(Di)$: Direct conduction band edge, $E_C(In)$: Indirect conduction band edge,
E_F : Fermi level, E_V : Valence band edge

4.5 Summary

Band structure was evaluated by various methods such as PYS, KFM, ellipsometry, Micro-PL and Hall effect. Comparing iron pyrite single crystal treated by aqua regia solution with alcohol-washed sample, optical and electrical characteristics were not change. Therefore, oxidation at iron pyrite surface could not contribute to the conduction mechanism and electrical transitions. On the other hand, indirect to direct transition in iron pyrite single crystal was observed by evaluation of optical characteristics. In addition, Mott VRH conduction also was observed by Hall effect measurement at low temperature, which should contribute to electrical transition in localized states. Based on these results, band diagram was described.

Reference

[1] M. Caban-Acevedo, N. S. Kaiser, C. R. English, D. Liang, B. J. Thompson, H. E. Chen, K. J. Czech, J. C. Wright, R. J. Hamers, S. Jin, J. Am. Chem. Soc. 136 (2014) 17163-17179.

[2] J. Hu, Y. Zhang, M. Law, R. Wu, Phys. Rev. B 85 (2012).

[3] M. Bronold, Y. Tomm, W. Jaegermann, Sur. Sci. Lett. 314 (1994) L931-L936.

[4] H. W. Nesbitt, G. M. Bancroft, A. R. Pratt, M. J. Scaini, Am. Mineral. 83 (1998) 1067–1076.

[5] S. Shukla, G. Xing, H. Ge, R. R. Prabhakar, S. Mathew, Z. Su, V. Nalla, T. Venkatesan, N. Mathews, T. Sritharan, T. C. Sum, Q. Xiong, ACS Nano 10 (2016) 4431-4440.

[6] P. Lazic, R. Armiento, F. W. Herbert, R. Chakraborty, R. Sun, M.K. Chan, K. Hartman, T. Buonassisi, B. Yildiz, G. Ceder, J. Phys.: Condens. Matter 25 (2013) 465801.

[7] J. M. Lucas, C.-C. Tuan, S. D. Lounis, D. K. Britt, R. Qiao, W. Yang, A. Lanzara, A. P. Alivisatos, Chem. Mater. 25 (2013) 1615-1620.

[8] J. Bernasconi, Phys. Rev. B 7 (1973) 2252-2260.

[9] M. Limpinsel, N. Farhi, N. Berry, J. Lindemuth, C.L. Perkins, Q. Lin, M. Law, Energy Environ. Sci. 7 (2014) 1974-1989.

[10] K. Ellmer, D. Lichtenberger, A. Ennaoui, C. Hopfner, S. Fiechter, H. Tributsch, Conference Record of the Twenty Third IEEE (1993) 535-538.

[11] D. Lichtenberger, K. Ellmer, R. Schieck, S. Fiechter, H. Tributsch, Thin Solid Films 246 (1994) 6-12.

[12] M. Caban-Acevedo, D. Liang, K. S. Chew, J. P. DeGrave, N. S. Kaiser, S. Jin, ACS Nano 7 (2013) 1731-1739.

[13] P. A. Lee, T. V. Ramakrishnan, Rev. Mod. Phys. 57 (1985) 287-337.

[14] H. T. Yi, Y. N. Gartstein, V. Podzorov, Sci. Rep. 6 (2016) 23650.

[15] S. Ozaki, S.-I. Boku, S. Adachi, Phys. Rev. B 68 (2003).

[16] Y. N. Zhang, M. Law, R. Q. Wu, J. Phys. Chem. C 119 (2015) 24859-24864.

Chapter 5

Conclusions

5.1 Conclusions

Iron pyrite has a good potential as low cost and earth-abundant photovoltaic device material. However, iron pyrite thin film photovoltaic devices have not obtained conversion efficiency yet. In this thesis, an inversion layer at iron pyrite surface was focused as the cause of poor photovoltaic performance, and device simulation and characteristic evaluation were performed toward realizing high performance iron pyrite photovoltaic device. The main conclusions obtained in the present study are summarized as follows.

In Chapter 2, two-dimensional (2D) device simulation was performed to investigate the cause of poor performance of iron pyrite thin film photovoltaic devices which have been fabricated in the past, and to understand the effects of the density of states at the deep donor level and the inversion layer on the iron pyrite photovoltaic devices. It was founded that the following factors allowed FeS_2 photovoltaic device efficiency as high as around 13.5% to be achieved: a *p*-Cu_2O/*n*-FeS_2 hetero-junction, a density of states in the bulk layer of less than 1×10^{15} cm^{-3}, and carrier lifetime in the bulk of longer than 1 μs. To realize higher efficiency FeS_2 photovoltaic device, it is necessary to remove the surface layer and reduce the density of states of the deep donor level during the fabrication of the FeS_2 bulk layer.

In Chapter 3, the chemical-bonding state and phase purity at the surface region of iron pyrite single crystal was evaluated by micro-Raman spectroscopy and XPS. To compare the surface condition of iron pyrite single crystal, the samples only treated by alcohol washing and the samples treated by both alcohol washing and aqua regia etching were measured, respectively.

Micro-Raman spectroscopy indicated that phase purity at the surface region of iron pyrite was improved by aqua regia etching, which suggested that aqua regia solution could remove contamination and adjust the stress at surface region. From the results of XPS, it was found that Fe^{2+} multiplets and Fe^{3+} multiplets were observed from the $Fe2p_{3/2}$ spectra in both treatment conditions of alcohol washing and aqua regia etching. These multiples corresponds to high-spin Fe^{2+} and Fe^{3+}, which should result in forming defect level in band gap by spin splitting based on LFT. Oxidation productions at the surface region of iron pyrite were removed by aqua regia etching because the intensity of O 1s spectrum decreased. However, O 1s spectrum was confirmed after aqua regia etching. This result suggests the oxide and water in air immediately reacts the surface of iron pyrite and Fe^{3+}–OH^- species are created. Therefore, it is difficult to completely prevent the oxidation reaction on the surface region.

In Chapter 4, band structure and electrical transport characteristics of iron pyrite single crystal were evaluated. PYS, KFM and ellipsometry to evaluate band structure of iron pyrite. The results of PYS and KFM indicated that the energy difference between Fermi level and valence band was around 0.35 eV. Furthermore, Tauc plot of indirect type estimated the band gap of iron pyrite to be 1.0 eV. Therefore, Fermi level is located at acceptor level although the carrier type of iron pyrite single crystal is *n*-type, which suggests that the surface region of iron pyrite single crystal should form an inversion layer. Since these results were not changed after aqua regia etching, the formation of the inversion layer at iron pyrite surface should contribute to defect levels based on LFT model rather than oxidation layer. In addition, direct transition was observed by Tauc plot although iron pyrite was reported as indirect transition from band calculation. To evaluate electron transition of iron pyrite single crystal with different optical measurement from ellipsometry, Micro-PL was performed. PL spectrum shown two peaks in 1.316 eV and 1.358 eV, which indicated that electron transition over 1.0 eV occurred in band gap. Therefore, it is presumed that localized states below conduction band is formed from

optical measurement. From Hall effect measurement, Mott-VRH conduction at low temperature below 240K observed. Mott-VRH conduction is phenomena that carriers constrained to localized states move between localized levels by thermal excitation. Therefore, Mott-VRH conduction should occur in localized states below conduction band. In addition, the sign of Hall coefficient fluctuates between small positive and negative values at low temperature region below 85K, which suggests that the carrier type determination of Hall effect measurement should not be performed because Mott-VRH conduction is not influenced by Lorentz force.

As described above, some problems to be improved in iron pyrite were found toward high performance iron pyrite thin film photovoltaic device. Especially, it was revealed that not only the inversion layer but also the intrinsic defect levels in the bulk contributed to poor performance of photovoltaic device. To improve photovoltaic characteristics, it is necessary to reduce the intrinsic defect levels in the bulk because the intrinsic defect levels lead to the formation of localized states below conduction band which reduces band gap and encourage the carrier recombination through the defects. In addition, developing the stabilization method of Fe coordination at the surface region is necessary while preventing the reaction of oxygen with the surface.

5.2 Future work

Through this work, some problems were revealed toward high performance iron pyrite thin film photovoltaic device. To improve these problems, it will be essential to develop suitable methods as follow,

Development of surface passivation for improvement of Fe coordination:

Since it is found that the surface of iron pyrite immediately absorbed oxygen in the air, surface treatment in atmosphere without oxygen is essential to prevent the absorption of oxygen at the surface of iron pyrite. In addition, surface passivation utilizing sulfur rich compound is

necessary to improve the decreasing Fe coordination after removing oxidation layer.

Development of doping in iron pyrite to form suitable photovoltaic material:

As already mentioned, band bending, potential fluctuations and Mott-VRH conduction might be derived from defects in iron pyrite. Especially, it seems that intrinsic sulfur vacancies are the most reasonable and suitable explanation for the origin of the bulk and surface states in iron pyrite. To improve intrinsic sulfur vacancies, the development of making bulk crystal and thin film while perfectly controlling the sulfur stoichiometry in iron pyrite. However, the challenge is difficult to achieve due to thermal instability of iron pyrite [1, 2]. As an alternative strategy, the development of doping method in iron pyrite is desirable. Recently, Fe_2GeS_4 and Fe_2SiS_4 were reported as alternative photovoltaic material of iron pyrite [2]. These materials have been reported to present a six-coordinate environment for Fe^{2+} and replace the disulfide S_2^{2-} with simple sulfide S^{2-}. In addition, it was reported that the ternary compounds didn't readily decompose into S-deficient binary phases. Therefore, these materials have good potential as next generation photovoltaic material.

Reference

[1] M. Birkholz, S. Fiechter, A. Hartmann, H. Tributsch, Phys. Rev. B 43 (1991) 11926-11936.

[2] L. Yu, S. Lany, R. Kykyneshi, V. Jieratum, R. Ravichandran, B. Pelatt, E. Altschul, H. A. S. Platt, J. F. Wager, D. A. Keszler, A. Zunger, Adv. Energ. Mater. 1 (2011) 748-753.

List of Publications

A. Academic Journals

1. Shunsuke Uchiyama, Yasuaki Ishikawa, and Yukiharu Uraoka
   "Effect of inversion layer at iron pyrite surface on photovoltaic device"
   Jpn. J. Appl. Phys. 57 (2018) 032301.

B. International Conference

1. Shunsuke Uchiyama, Yasuaki Ishikawa, Takahiro Doe, and Yukiharu Uraoka
   "Evaluation of Band Structure of FeS_2 Thin Films for Next Generation Solar Cell Materials", 2014 GIST-NAIST-NCTU Joint Symposium on Advanced materials, GIST, Korea, November (2014)
2. Shunsuke Uchiyama, Yasuaki Ishikawa, Takahiro Doe, and Yukiharu Uraoka
   "Evaluation of band structure and conductivity property of iron pyrite (FeS_2) thin films deposited by spin-coating", The 2015 International Meeting for Future of Electron Devices, Ryukoku University Avanti Kyoto Hall, Japan, June (2015)
3. Shunsuke Uchiyama, Yasuaki Ishikawa, Yusuke Kawamura, and Yukiharu Uraoka
   "Numerical Modeling of Device Structure for FeS_2 Thin Film Solar Cells", Active-Matrix Flatpanel Displays and Devices-16, Ryukoku University Avanti Kyoto Hall, Japan, June (2016)
4. Shunsuke Uchiyama, Yasuaki Ishikawa, and Yukiharu Uraoka
   "Device Modeling of Iron Pyrite Solar Cell for High Conversion Efficiency", 27^{th} International Photovoltaic Science and Engineering Conference, Lake Biwa Otsu Prince Hotel, Japan, November (2017)

5. Shunsuke Uchiyama, Yasuaki Ishikawa, Yoshitaro Nose, and Yukiharu Uraoka
"Surface Analysis of FeS_2 Pyrite Bulk Crystal", 2017 GIST-NAIST-NCTU Joint Symposium on Advanced materials, GIST, Korea, October (2017)

C. Domestic Conference

1. Shunsuke Uchiyama, Yasuaki Ishikawa, Takahiro Doe, and Yukiharu Uraoka
"Evaluation on Band Structure of FeS_2 Thin Film as a Candidate of Next-Generation Photovoltaic Device Material", Thin Film Materials and Devices Meeting 2014, Ryukoku University Avanti Kyoto Hall, Japan, October (2014)
2. Shunsuke Uchiyama, Yasuaki Ishikawa, Takahiro Doe, and Yukiharu Uraoka
"Evaluation on Band Structure and Conductivity of FeS_2 Thin Film as a Candidate of Next-Generation Photovoltaic Device Material", 2015 Japan Society of Applied Physics, Kansai Chapter 3rd Meeting, NAIST, Japan, February (2015)
3. Shunsuke Uchiyama, Yasuaki Ishikawa, and Yukiharu Uraoka
"Search of Device Structure by Simulation to Establish the Device Model of FeS_2 Thin Film Solar Cell", 2016 Japan Society of Applied Physics, Kansai Chapter 3rd Meeting, Osaka Prefecture Univ., Japan, February (2016)
4. Shunsuke Uchiyama, Yasuaki Ishikawa, and Yukiharu Uraoka
"Search of Device Structure by Simulation to Realize the FeS_2 Thin Film Solar Cell", 13th Symposium of Next Generation Solar Power System, Nagaoka City Hall Plaza Ao-re Nagaoka, Japan, May (2016)
5. Shunsuke Uchiyama, Yasuaki Ishikawa, and Yukiharu Uraoka
"Investigation of Device Structure of FeS_2 Solar Cell by Device Simulation", 14th Symposium of Next Generation Solar Power System, Nagoya Univ., Japan, July (2017)

D. Related Presentations

1. Takahiro Doe, Yasuaki Ishikawa, Shunsuke Uchiyama, Masahiro Horita, and Yukiharu Uraoka

   “Precursor Dependence of FeS_2 Thin Film Formed by Electro-Spray Deposition”, 75th JSAP Fall Meeting, Hokkaido Univ., Japan, September (2014)

2. Takahiro Doe, Yasuaki Ishikawa, Shunsuke Uchiyama, Masahiro Horita, and Yukiharu Uraoka

   “Precursor Dependence of Formation of FeS_2 Films via Electro-Spraying and Sulfuration Annealing”, The 2014 MRS Fall Meeting, Hynes Convention Center, USA, December (2014)

3. Yusuke Kawamura, Yasuaki Ishikawa, Shunsuke Uchiyama, Yoshitaro Nose, and Yukiharu Uraoka

   “Evaluation of Band Offset of FeS_2/NiO_x Junctions toward Hetero Junction FeS_2-Pyrite Solar Cell”, 2016 SDM, NAIST, Japan, December (2016)